Midbrain Kappa Opioid Receptor-Expressing Neurons Modulate Multiple Dimensions of Opioid Withdrawal

by

Ruby A. Holland

B.A., University of Pennsylvania, 2016

Submitted to the Graduate Faculty of the

Click to choose your school in partial fulfillment

of the requirements for the degree of

Doctor of Philosophy

University of Pittsburgh

2023

UNIVERSITY OF PITTSBURGH

SCHOOL OF MEDICINE

This dissertation was presented

by

Ruby Andrea Holland

It was defended on

July 6, 2023

and approved by

Dr. H. Richard Koerber, PhD, Professor, Department of Neurobiology

Dr. Michael S. Gold, PhD, Professor, Department of Neurobiology

Dr. Mary M. Torregrossa, PhD Associate Professor, Department of Psychiatry

Dr. Anthony A. Grace, PhD, Distinguished Professor, Department of Neuroscience

Dr. Meaghan C. Creed, PhD, Associate Professor, Washington University in St. Louis

Thesis Advisor/Dissertation Director: Dr. Sarah E. Ross, PhD, Associate Professor, Department of Neurobiology

Midbrain Kappa Opioid Receptor-Expressing Neurons Modulate Multiple Dimensions of Opioid Withdrawal

Ruby Andrea Holland, PhD

University of Pittsburgh, 2023

Opioid withdrawal is a multidimensional, whole-body response to the abrupt cessation of chronic opioids. Treatment options are limited, and the distressing, debilitating symptoms of opioid withdrawal represent a significant barrier to recovery from opioid use disorder. It is believed that opioids promote withdrawal through the adaptation of aversive signals to counteract hyperactive reward systems. However, much remains unclear about the neural circuits influenced by opioids due to the varying actions of opioids on the broadly expressed delta, mu, and kappa opioid receptors. Recently, the kappa opioid receptor (KOR) and its endogenous ligand dynorphin have gained special attention for their roles in aversive states such as stress and chronic pain, particularly through acting on neurons emanating from the ventral tegmental area (VTA). However, less is known about the anatomy of VTA neurons which express KOR (VTA^{KOR} neurons) or the projection-specific contributions of VTA^{KOR} neurons to the aversive, negative affective, and autonomic effects of opioid withdrawal. To address these gaps in knowledge, we utilized a combination of genetic, physiological, and behavioral approaches to selectively target VTA^{KOR} neurons *in vivo*. Through a combination of cre-dependent viral tracing, immunohistochemistry, and RNAscope FISH, we found that VTA^{KOR} neurons express multiple neurotransmitters and project to distinct regions throughout the forebrain, midbrain, and hindbrain. Chronic opioids increase dynorphin expression in VTA input regions, decrease morphine-induced neuronal activation in the VTA, and alter the firing properties of VTA^{KOR} neurons and their inputs.

Consistent with this, chemogenetic activation of VTA^{KOR} neurons attenuated withdrawal-associated behaviors such as jumping, shakes and tremors, body weight loss, diarrhea, and urination, indicating VTA^{KOR} neural inhibition is necessary in opioid withdrawal symptoms. Chemogenetic activation of VTA^{KOR} neurons also abolished withdrawal-induced conditioned place aversion and attenuated withdrawal-associated anxiety-like and depressive-like behaviors. When we selectively activated VTA^{KOR} neurons projecting to the ventrolateral periaqueductal gray ($VTA \rightarrow vlPAG^{KOR}$ neurons), withdrawal-associated body weight loss, diarrhea, and urination were selectively attenuated. Taken together, these results demonstrate that chronic opioids inhibit the activity of VTA^{KOR} neurons, and that this inhibition is necessary for the precipitation of withdrawal. Furthermore, these results highlight the critical role of central midbrain mechanisms by which opioids modulate the gastrointestinal system.

Table of Contents

List of Tables

List of Figures

Acknowledgments

I would like to thank all the people who were instrumental in my growth as a scientist and as a person. My passion for neuroscience began as a freshman in college at the University of Pennsylvania in the laboratory of Dr. Bart De Jonghe. As my first research mentor, Bart encouraged me to take on independent projects, contribute to manuscripts early on in my training, and communicate my work at conferences. He was also the first person to suggest I pursue an MD/PhD. I would like to thank Bart for his support, training, and mentorship, and for supporting me in my personal growth and pursuit of a dual degree. I would also like to thank Dr. Amber Alhadeff, my first collaborator. In addition to her training, mentorship, and collaboration, Amber served as a powerful example to me of what a thriving neuroscientist looks like, and I continue to aspire to her scientific rigor and career success.

I would like to express my immense gratitude to my thesis advisor and mentor, Dr. Sarah E. Ross. It was during my time in Sarah's lab that I grew into an independent researcher, ready to take on new challenges and mentees of my own. Sarah's support and kindness have helped me grow as both a scientist and person. It has been a privilege to work with her, and I will carry her wisdom and lessons with me throughout my professional career. In addition, I would like to thank all the members of the Ross Lab for their feedback, friendship, and assistance over the years in lab. In particular, I'd like to thank Dr. Kelly Smith and Dr. Eileen Nguyen for their peer mentorship and collaborative work on this project, as well as BaDoi Phan, Isabel Bleimeister, and Jeffrey Okoro for their analytical assistance. Much of the work in this dissertation was completed with the help of dedicated undergraduates; I would like to thank Samantha Sherman, Ava Zoltanski, and Tommy Nguyen for their assistance.

I would like to thank my dissertation committee members, Drs. H. Richard Koerber, Michael Gold, Mary Torregrossa, and Anthony Grace for their advice and feedback as well as Dr. Meaghan Creed for her time and effort by serving as my outside examiner. I would also like to thank the leadership of the University of Pittsburgh and Carnegie Mellon University Medical Scientist Training Program, Dr. Richard Steinman and Kathleen Hansell-Prigg for their support. I would also like to thank Drs. Rahilla Tarfa and Rebekah Evans for providing their time and expertise towards patch clamp electrophysiology in the ventral tegmental area, as well as Dr. Ross Williamson and Megan Arnold for training and use of their Leica DM6B epifluroescent microscope.

My training in the Center for Neuroscience at the University of Pittsburgh (CNUP) would not have been possible without the hard work of administrators. In particular, I would like to thank Patti Argenzio, Sarah Bakaitus, Hunter Simpson, Natalee Bright, Shawn Steele, and Heather Scott for their assistance throughout my time as a student at the CNUP and for always being a supportive presence throughout my training. I would also like the thank the DLAR veterinary and husbandry staff for caring and advocating for the animals used in the experiments described here.

The work in this dissertation would not have been possible without the support of my closest family and friends. In particular, I would like to thank my mother, Lisa Nelson, for all that she has done and sacrificed so that I could have access to the many educational opportunities which have empowered me to pursue my academic endeavors. I would also like to thank my younger sister, Selah Gamble, for her continual support throughout my years in school. I would also like to thank my grandmother for her support and assistance throughout my life. I would like to thank all of my friends, particularly Hannah Elarmo, Kristen Leong, BaDoi Phan, Alex Schuyler, Hannah Apfelbaum, Talia Adi, Jeremy Gedeon, Ariel Epouhe, Elizabeth Meador, Sarah Svirsky, Kelly

Smith, and Abby Hellmann. I would like to thank my feline roommate Calvin for his companionship, chaotic good nature, and for enhancing my black outfits with his fur. I would like to thank the members of my knit-crochet group and community garden for keeping me grounded and fostering my creativity. Finally, I would like to thank the rest of my family for their lifelong support of me and my goals.

Abbreviations

aca – anterior commissure, anterior part

acp – anterior commissure, posterior

aCSF – artificial cerebrospinal fluid

AP – action potential

ANOVA – analysis of variance

aq – aqueduct

Arc – arcuate nucleus of the hypothalamus

BNST – bed nucleus of the stria terminalis

cc – central canal

CeA – central nucleus of the amygdala

CLi – caudal linear nucleus of the raphe

CM – central medial thalamic nucleus

CPA – conditioned place aversion

CPu – caudate putamen

CPP – conditioned place preference

D3V – dorsal third ventricle

DAMGO – [D-Ala^2, *N*-MePhe^4, Gly-ol]-enkephalin

DOR – delta opioid receptor

DRD – dorsal raphe nucleus dorsal part

DRI – dorsal raphe nucleus interstitial part

DR – dorsal raphe nucleus

DSM-5 – Diagnostic and Statistical Manual of Mental Disorders, Fifth Edition

EPSC – excitatory postsynaptic current

GABA – gamma aminobutyric acid

GAD67 – glutamic acid decarboxylase 67

Gi – giganticellular reticular nucleus

GiA – giganticellular reticular nucleus alpha part

ic – internal capsule

IF – interfascicular nucleus

IL – infralimbic cortex

IO – inferior olive

IOB – inferior olive subnucleus B of medial nucleus

IOC – inferior olive subnucleus C of medial nucleus

IOD – inferior olive dorsal nucleus

IOPr – inferior olive principal nucleus

IP – intraperitoneal

IPn – interpeduncular nucleus

IPSC – inhibitory postsynaptic current

IRt – intermediate reticular nucleus

KOR – kappa opioid receptor

LHb – lateral habenula

LH/LHA – lateral hypothalamic area

LPGi – lateral paragigantocellular nucleus

lPBN – lateral parabrachial nucleus

MD – medial dorsal thalamic nucleus

MdD – medullary reticular nucleus dorsal part

mlf – medial longitudinal fasciculus

MOR – mu opioid receptor

mPFC – medial prefrontal cortex

MRn – medullary reticular nucleus

NAc – nucleus accumbens

NAcC – nucleus accumbens core

NAcSh – nucleus accumbens shell

NB – neurobiotin

NTS – nucleus tractus solitarius

Oprk1 – opioid receptor kappa 1 gene

Oprm1 – opioid receptor kappa 1 gene

OUD – opioid use disorder

PBP – parabrachial pigmented nucleus

Pdyn – prodynorphin gene

PN – paranigral nucleus

PnO – pontine reticular nucleus, oral part

PrL – prelimbic cortex

PVH – periventricular nucleus of the hypothalamus

py – pyramidal tract

RLi – rostral linear nucleus of the raphe

RM – repeated measures

RMg – raphe magnus nucleus

RMTg – rostromedial tegmental nucleus

ROb – raphe obscurus nucleus

Rt – reticular thalamic nucleus

RVM – rostral ventromedial medulla

scp – superior cerebellar peduncle (brachium conjunctivum)

Slc17a6 – solute carrier family 17, member 6 gene

Slc32a1 – solute carrier family 32, member 1gene

SUD – substance use disorder

SV-VII, SX – sacral laminae V-VII, sacral lamina X

tdT – tdTomato

TH – tyrosine hydroxylase

ts – tectospinal tract

vlPAG – ventrolateral periaqueductal gray

VP – ventral pallidum

VTA – Ventral tegmental area

ZI – zona incerta

1.0 Chapter 1: Introduction

1.1 The Epidemiology and Burden of Opioid Addiction

Throughout history, opioids have served as our most effective pharmacological agents for the treatment of severe pain. Unfortunately, the hedonic effects of opioids encourage impulsive use, dependence, and addiction. Addiction is a term which can be defined through two lenses. To clinicians, opioid addiction refers to a medical condition, also termed opioid use disorder (OUD), which occurs when people engage in a problematic pattern of opioid use leading to clinical impairment or distress (American Psychiatric Association, 2013). To scientists, the term addiction describes a poorly understood biological process which involves complex interactions between genetics, brain circuits, and an individual's environment and experiences. While the experiments described in this dissertation serve to dissect the neurobiological mechanisms underlying opioid addiction, it is important to highlight the urgent public health context motivating this work.

Currently, more than 2.7 million people aged 12 and older in the United States meet criteria for OUD as defined by the Diagnostic and Statistical Manual of Mental Disorders (DSM-5), which amounts to approximately 1% of the population (Substance Abuse and Mental Health Services Administration & U.S. Department of Health and Human Services, 2021). OUD can lead to several adverse health outcomes. Intravenous opioid use can lead to systemic bloodborne infections such as endocarditis, hepatitis B, and HIV. Additionally, chronic opioids can lead to a paradoxical increase in pain sensitivity known as opioid-induced hyperalgesia, which can complicate pain management. Opioids also induce constipation which can progress to opioid-induced bowel dysfunction. Most alarmingly, opioids induce respiratory depression which can

lead to overdose. Opioid overdose deaths have increased ten-fold in the past two decades, and spiked to more than 80,000 deaths annually in 2021 in the context of the COVID-19 pandemic. Most deaths have involved fentanyl (Spencer et al., 2022).

Additionally, longstanding criminal policies and stigma surrounding drug use have exerted grave social and financial consequences on those suffering from OUD and other substance use disorders (SUDs). The mass incarceration of disproportionately Black drug users has led to mass felony disenfranchisement and the creation of a permanent underclass of citizens with limited access to public resources and opportunities (Csete et al., 2016). While modern policies have invested more public funds towards health-centered approaches and treatment interventions (Office of National Drug Control Policy, 2016), there still exist major legal barriers for those with SUDs to acquiring employment, pursuing postsecondary education, obtaining business licenses, receiving food stamps, and maintaining custody of children (National Inventory of Collateral Consequences of Conviction, 2023). Furthermore, the Controlled Substances Act of 1970 classifies psychedelics and marijuana as Schedule I substances, effectively halting research on these substances despite growing research supporting their benefits for the treatment of SUDs (Dos Santos et al., 2018). In the wake of our most recent opioid overdose crisis, it is imperative that policies continue to shift towards the investment of scientific effort and resources into understanding the neurobiological mechanisms underlying opioid addiction and identifying novel therapeutic approaches to combatting the adverse health outcomes associated with opioid use.

1.2 Opioid Withdrawal

Notable psychiatrist M. A. H. Russell, a leader in tobacco dependence research, was one of the first to assert that dependence on drugs required negative affect experienced in its absence (Russell, 1976). Opioid withdrawal is the negative affective state which results from the rapid cessation of chronic opioids (Farrell, 1994). Withdrawal can occur spontaneously through abstinence from opioids or can be precipitated through the administration of an opioid antagonist such as naloxone. Importantly, withdrawal can also occur through the cessation of OUD maintenance therapies such as buprenorphine or methadone (Gossop & Strang, 1991). Opioid withdrawal impacts regulatory and homeostatic systems throughout the body. Withdrawal dysregulates mood and affect resulting in anxiety, restlessness, agitation, depression, and insomnia. Additionally, sympathetic arousal manifests as rigors, diaphoresis, mydriasis, hypertension, and tachycardia. Withdrawal also commonly presents with debilitating gastrointestinal symptoms such as nausea, vomiting, and intractable diarrhea (Kanof et al., 1993).

While opioid withdrawal is not classically described as life threatening, several complications of opioid withdrawal and long-term abstinence make discontinuation of chronic opioids highly dangerous (James et al., 2019). Firstly, sympathetic overactivity and electrolyte imbalances in the context of acute opioid withdrawal can result in cardiovascular complications such as stress cardiomyopathy and atrial fibrillation (Krantz et al., 2021; Spadotto et al., 2013; Wedam & Haigney, 2016). Furthermore, opioid withdrawal is incredibly emotionally distressing and commonly precipitates major depressive episodes, which substantially increase the risk of suicide (Demidenko et al., 2017; Fenton et al., 2022). Finally, sudden abstinence from opioids increases the risk of relapse and overdose. During a period of withdrawal, an individual loses a degree of physiological tolerance to opioids. When one relapses by taking their typical pre-

withdrawal dose of opioids, there is a substantial risk of accidental overdose (Oliva et al., 2020). Therefore, identifying the neural mechanisms underlying opioid withdrawal specifically is of paramount importance in combatting the opioid use and overdose crisis.

1.3 Positive and Negative Reinforcement

Animals must learn to prioritize and respond to a variety of internal (e.g. pain, fear, hunger) and external (e.g. food, predators, mates) stimuli in diverse contexts order to survive. Reward and aversion are both necessary in this form of learning, wherein behaviors which are beneficial to survival are encouraged, while behaviors which are maladaptive or hazardous are discouraged. Motivated behaviors can be either positively reinforced (i.e. through the administration of a rewarding stimulus) or negatively reinforced (i.e. through the removal of an aversive stimulus) (Skinner, 1938).

Opioids are one of many classes of psychoactive drugs which motivate drug-seeking behaviors through both positive and negative reinforcement. In short-term or casual opioid use, the pursuit of opioids is driven by positive reinforcement, as they produce feelings of euphoria (i.e. reward). Consistent with this, rats can be easily trained to press a lever in order to receive an infusion of morphine, and morphine induces a conditioned place preference in rodents (Bozarth & Wise, 1984; Shippenberg & Herz, 1987; Young et al., 1979). However, as opioid use becomes chronic and an individual becomes dependent, drug-seeking behaviors are equally – if not more heavily – driven by negative reinforcement, such as through the relief of pain and suffering, and the prevention of withdrawal symptoms (i.e. aversion) (Wise & Koob, 2014). Rodents which are dependent on morphine quickly learn to avoid an environment in which they have received

naloxone, an opioid receptor antagonist (Azar et al., 2003), and dependent rodents will re-establish lever-pressing to receive intravenous morphine after a period of abstinence (Young et al., 1979). In humans, opioid addiction manifests similarly; in severe cases of addiction, one's entire life may be organized around acquiring opioids, including through engaging in hazardous or illegal activity. Thus, opioid withdrawal is a powerful negative reinforcer of addictive behaviors.

1.4 Mechanisms of Opioid Reward and Aversion

1.4.1 Anatomy of The Ventral Tegmental Area

The ventral tegmental area (VTA) has been studied extensively for its critical role in both reward and aversion (Wise, 2004). Two major dopaminergic pathways originate in the VTA: the mesolimbic pathway, which terminates in the nucleus accumbens (NAc), and the mesocortical pathway, which terminates in the medial prefrontal cortex (mPFC). Importantly, while dopamine neurons – identified through the expression or immunoreactivity of the enzyme tyrosine hydroxylase (TH) – make up the majority of neurons in the VTA, there are also significant glutamatergic and gamma-aminobutyric acid (GABA)-expressing neural populations (Nair-Roberts et al., 2008; Swanson, 1982). There is also overlap in the expression of dopamine, glutamate, and GABA (Kim et al., 2019; Miranda-Barrientos et al., 2021; Mongia et al., 2019; Yoo et al., 2016), and dopamine and glutamate are co-released from the same vesicles (Aguilar et al., 2017; Buck et al., 2021). VTA projections are largely nonoverlapping and terminate in diverse regions throughout the hindbrain, midbrain, and forebrain (Albanese & Minciacchi, 1983; Fallon,

1981; Geisler et al., 2007), and there is also significant variability in the proportion of TH-immunoreactive VTA neurons in different projection targets (Breton et al., 2019).

In addition to neurotransmitter expression and downstream projection target, VTA neurons can also be categorized into principal, secondary, and tertiary neurons based on electrophysiological properties. Principal neurons, identified as dopamine neurons by the post-hoc immunolabeling of TH, possess a hyperpolarization-activated current (I_h), have a long action potential duration, and are disinhibited by the MOR agonist [D-Ala^2, *N*-MePhe^4, Gly-ol]-enkephalin (DAMGO). Secondary neurons, which are GABA interneurons, lack an I_h, have a short action potential duration, and are hyperpolarized by DAMGO (Johnson & North, 1992). In addition, tertiary neurons have been identified which exhibit an I_h, have a long action potential duration, and are inhibited by DAMGO (Margolis et al., 2003). The excitability of principal neurons is tightly controlled by inhibitory input from GABAergic interneurons (i.e. secondary neurons) as well as GABAergic projections from the tail of the VTA, also known as the rostromedial tegmental nucleus (RMTg) (Jalabert et al., 2011).

1.4.2 Opioid Neuropharmacology

Opioids are a class of compounds which act on opioid receptors to produce morphine-like effects. Natural opioids, such as morphine and codeine, are extracted directly from the opium poppy, *Papaver somniferum*. Semi-synthetic opioids, such as heroin, oxycodone, and hydrocodone are synthesized through the acetylation or oxidation of opium precursors, while synthetic opioids, such as fentanyl and tramadol, possess a phenylpiperidine structure which is not derived from the opium poppy (Pathan & Williams, 2012). Opioids bind to the mu, delta, and kappa opioid receptors (MOR, DOR, and KOR, respectively), which are inhibitory G protein-coupled receptors

(GPCRs). GPCRs possess seven transmembrane domains and couple to intracellular G proteins; however, opioid receptors also engage G protein-independent intracellular signaling pathways (Che et al., 2021). All of these opioid receptors are agonized by a system of endogenous opioid ligands including endorphins, dynorphins, and enkephalins (Abrimian et al., 2021).

There are several challenges to studying the functional role of opioid receptors and their endogenous ligands in the context of addiction. Firstly, the expression of MOR, KOR, and DOR are widespread and overlap significantly in the brain (Valentino & Volkow, 2018). Furthermore, most endogenous opioids are nonselective, possessing affinity for multiple opioid receptors (Paul et al., 2021). Finally, while the prototypical exogenous opioids are MOR agonists, escalation of intake in the setting of dependence may achieve brain concentrations capable of binding KOR and DOR. Therefore, modern intersectional genetic approaches are necessary to parse the functional role of diverse subpopulations of opioid receptor- and opioid peptide-expressing neurons.

1.4.3 The Mu Opioid Receptor and Reward

Exogenous opioids such as morphine produce their euphoric effects by increasing dopamine release in the ventral striatum. MOR agonists increase the firing rate of VTA dopamine neurons and enhance dopamine release in the NAc when administered systemically and locally into the VTA, while MOR antagonists injected locally into the VTA decrease dopamine release in the NAc (Di Chiara & Imperato, 1988; R Spanagel et al., 1992). Rats will lever-press to receive intra-VTA infusions of morphine (Bozarth & Wise, 1981), and MOR agonist-induced conditioned place preference (CPP) can be blocked with a conditioned knockout (cKO) of MOR in the VTA (Olmstead & Franklin, 1997; Zhang et al., 2009) and with dopamine receptor antagonists (David et al., 2002). Interestingly, self-administration of and CPP produced by the MOR agonist

endomorphin-1 into the VTA was most pronounced when administered to the most posterior aspects of the VTA (Zangen et al., 2002). Therefore, opioid reward is dependent on the expression of MOR within and directly caudal to the VTA.

Opioids are understood to increase dopamine release through a disinhibitory mechanism. Intracellular recordings of rat VTA neurons in slice show that MOR agonists do not directly activate principal dopamine neurons, but rather decrease GABA-mediated synaptic input by hyperpolarizing GABA neurons (Johnson & North, 1992). Morphine also inhibits a dense population of MOR-expressing GABA neurons in the directly posterior RMTg to increase dopamine firing (Jalabert et al., 2011). Thus, opioids enhance dopamine release and produce reward by inhibiting GABA neurons in the VTA and in the neighboring RMTg, thereby disinhibiting VTA dopamine neurons.

1.4.4 The Kappa Opioid Receptor and Aversion

While activation of MOR produces reward, activation of KOR is aversive in humans and rodent models. Systemically administered KOR agonists are sufficient to induce conditioned place aversion (CPA) in rodents (Shippenberg & Herz, 1987), as are microinjections of KOR agonists into the VTA, NAc, mPFC, and lateral hypothalamus (Bals-Kubik et al., 1993). This effect is abolished through the administration of a dopamine receptor D1 antagonist locally into the NAc, chemical lesions of the NAc (Shippenberg et al., 1993), and through the conditional knockout (cKO) of KOR in dopamine neurons (Chefer et al., 2013). Consistent with this, KOR agonists decrease dopamine release in the NAc when administered systemically (Di Chiara & Imperato, 1988), intracerebroventricularly (ICV) (Rainer Spanagel et al., 1991; R Spanagel et al., 1990), and locally into the NAc (R Spanagel et al., 1992). In a cKO of KOR from dopamine neurons,

KOR agonist-induced aversion is rescued through re-expression of KOR in the VTA (Ehrich et al., 2015), and in *ex vivo* slice recordings, KOR agonists hyperpolarize VTA neurons; this effect was found to be specific to putative dopamine neurons (Margolis et al., 2003). Thus, KOR-mediated aversion is dependent on inhibition of dopamine release in the NAc from VTA neurons.

Interestingly, while KOR agonists injected directly into the VTA induce CPA, they do not decrease dopamine levels in the NAc (Devine et al., 1993), indicating KOR-mediated aversion is dependent on other brain regions as well. For example, KOR agonism also reduces dopamine release in the mPFC (Tejeda et al., 2013). Consistent with this, KOR agonists bath applied to VTA dopamine neurons in *ev vivo* slices inhibit neurons retrogradely traced from the mPFC, but not the NAc (Margolis et al., 2006). Overall, this indicates KOR expression on the terminals of NAc-projecting VTA neurons are required for KOR-mediated reductions in dopamine release, and that inhibition of dopamine release in the mPFC is also critical in the development of aversion.

Just as KOR agonism is sufficient to induce aversion, KOR antagonism is sufficient to prevent aversion. In a recent study, injection of the KOR antagonist nor-BNI into the VTA attenuated learned avoidance to bitter quinine and associated reductions in NAc dopamine release (Robble et al., 2020). Chronic pain induces aversive behaviors such as hypolocomotion and enhanced KOR agonist-induced CPA and is associated with increased dynorphin expression in the NAc in male mice. The aversive behavioral effects of chronic pain are also prevented through VTA injection of the KOR antagonist nor-BNI (Liu et al., 2019).

Taken together, these studies support a model in which MOR and KOR are functionally opposed in mesolimbic reward circuits (Figure 1). While MOR disinhibits VTA dopamine neurons through the inhibition of presynaptic GABA neurons to induce reward, KOR directly inhibits

dopamine release from VTA neurons to induce aversion. These studies also highlight the potential therapeutic benefit of KOR antagonism in aversive states.

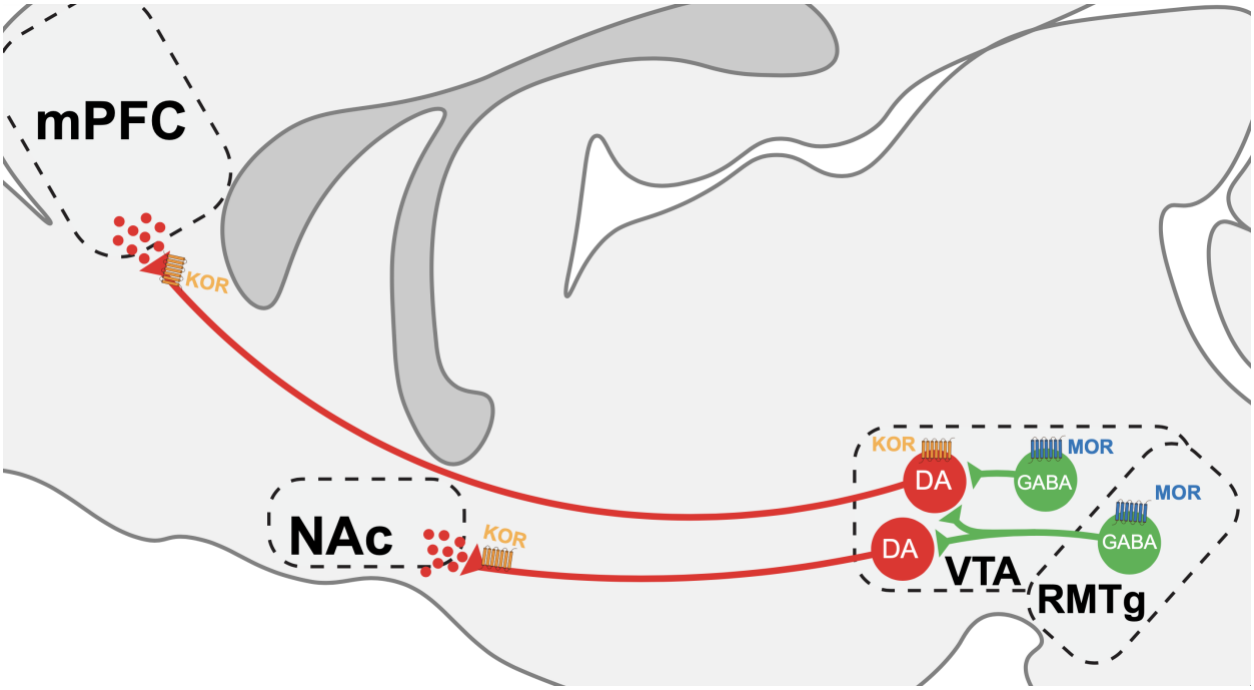

Figure 1 MOR and KOR are functionally opposed in mesolimbic reward circuits.

KOR (organge icon) is expressed on VTA dopamine neuron (red icons) cell bodies and terminals projecting to the NAc and mPFC. VTA dopamine neurons are regulated by GABA interneurons (green icons) in the VTA as well as GABA neurons projecting from the RMTg. KOR agonism inhibits dopamine release by directly inhibiting VTA dopamine neurons, while MOR (blue icon) agonism enhances dopamine release by inhibiting presynaptic GABA neurons in the VTA and RMTg.

1.5 The Kappa Overdrive Model of Opioid Addiction

1.5.1 Overarching Hypothesis

Given the abundance of evidence supporting the functional opposition of MOR and KOR on mesolimbic and mesocortical reward circuits, a delicate balance between MOR and KOR signaling is proposed to be critical in maintaining a stable affect and hedonic homeostasis. In opioid addiction, however, chronic intake of potent MOR agonists disrupts the balance of MOR and KOR signaling and results in hyperactivation of reward circuits. Tolerance and dependence are proposed to result from the adaptive recruitment of parallel aversive circuits, namely KOR and dynorphin, to regulate hyperactive reward signals (George & Koob, 2017). Upon cessation of the chronic MOR agonist, unopposed KOR agonism via increased dynorphin contributes to an acutely aversive, negative affective, and dysautonomic state which manifests as withdrawal symptoms. This is known as the kappa overdrive model of opioid addiction (Figure 2) (Helal et al., 2017).

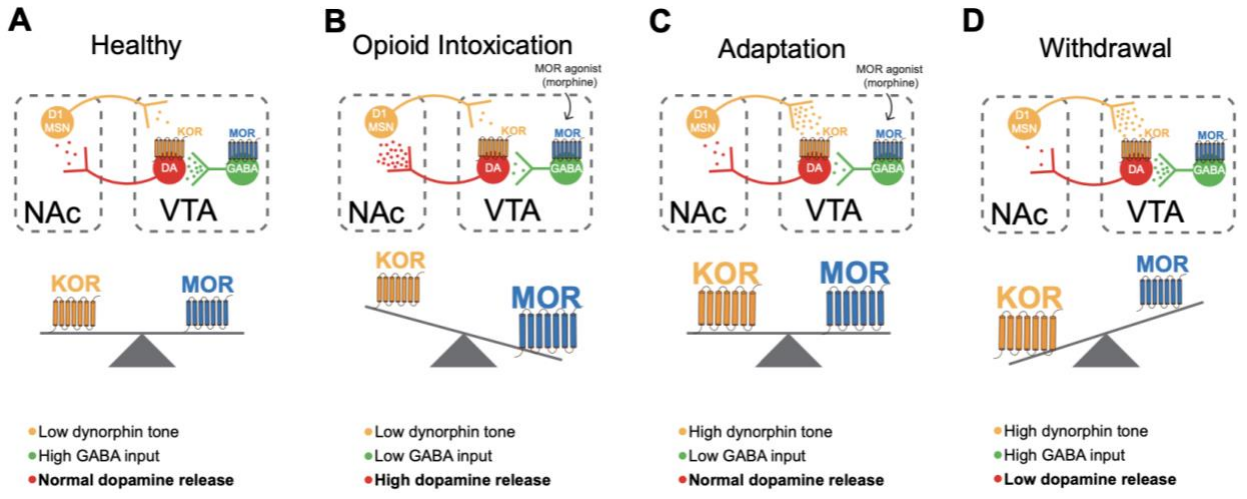

Figure 2 The kappa overdrive model of opioid addiction.

(A) In a healthy individual, MOR and KOR are in balance and dopamine release is tightly regulated by presynaptic GABA neurons. (B) Opioids like morphine inhibit GABA neurons, thereby disinhibiting dopamine release. (C)

Dynorphin and KOR are upregulated to counteract hyperactive reward signals and maintain the balance of MOR and KOR. (D) When opioids are withdrawn, unopposed dynorphin/KOR signaling leads to decreased dopamine release which manifests as opioid withdrawal symptoms.

1.5.2 Evidence Supporting the Model

The kappa overdrive model of opioid addiction is supported by a growing body of behavioral evidence. In humans, buprenorphine, a MOR partial agonist and KOR antagonist, remains one of our most effective pharmacological agents in the management of OUD (Haight et al., 2019; Lee et al., 2018). In rats self-administering oxycodone, KOR expression is increased in the hippocampus (Blackwood et al., 2019). Consistent with this, rats self-administering heroin show increased expression of prodynorphin in the NAc (Schlosburg et al., 2013), as do mice in chronic morphine withdrawal (Zan et al., 2015). In these models, local injection of nor-BNI attenuated escalation of heroin intake and withdrawal-associated depressive behaviors, respectively. KOR knockout also attenuates heroin withdrawal symptoms in mice (Lutz et al., 2014).

Interestingly, dependence on other psychoactive drug classes may also recruit KOR signaling. For example, cocaine withdrawal increases KOR activity in the VTA as measured by [35S]GTPgammaS autoradiography (Piras et al., 2010), and binge cocaine administration increases prodynorphin expression in the rat caudate-putamen (CPu) (Spangler et al., 1996). In the context of alcohol use, antagonism of KOR with nor-BNI decreases ethanol self-administration in ethanol-dependent rats without affecting intake in non-dependent animals (Walker et al., 2011). Similarly, cKO of KOR and dynorphin in the CeA decrease ethanol consumption (Bloodgood et

al., 2021). Thus, opioid dependence is associated with an upregulation of KOR and dynorphin, and inhibition of KOR and dynorphin attenuates drug self-administration and withdrawal.

1.5.3 Limitations and Contradictions

While a growing body of evidence supports the kappa overdrive model in the context of addiction, it is important to acknowledge the behavioral and pharmacological studies which contradict this model. Firstly, in some studies KOR antagonists actually precipitate or potentiate morphine withdrawal symptoms in opioid-dependent animals when administered systemically (Le Guen et al., 2003; Maldonado, Negus, et al., 1992; R Spanagel et al., 1994), ICV (R Spanagel & Shippenberg, 1993), or through microinjections into the nucleus paragigantocellularis (PGi) (Sinchaisuk et al., 2002). Furthermore, rats binge consuming cocaine show decreased expression of KOR in the substantia nigra (Spangler et al., 1996). Together, these results highlight potential weaknesses in the kappa overdrive model, and underscore the need to further investigate this model and the complex roles of KOR and dynorphin in opioid withdrawal.

1.6 Summary and Dissertation Goal

The majority of research on VTA dopamine neurons in the context of reward and addiction have focused on the NAc and mPFC projections, despite the broad collection of projections emanating from the VTA which are lesser known in their genetic makeup and functional relevance.

Furthermore, pharmacological approaches investigating KOR signaling in aversion are limited in their ability to interrogate specific projections of VTA^{KOR} neurons. Finally, much less is understood about KOR-mediated aversion in the context of opioid withdrawal, and behavioral experiments have been contradictory in rodent models. Thus, the goals of this dissertation are to characterize the anatomy of neurons in the VTA which express KOR (VTA^{KOR} neurons), determine the effects of opioid withdrawal on the activity of VTA^{KOR} neurons, and identify specific populations of VTA^{KOR} neurons critical in distinct opioid withdrawal behaviors. In Chapter 1, we characterize the neurochemical identity of VTA^{KOR} neurons and determine how chronic opioids alter the expression of KOR in the VTA and dynorphin in neurons retrogradely traced from the VTA. In Chapter 2, we measure the effects of acute morphine withdrawal on the neuronal activity and intrinsic excitability of VTA^{KOR} neurons. Consequently, in Chapter 3 we utilized an intersectional chemogenetic approach to activate VTA^{KOR} neurons *in vivo* to determine their role in acute morphine withdrawal, and found that VTA^{KOR} neurons projecting to the ventrolateral periaqueductal gray ($VTA \rightarrow vlPAG^{KOR}$ neurons) were specifically critical in opioid withdrawal-associated diarrhea and micturition. Finally, we speculate more broadly about the impacts of our findings on our current understanding of addiction pathogenesis and highlight potential future directions of this direction of study. While these results are generally supportive of the kappa overdrive model, several findings uncover a deeper complexity to the system than the kappa overdrive model describes, and prompt important questions about opioid addiction and the neural substrates underlying reward more generally.

2.0 Chapter 2: Chronic Opioids Recruit the Midbrain KOR/Dynorphin System

2.1 Introduction

The VTA is a critical hub for circuits encoding both reward and aversion (Margolis & Karkhanis, 2019). Previous work has demonstrated that KOR agonism induces aversion by inhibiting dopamine release from VTA neurons projecting to the NAc and mPFC (Bals-Kubik et al., 1993; Di Chiara & Imperato, 1988). In the context of opioid addiction, the kappa overdrive model predicts that chronic MOR agonism recruits KOR and dynorphin to inhibit dopamine neurons. Indeed, KOR agonists do selectively hyperpolarize TH-immunoreactive VTA neurons when bath applied in slice (Margolis et al., 2003). However, it is unclear which VTA subpopulations are expressed by VTA^{KOR} neurons, or the sources of dynorphin to the VTA throughout the brain. Furthermore, it is unknown how chronic opioids impact KOR expression in the VTA and dynorphin expression upstream. In this chapter we describe experiments which genetically characterize VTA^{KOR} neurons and identify the sources of dynorphin input throughout the brain. To address this, we use a combination of cre-dependent viral tracing and quantitative RNAscope fluorescence *in situ* hybridization (FISH) and the effect of chronic opioids on KOR and dynorphin expression in these circuits. Given the significant overlap of neurotransmitter expression in VTA neurons generally (Kim et al., 2019; Miranda-Barrientos et al., 2021; Mongia et al., 2019; Yoo et al., 2016), VTA^{KOR} neurons may be more functionally diverse than the kappa overdrive model predicts. Furthermore, we predict increases in dynorphin mRNA puncta in neurons retrogradely traced from the VTA in the NAc, mPFC, CPu, locus coeruleus (LC), lateral parabrachial nucleus (lPBN), ventrolateral periaqueductal gray (vlPAG), and dorsal raphe (DR).

2.2 Methods

2.2.1 Subjects

6-8 week old C57BL/6 mice were obtained from Charles River (#027). *Pdyn*^{cre} mice (Krashes et al., 2014) were maintained on a C57BL/6 background. Mice were group-housed in a temperature and humidity-controlled room maintained on a 12h/12h light-dark cycle (lights on at 0700). Animals were given *ad libitum* access to pelleted chow and water. All protocols and procedures were approved by the Institutional Care and Use Committee of the University of Pittsburgh.

2.2.2 Virus

AAVrg-hSyn-DIO-mCherry (Addgene viral prep # 50459-AAVrg) was a gift from Bryan Roth (Krashes et al., 2011).

2.2.3 Drugs

Morphine sulfate (4 mg/ml; Covetrus) and naloxone (0.3 mg/ml; Sigma Aldrich #PHR1802) were dissolved in sterile saline (0.9% NaCl) and administered intraperitoneally.

2.2.4 Stereotaxic Surgery

For retrograde tracing of dynorphin-expressing neurons, *Pdyn*^{cre} mice were anesthetized with 2% isoflurane and fixed in a stereotaxic frame. Ophthalmic ointment was applied to the eyes

and the scalp was shaved and disinfected with betadine and 70% ethanol. The cranium was exposed with a midline incision and sutures were unveiled with 3% hydrogen peroxide. Bregma and lambda suture lines were leveled to within 100 μm. A small burr hole was drilled into the skull and a custom-made 33-gauge metal needle was lowered slowly into the injection site. 250 nl of AAVrg-hSyn-DIO-mCherry was injected bilaterally into the ventral tegmental area (VTA: AP -3.30 mm, ML ±0.35 mm, DV -4.80 mm from top of skull) using a Hamilton syringe. The needle was kept in place for 15 minutes to allow for diffusion of the virus and then slowly withdrawn. The incision was closed with VetBond glue and animals were given an intraperitoneal injection of ketoprofen (5 mg/kg) and buprenorphine (0.1 mg/kg) for analgesia. Animals were given 4 weeks to recover before beginning behavioral experiments.

2.2.5 Precipitation of Morphine Withdrawal

Mice were given twice daily IP injections of morphine (Covetrus) at escalating doses for 5 days and a single dose on day 6 (day 1 AM, 10 mg/kg; day 1 PM, 20 mg/kg; day 2 AM and PM, 40 mg/kg; day 3 AM and PM, 60 mg/kg; day 4 AM and PM, 80 mg/kg; day 5 AM and PM, 100 mg/kg; day 6 AM, 100 mg/kg) in order to induce morphine dependence. 4 hours after the last dose of morphine, mice received naloxone 3 mg/kg IP to precipitate withdrawal. For RNAscope puncta quantification, mice were euthanized 30 minutes after naloxone injection.

2.2.6 Immunohistochemistry

Mice were anesthetized with ketamine/acepromazine/xylazine and transcardially perfused with 10 mL PBS followed by 4%-PFA-PBS. Whole brains and spinal cords were dissected and

post-fixed in 4%-PFA-PBS for a minimum of 2h to overnight, and then cryoprotected in 30% sucrose-PBS until tissue sank. 60-μm sections were sliced in a cryostat. Slices were stained free-floating (brain) or fixed to Superfrost Plus slides (spinal cord) as previously described (Nguyen et al., 2022). Briefly, sections were washed with PBS and blocked in 5% normal donkey serum (NDS) in 0.2% Triton-X in PBS (PBS-Tx). Sections were incubated in rabbit anti-RFP (Rockland) primary antibody overnight at room temperature in 5% NDS-PBS-Tx. After washing with PBS-Tx, sections were incubated in donkey anti-rabbit 555 (Invitrogen) secondary antibody for 2 hours at room temperature. Sections were mounted on Superfrost Plus slides and coverslipped with ProLong Gold with DAPI.

2.2.7 RNAscope Fluorescence *in situ* Hybridization

Mice were anesthetized with 2% isoflurane and decapitated. Whole brains were rapidly dissected and flash-frozen in isopentane. 14-μm coronal sections were mounted to Superfrost Plus slides and immediately stored at -80C. The next day, multiplex fluorescence *in situ* hybridization was performed according to the manufacturer's specifications (ACD Bio). Briefly, sections were fixed in 4% paraformaldehyde in phosphate-buffered saline (4% PFA-PBS) for 15 minutes, dehydrated, and treated with protease IV for 15 minutes. Sections were then hybridized with gene-specific probes to mouse Oprk1 (ACD Bio # 316111), Th (ACD Bio # 317621), Slc17a6 (ACD Bio # 319171), and Slc32a1 (ACD Bio # 319191), Oprm1 (ACD Bio # 315841) and Pdyn (ACD Bio # 318771). Slides were counterstained with DAPI (ACD Bio # 320858) and coverslipped with ProLong Gold Antifade Reagent with DAPI. Three-plex positive (ACD Bio # 320881) and negative (ACD Bio # 320871) controls were used.

2.2.8 Imaging

Sections were imaged at full tissue thickness using an upright epifluorescent microscope (Leica DMi8 Epifluorescent Microscope with 2.5x, 5x, 10x, 20x, or 40x objectives). All analysis was completed off-line using FIJI software (Image J, NIH), Python, and R. For retrograde tracing, presence of mCherry-immunoreactive cell bodies were manually identified based on Paxinos and Franklin's mouse brain atlas (Paxinos & Franklin, 2012).

2.2.9 RNAscope Puncta Quantitative Analysis Pipeline

To quantify Oprk1 and Pdyn cells and puncta in RNAscope images, a custom quantification method in Python and R was developed. Leica multiplexed images were first converted into TIF format using a FIJI macro. A custom python script was written to detect DAPI nuclei using Mesmer, a pre-trained DeepCell model for cell or nuclei detection, and detect puncta in the RNAscope channels using Polaris, a pre-trained DeepCell model for puncta detection. These scripts were created based on tutorials available at https://github.com/vanvalenlab/deepcell-tf/tree/master/notebooks/applications (Greenwald et al., 2022). Briefly, the custom python script reads the images, loads the pretrained models, predicts the puncta, predicts the nuclei. It was determined that expanding the nuclei shape by 3 extra pixels cell perimeters that include cytosolic RNAscope puncta. Finally, the script outputs the results for puncta segmentation (puncta location, relative image intensity values), results for nuclei segmentation (location, size, roundness, etc), and overlaid images for qualitative assessment of segmentation performance. Next, the segmentation of all images were analyzed together to filter out nuclei, count puncta per nuclei, and calculate the number of cells or puncta per cell for each image using the same thresholds across

the dataset. We exclude outlier nuclei using automatic multivariate outlier detection using rstatix::mahalanobis_distance() with default parameters on the nuclei morphological features. The optimal puncta per cell thresholds were selected to most closely align with manual cell counts which were performed for a subset of the data, determined by the highest Spearman correlation between manual counts and computation detection-based thresholding of puncta per cell. For quantification of Oprk1 in the VTA, we used the following thresholds to determine a positive cell: 8 Oprk1 puncta per cell to be Oprk1+, 5 Fos puncta per cell to be Fos+. For the quantification of Pdyn in retrogradely traced cells, we used the following thresholds to determine a positive cell: 8 mCherry puncta per cell to be mCherry+, 5 Oprm1 puncta per cell to be Oprm1+, and 10 Dyn puncta per cell to be Dyn+.

2.2.10 Code Availability

The python and Rscripts for RNAscope automatic detection analyses will be available to individual members of the scientific community upon request to the corresponding authors. The code exists at the following private link after access is granted: https://github.com/pfenninglab/RNAscope_processing_with_DeepCell.

2.2.11 Statistical Analysis

All statistical analyses were analyzed with GraphPad Prism 9.0. Values are represented as mean ± SEM. Statistical significance was assessed using an unpaired t-test or two-way ANOVA followed by Holm-Sidak post-hoc test; parametric tests were justified by the normal distribution of reported data sets. Significance was indicated by $p < 0.05$. The n for each experiment is

described in the figure legends; three images were averaged per animal. Sample sizes were selected based on previously published histological and RNAscope experiments (Chiang et al., 2020; Nguyen et al., 2022).

2.3 Results

2.3.1 VTA^{KOR} neurons are neurochemically diverse

Rewarding and aversive information is conveyed from the VTA to many regions of the brain, particularly through the release of dopamine in the NAc (Di Chiara & Imperato, 1988). Previous electrophysiology studies have demonstrated that VTA dopamine neurons are regulated by presynaptic GABA interneurons, and selectively inhibited by KOR agonists (Jalabert et al., 2011; Johnson & North, 1992; Margolis et al., 2003). However, the neurochemical identity of all VTA neurons expressing KOR (VTA^{KOR} neurons) and their genetic relationship to local MOR and dynorphin neurons has yet to be completed. To address this, we performed RNAscope FISH in the VTA to quantify colocalization of the *Oprk1* gene with *Oprm1*, *Pdyn,* and the cell type-specific marker genes *Th, Slc17a6,* and *Slc32a1* to identify dopaminergic, glutamatergic, and inhibitory neurons, respectively (Figure 3). Out of 1107 cells, we did not identify any Oprk1/Oprm1 dual-labeled cells or Oprk1/Pdyn dual-labeled cells, indicating no overlap between KOR and MOR neurons, or KOR and dynorphin neurons in the VTA (Figure 3A). We identified ~10% of Oprm1 cells which were dual-labeled with Pdyn, and ~30% of Pdyn neurons which were dual-labeled with Oprm1, indicating functional overlap between these populations (Figure 3A). These results

are consistent with prior studies suggesting MOR and dynorphin neurons are presynaptic to KOR neurons and represent functionally distinct populations in the VTA.

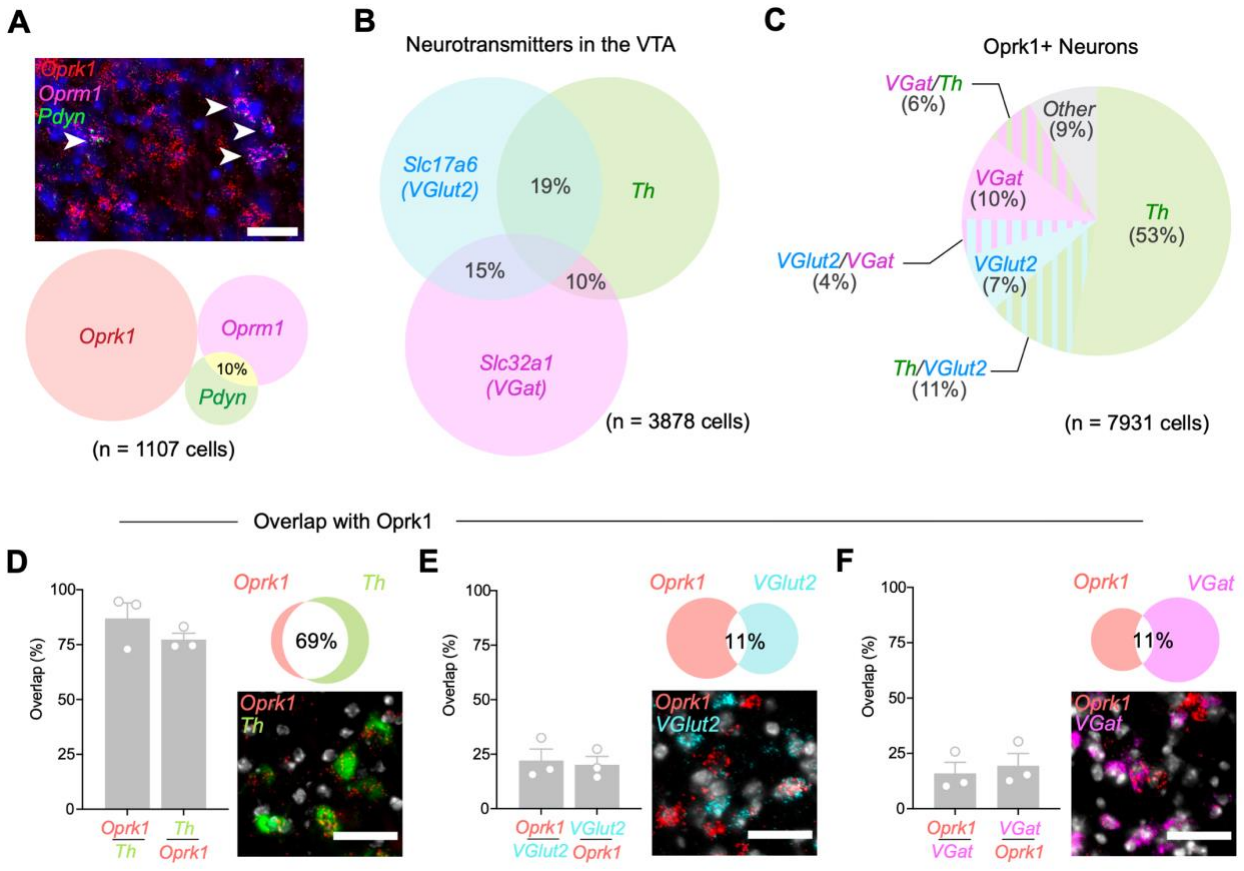

Figure 3 RNAscope FISH characterization of VTA^{KOR} neurons reveals anatomical distinction from MOR neurons and cell type diversity.

(A) Top: representative image of RNAscope for *Oprk1* (red), *Oprm1* (magenta), and *Pdyn* (green) in the VTA. White arrows indicate *Oprm1/Pdyn* dual-labeled neurons. Scale bar = 50 µm. Bottom: Venn diagram of *Oprk1*, *Oprm1*, and *Pdyn* neurons counted. n = 1107 cells from three mice, with 4-6 images quantified from each mouse. 10% indicates percentage of *Oprm1* cells in the VTA which also express *Pdyn*. (B) Venn diagram of *Th*, *Slc17a6*, and *Slc32a1* neuron co-expression in the VTA. n = 3878 cells from three mice, with 4-6 images counted from each mouse. (C) Pie chart summarizing colocalization of *Th*, *Slc17a6*, and *Slc32a1* with *Oprk1* in the VTA. n = 7931 cells from six mice, with 4-6 images counted from each mouse. (D) Left: quantification of colocalization of *Oprk1* and *Th* in the VTA. Bottom: representative image of RNAscope for *Oprk1* and *Th*. Scale bar = 50 µm. Top: Venn diagram of *Oprk1* and *Th* overlap. 69% denotes the percentage of all *Oprk1* and *Th* neurons which overlap. (E) Left:

quantification of colocalization of *Oprk1* and *Slc17a6* (Vglut2) in the VTA. Bottom: representative image of RNAscope for *Oprk1* and *Slc17a6* (Vglut2). Scale bar = 50 µm. Top: Venn diagram of *Oprk1* and *Slc17a6* (VGlut2) overlap. 11% denotes the percentage of all *Oprk1* and *Vglut2* neurons which overlap. (F) Left: quantification of colocalization of *Oprk1* and *Slc32a1 (*VGat) in the VTA. Bottom: representative image of RNAscope for *Oprk1* and *VGat.* Scale bar = 50 µm. Top: Venn diagram of *Oprk1* and *VGat* overlap. 11% denotes the percentage of all *Oprk1* and *VGat* neurons which overlap. Each dot represents an individual mouse (n = 3 mice) and 4-6 images were aveaged per mouse. Group data is represented as mean ± SEM.

Next, we sought to characterize the neurotransmitter expression in *Oprk1* neurons. Consistent with previous studies (Kim et al., 2019; Miranda-Barrientos et al., 2021; Mongia et al., 2019; Yoo et al., 2016), we found considerable overlap in *Th, Slc17a6,* and *Slc32a1* neural populations in the VTA, with ~19% overlap between *Th* and *Slc17a6* neurons, ~10% overlap between *Th* and *Slc32a1* neurons, and ~15% overlap between *Slc17a6* and *Slc32a1* neurons in the VTA (Figure 3B). We next sought to determine which of these VTA cell types express *Oprk1*. Interestingly, *Oprkl* neurons expressed all three cell type-specific markers, with the highest overlap with *Th* (~53% *Th* alone, ~11% *Th/Vglut2,* and ~10% *Th/VGat*); however ~7% of *Oprk1* neurons also co-expressed *Vglut2* alone, ~6% co-expressed *VGat* alone, and ~4% co-expressed *VGlut2/VGat*) (Figure 3C). When looking more closely at the distribution of *Oprk1* in *Th, VGlut2,* and *VGat* neurons, we found ~87% of *Th* neurons, ~22% of *VGlut2* neurons, and ~16% of *VGat* neurons co-express *Oprk1* (Figure 3D-F). Together, these results suggest that, while *Oprk1* expression is abundant in dopamine neurons, VTA^{KOR} neurons are diverse and likely represent multiple subpopulations of VTA neurons.

2.3.2 Chronic opioids do not increase KOR expression in the VTA

Given KOR is expressed in diverse cell types in the VTA, we hypothesized chronic opioids how chronic opioids impact expression of the *Oprk1* gene in the VTA. To explore this, we quantified Oprk1 expression in VTA^{KOR} neurons in opioid naïve and opioid-dependent mice after administration of morphine 10 mg/kg (Figure 4A). We achieved this through the development and use of a custom automated machine learning analytical pipeline in Python and R to quantify Oprk1+ cells and number of puncta in each cell (Figure 4B-C). We found that chronic morphine did not significantly increase the number of KOR+ cells (Figure 4D), the total number of KOR puncta (Figure 4E), or the number of KOR puncta per cell in the VTA (Figure 4F; F statistics reported in Table 1). These results indicate that neither chronic nor acute morphine significantly alter KOR expression in the VTA.

2.3.3 Chronic opioids increase dynorphin expression in VTA input regions

Given the importance of midbrain dynorphin and KOR signaling in aversive states, we sought to identify all the dynorphin-expressing afferents into the VTA throughout the brain. Toward this end, a Cre-dependent retrograde AAV encoding mCherry was stereotaxically delivered into the VTA of $Pdyn^{cre}$ mice (Figure 5A). We observed Pdyn-expressing afferents originating from numerous regions of the brain (Figure 5B-D). In the rostral forebrain, consisting of the cortex and basal ganglia, we identified mCherry-immunoreactive cell bodies in the medial prefrontal cortex (mPFC), NAc core (NAcC), and caudate-putamen (CPu), and ventral pallidum (Figure 5B). In limbic structures such as the thalamus, hypothalamus, and epithalamus, we identified mCherry-immunoreactive cell bodies in the bed nucleus of the stria terminalis (BNST),

arcuate nucleus (Arc), periventricular nucleus of the hypothalamus (PVH), and the central amygdala (CeA) (Figure 5C). In the brainstem, consisting of the midbrain, pons, and medulla, we identified mCherry-immunoreactive cell bodies, in the ventrolateral periaqueductal gray (vlPAG), dorsal raphe (DR), lateral parabracial nucleus (lPBN), locus coeruleus (LC), and the nucleus tractus solitarius (NTS) (Figure 5D). Thus, the VTA receives dynorphin input from several brain regions implicated in hedonic homeostasis, aversion, autonomic dysregulation, and gastrointestinal motility.

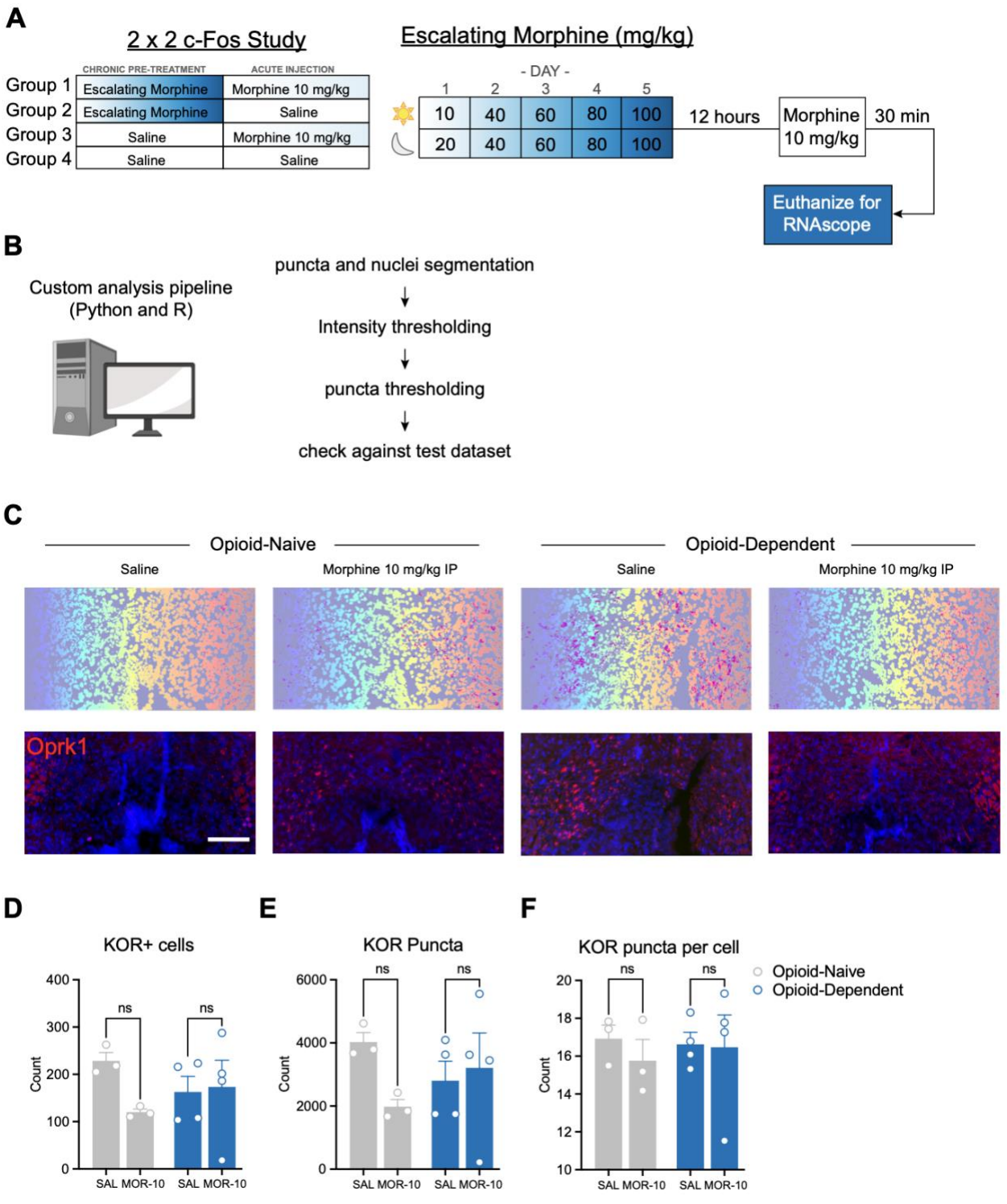

Figure 4 Chronic opioids do not significantly increase KOR expression in the VTA

(A) Experimental design. Left: C57BL/6 mice were split into four groups in a 2x2 study based on chronic pre-treatment and acute injection. Right: mice received escalating doses of morphine or saline IP for 5 days. 12 hours

later, mice received a smaller dose of morphine (10 mg/kg) IP or saline, and were euthanized 30 minutes later for RNAscope. (B) Illustration of the automated RNAscope punctal analysis pipeline. (C). Top: Representative machine counts of Oprk1 puncta in VTA RNAscope. Bottom: corresponding RNAscope image of Oprk1 in VTA RNAscope. Scale bar = 250 µm. (D) Quantification of number of KOR+ cells in the VTA of opioid-naïve and opioid-dependent mice receiving an acute injection of morphine 10 mg/kg. Gray bars are opioid-naïve mice, blue bars are opioid-dependent mice. Each dot represents a single mouse (n = 3-4 mice per group), with 2-3 images averaged per animal. Data analyzed via 2-way ANOVA. Group data is represented as mean ± SEM. (E) Quantification of total number KOR puncta in the VTA of opioid-naïve and opioid-dependent mice receiving an acute injection of morphine 10 mg/kg. Gray bars are opioid-naïve mice, blue bars are opioid-dependent mice. Each dot represents a single mouse (n = 3-4 mice per group), with 2-3 images averaged per animal. Data analyzed via 2-way ANOVA. Group data is represented as mean ± SEM. (F) Quantification of number of Oprk1+ puncta per cell in the VTA of opioid-naïve and opioid-dependent mice receiving an acute injection of morphine 10 mg/kg. Gray bars are opioid-naïve mice, blue bars are opioid-dependent mice. Each dot represents a single mouse (n = 3-4 mice per group), with 2-3 images averaged per animal. Data analyzed via 2-way ANOVA. Group data is represented as mean ± SEM.

Table 1 Summary of F Statistics for ANOVAs in Chapter 2

Sub-Figure	Test	Effect	F (DFn, DFd)	p value	Significant?
4D	2-way RM ANOVA with Sidak correction	Interaction	F (1, 10) = 2.291	P=0.1611	No
		Acute Drug	F (1, 10) = 1.534	P=0.2438	No
		Morphine Dependence	F (1, 10) = 0.02540	P=0.8765	No
4E	2-way RM ANOVA with Sidak correction	Interaction	F (1, 10) = 2.571	P=0.1399	No
		Acute Drug	F (1, 10) = 1.150	P=0.3088	No
		Morphine Dependence	F (1, 10) = 3.608e-005	P=0.9953	No
4F	2-way RM ANOVA with Sidak correction	Interaction	F (1, 10) = 0.1729	P=0.6863	No
		Acute Drug	F (1, 10) = 0.2953	P=0.5988	No
		Morphine Dependence	F (1, 10) = 0.02876	P=0.8687	No

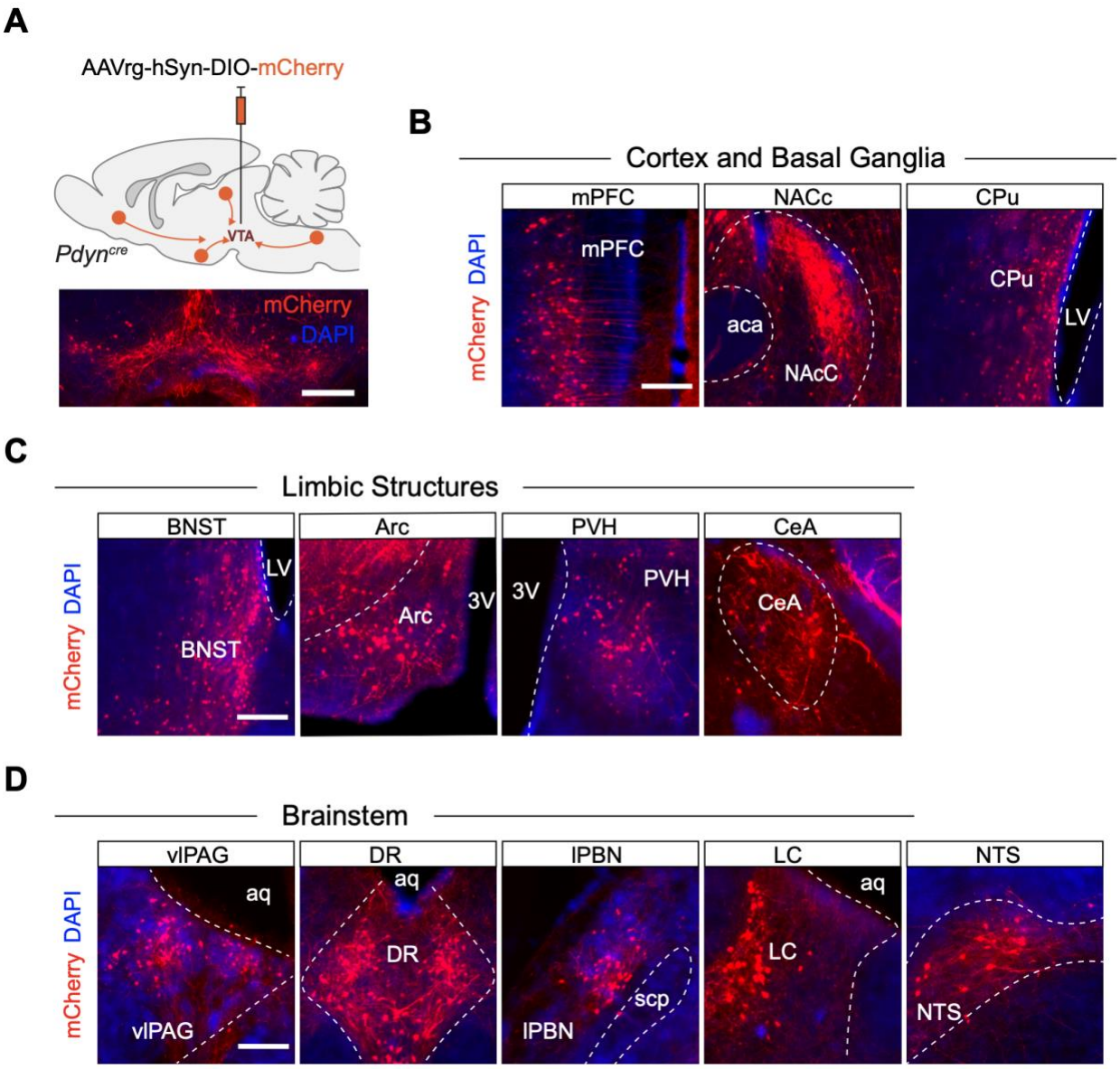

Figure 5 the VTA receives dynorphin input from several forebrain, midbrain, and hindbrain structures.

(A) Top: illustration of viral delivery of mCherry into Pdyn input neurons. Bottom: representative image of a mouse VTA slice containing mCherry (red)-immunoreactive fibers. Scale bar = 250 µm. (B) Representative images of regions in the cortex and basal ganglia with mCherry (red)-immunoreactive cell bodies. mPFC, medial prefrontal cortex; PrL, NAcC, nucleus accumbens core; CPu, caudate putamen. Scale bar = 100 µm. (C) Representative images of regions in the caudal forebrain with mCherry (red)-immunoreactive cell bodies. BNST, bed nucleus of the stria terminalis; Arc, arcuate nucleus; PVH, periventricular nucleus of the hypothalamus; CeA, central amygdala. Scale bar = 100 µm. (D) Representative images of regions in the midbrain, pons and medulla with mCherry (red)-

immunoreactive cell bodies.vlPAG, ventrolateral PAG; DR, dorsal raphe; lPBN, lateral parabrachial nucleus; LC, locus coeruleus; NTS, nucleus tractus solitarius. Scale bar = 100 μm.

After identifying the diverse sources of dynorphin input into the VTA above, we next sought to determine whether chronic opioids increase dynorphin expression in these regions. To achieve this, we performed quantitative RNAscope FISH in neurons from eight candidate brain regions retrogradely labeled from the VTA (Figure 6). Specifically, a Cre-dependent retrograde AAV encoding mCherry was stereotaxically delivered into the VTA of *Pdyn*^{cre} mice (Figure 6A). 5 weeks after surgery, mice were split into chronic morphine or saline groups and received escalating doses for 6 days, followed by naloxone 3 mg/kg to induce withdrawal (Figure 6B). We then performed RNAscope for *Pdyn*, *mCherry,* and *Oprm1* in slices from 8 major dynorphin-expressing regions: the CPu, DR, LC, NAc, vlPAG, lPBN, mPFC, and VTA. Images were then analyzed through a custom automated machine learning pipeline through Python and R (Figure 6C-D). In our analysis we quantified number of Pdyn+ cells (Figure 6E), number of Pdyn puncta per Pdyn+ cell (Figure 6F), and number of Pdyn puncta per Pdyn+/mCherry+ cell (Figure 6G). Using unpaired, uncorrected t-tests, we identified that chronic morphine may induce increases in the number of Pdyn+ cells in the LC (Figure 6E) and increased the number of Pdyn puncta per cell in the DR (Figure 6F). Our screen did not yield any notable effects of chronic opioids in Pdyn puncta in neurons co-expressing mCherry (Figure 6G). Additionally, we quantified the proportion of Pdyn+ cells which co-expressed Oprm1 (Figure 6H). We found varying levels of Oprm1 expression in Pdyn-expressing brain regions (23% in the CPu, 24% in the DR, 42% in the LC, ~16% in the NAc, ~34% in the vlPAG, ~40% in the lPBN, ~28% in the mPFC, and ~59% in the VTA). Taken together, these results are suggestive of two dynorphin-mediated mechanisms by which chronic opioids may be altering the mesolimbic reward circuitry: via increasing the number of cells which express Pdyn mRNA transcript, and increasing the expression level of Pdyn

transcript within Pdyn+ cells. Follow-up studies are necessary to further elucidate the effects of chronic opioids on dynorphin expression in the dorsal raphe and locus coeruleus.

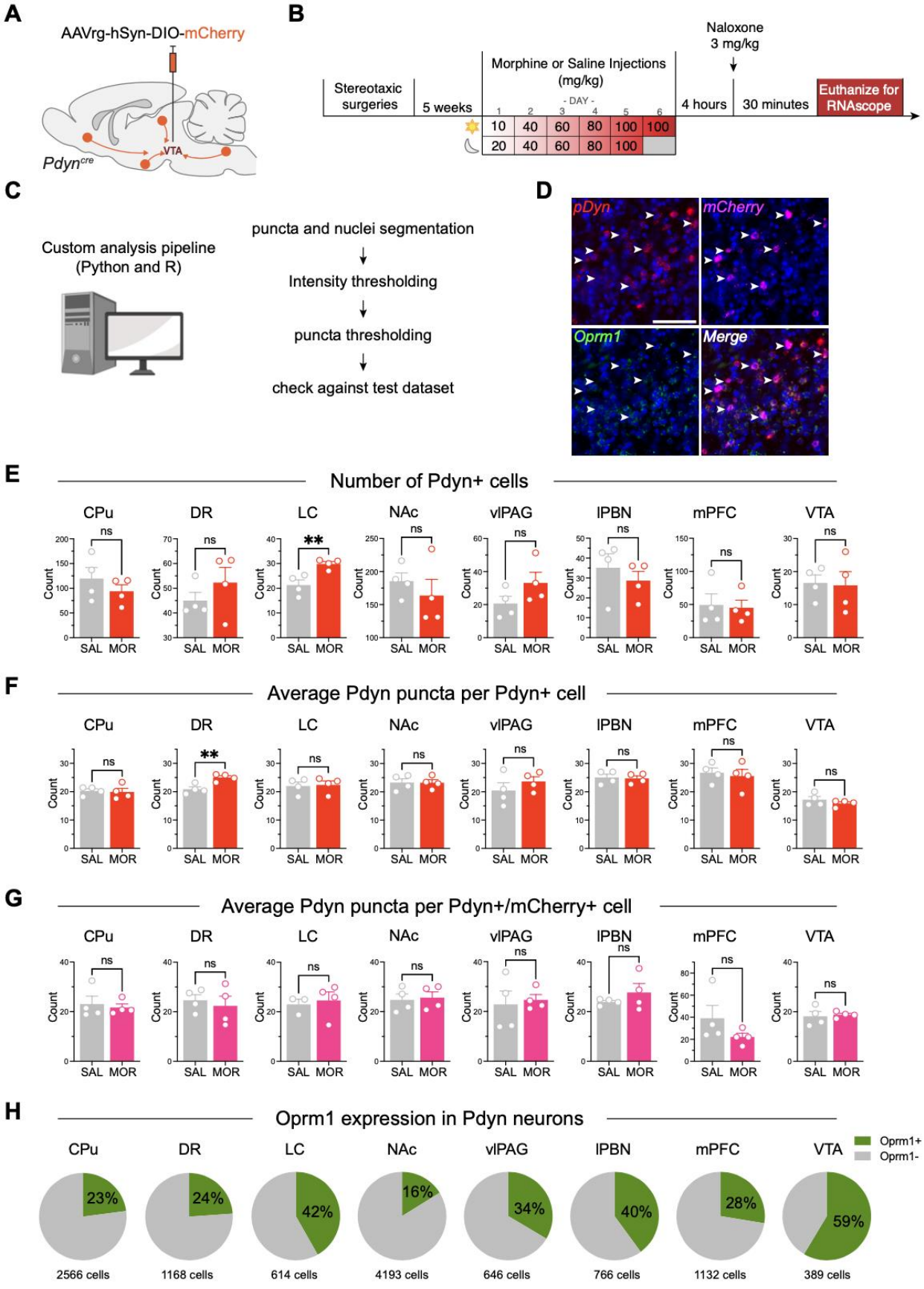
A
AAVrg-hSyn-DIO-mCherry
VTA
Pdyn^cre
B
Naloxone
3 mg/kg
Morphine or Saline Injections
(mg/kg)
- DAY -
Stereotaxic surgeries
5 weeks
4 hours
30 minutes
Euthanize for RNAscope
10 40 60 80 100 100
20 40 60 80 100
C
Custom analysis pipeline
(Python and R)
puncta and nuclei segmentation
Intensity thresholding
puncta thresholding
check against test dataset
D
pDyn
mCherry
Oprm1
Merge
E
Number of Pdyn+ cells
F
Average Pdyn puncta per Pdyn+ cell
G
Average Pdyn puncta per Pdyn+/mCherry+ cell
CPu
DR
LC
NAc
vlPAG
lPBN
mPFC
VTA
Count
SAL MOR
ns
**
H
Oprm1 expression in Pdyn neurons
Oprm1+
Oprm1-
23%
24%
42%
16%
34%
40%
28%
59%
2566 cells
1168 cells
614 cells
4193 cells
646 cells
766 cells
1132 cells
389 cells

Figure 6 Preliminary screen for chronic opioid-induced increases in Pdyn expression in VTA input regions. (A) illustration of viral delivery of mCherry into Pdyn input neurons. (B) Experimental design. Five weeks after viral delivery of mCherry, *Pdyn*^{cre} mice received escalating doses of morphine or saline IP for 6 days followed by naloxone, and were euthanized 30 minutes later for RNAscope. (C) Illustration of the automated RNAscope punctal analysis pipeline. (D) Representative RNAscope image for *Pdyn* (red), *mCherry* (magenta), and *Oprm1* (green) in the lPBN, with Pdyn/*mCherry* co-expressing cells marked with white arrows. Scale bar = 100 µm. (E) Automated quantification of the number of Pdyn+ neurons in the CPu, DR, LC, NAc, vlPAG, lPBN, mPFC, and VTA. Gray bars are saline mice, and red bars are morphine mice. Each dot represents one mouse (n = 4 per group), with 3 images averaged per mouse, and group data is represented as mean ± SEM. **indicates statistically different (two-tailed unpaired and uncorrected t-test, $p<0.01$). (F) Automated quantification of the average number of Pdyn puncta per Pdyn+ neuron in the CPu, DR, LC, NAc, vlPAG, lPBN, mPFC, and VTA. Gray bars are saline mice, and red bars are morphine mice. Each dot represents one mouse (n = 4 per group), with 3 images averaged per mouse, and group data is represented as mean ± SEM. **indicates statistically different (two-tailed unpaired and uncorrected t-test, $p<0.01$). (G) Automated quantification of the average number of Pdyn puncta per Pdyn+/mCherry+ neuron in the CPu, DR, LC, NAc, vlPAG, lPBN, mPFC, and VTA. Gray bars are saline mice, and red bars are morphine mice. Each dot represents one mouse (n = 4 per group), with 3 images averaged per mouse, and group data is represented as mean ± SEM. (H) Quantification of the average percentage of Pdyn+ neurons co-express Oprm1 in the CPu, DR, LC, NAc, vlPAG, lPBN, mPFC, and VTA. Gray indicates Oprm1- neurons while green indicates Oprm1+ neurons. Results were pooled from all 8 mice, and the total number of cells involved in the quantification is listed below each pie chart.

2.4 Discussion

In this chapter we provided molecular evidence suggesting that chronic opioids may increase midbrain KOR signaling through dynorphin upregulation. Using RNAscope FISH, we characterized the neurochemical identity of VTA^{KOR} neurons, finding significant dopaminergic,

glutamatergic, and inhibitory subpopulations. We then used an automated quantitative RNAscope analytical pipeline to investigate KOR expression in the VTA, as well as dynorphin expression in VTA input regions, in acute and chronic opioid exposures. Furthermore, we used genetically engineered mice expressing Cre recombinase under the Pdyn promoter, thereby allowing us to virally target and characterize the anatomy of this population. Retrograde labeling of dynorphin-expressing neurons from the VTA identified distinct input regions throughout the forebrain, midbrain, and hindbrain. In chronic opioid use, KOR expression does not change in the VTA, but a screen of VTA input neurons identified the LC and DR as candidate regions that may show increases in Pdyn expression. . Together, these experiments reveal that, insofar as the kappa overdrive model is correct, it likely involves changes other than the upregulation of either *Oprk1* or *Pdyn* mRNA as its underlying mechanism.

A novel finding through our RNAscope characterization of VTA^{KOR} neurons was that this population was completely distinct from VTA^{MOR} neurons. This is consistent with electrophysiological evidence that MOR and KOR are functionally opposed in the VTA; KOR agonists acts solely on VTA principal neurons (Margolis et al., 2003, 2006) while MOR agonists act on presynaptic GABA interneurons (Johnson & North, 1992). Additionally, a subpopulation of MOR neurons co-expresses dynorphin, representing a novel mechanism by which secondary GABA interneurons modulate the activity of principal dopamine neurons in the VTA. Interestingly, while the majority of VTA^{KOR} neurons are dopaminergic, we additionally found subpopulations expressing glutamatergic and inhibitory markers. This is not completely inconsistent with previous VTA recordings in slice, wherein KOR agonists selectively inhibit TH-expressing neurons (Margolis et al., 2003), as KOR may be localized to the axon or terminal in these glutamatergic and inhibitory subpopulations. It is also interesting that, despite the finding

that ~20% of KOR neurons express an inhibitory neural marker, none of them express MOR. This suggests we have identified a novel population of KOR-expressing inhibitory neurons in the VTA not previously identified via electrophysiology, perhaps due to localization of the KOR protein beyond the cell body. An important future direction for these studies will be the anatomical, electrophysiological, and functional characterization of the lesser understood glutamatergic and GABAergic subpopulations of VTA^{KOR} neurons.

An additional novel finding from these experiments was that dynorphin expression increased in the LC and DR in acute opioid withdrawal via increasing the number of dynorphin-expressing neurons and increasing the expression of dynorphin mRNA transcript in each cell, respectively. However, no effect was not found in the subpopulation of dynorphin neurons which projected to the VTA. This could be because the increase in dynorphin expression is more pronounced in neurons projecting to regions with VTA^{KOR} neuron terminals, such as the NAc. For example, a recent study found dynorphin neurons in the DR induced social deficits in opioid withdrawal by modulating serotonin neurons projecting to the NAc (Pomrenze et al. 2022). This is consistent with prior work showing that in KOR KO mice, specifically re-expressing KOR in dorsal raphe serotonergic neurons was sufficient to reinstate KOR agonist-induced CPA (Land et al., 2009). Interestingly, we did not find effects of acute opioid withdrawal on prodynorphin mRNA transcript in the NAc. This is not consistent with previous studies showing that prolonged heroin self-administration (Schlosburg et al., 2013) and prolonged morphine abstinence (Zan et al., 2015) both increase dynorphin protein levels and mRNA expression, respectively, in the NAc. This difference in findings could be because differences in dynorphin levels in the withdrawal state do not manifest in the acute period, but rather develop over longer time periods. It is also possible we did not appreciate differences in dynorphin expression because the effects are restricted to a

specific subregion of the NAc such as the core or shell, or along the rostrocaudal or dorsoventral axes. Further studies are warranted to characterize the cell types in the NAc which express dynorphin, the effects of opioids on these neurons, and whether increases in dynorphin signaling occur in the VTA or other regions.

In the present study, our characterization of KOR/dynorphin dynamics in the VTA is limited to expression of mRNA transcript. However, a depression of receptor-ligand signaling can occur via several additional mechanisms, including increased receptor internalization and/or degradation, bias towards or away from G-protein-dependent signaling cascades, altered phosphorylation state of the receptor, increased dynorphin uptake or degradation, or changes in synaptic strength. Furthermore, it is important to emphasize again that, while our investigation of withdrawal-associated increases in dynorphin expression was designed to be unbiased, it was also uncorrected due to the nature of the repeated testing. Follow-up experiments are necessary to investigate further the relative roles of the DR and LC in opioid withdrawal-associated KOR/dynorphin changes more specifically.

An important detail not addressed in the analysis described here is the effect of chronic opioids and opioid withdrawal on Oprm1 expression in VTA interneurons and longer-range afferents. Subsequent analyses of our dataset will need to investigate this. Additionally, it is unknown how chronic opioid-induced alterations in prodynorphin mRNA transcript (or lack thereof) correlate with the release of dynorphin peptide onto VTAKOR neurons. Further studies are warranted to distinguish whether opioid-induced increases in dynorphin expression lead to increases in dynorphin release in the VTA or other regions.

3.0 Chapter 3: Opioids Decrease VTA^{KOR} Neuronal Activity

3.1 Introduction

Chronic opioids have been shown to induce genetic changes as well as structural and cellular plasticity within the VTA (Browne et al., 2020, 2023; Mazei-Robison & Nestler, 2012). For example, chronic opioids have been shown to reduce the area and perimeter of putative VTA dopamine neurons in rats (Sklair-Tavron et al., 1996; Spiga et al., 2003) and reduce dopamine release in the NAc (Mazei-Robison et al., 2011). However, the role of KOR and dynorphin recruitment in this phenotype is not understood, or whether these genetic and structural changes lead to alterations in neuronal activity or excitability in VTA^{KOR} neurons specifically. In this chapter we describe experiments which determine the effects of chronic opioids and opioid withdrawal on the activity of VTA^{KOR} neurons. To address this, we quantify morphine-induced c-Fos, a marker for neuronal activity, in VTA^{KOR} neurons of mice in spontaneous opioid withdrawal. We also generate an *Oprk1*$^{cre;tdTomato}$ mouse and perform *ex vivo* patch clamp electrophysiology in VTA slices from mice in acute naloxone-precipitated opioid withdrawal, and quantify the effects of opioid withdrawal on excitatory and inhibitory postsynaptic currents (EPSCs and IPSCs). We predict chronic morphine followed by acute withdrawal will decrease neuronal activity and excitability of VTA^{KOR} neurons through increased IPSCs.

3.2 Methods

3.2.1 Subjects

6-8 week old C57BL/6 mice were obtained from Charles River (#027). *Oprk1*$^{cre;tdTomato}$ mice were generated by crossing *Oprk1*^{cre} mice (Cai et al., 2016) with *Ai14* mice, which express tdTomato following Cre-mediated recombination (Madisen et al., 2010). 3-4 week old *Oprk1*^{cre}*;Rosa*^{tdT} mice were used for electrophysiology experiments. Mice were group-housed in a temperature and humidity-controlled room maintained on a 12h/12h light-dark cycle (lights on at 0700). Animals were given *ad libitum* access to pelleted chow and water. All protocols and procedures were approved by the Institutional Care and Use Committee of the University of Pittsburgh.

3.2.2 Drugs

Morphine sulfate (4 mg/ml; Covetrus) and naloxone (0.3 mg/ml; Sigma Aldrich #PHR1802) were dissolved in sterile saline (0.9% NaCl) and administered intraperitoneally.

3.2.3 Precipitation of Morphine Withdrawal

Mice were given twice daily IP injections of morphine (Covetrus) at escalating doses for 5 days and a single dose on day 6 (day 1 AM, 10 mg/kg; day 1 PM, 20 mg/kg; day 2 AM and PM, 40 mg/kg; day 3 AM and PM, 60 mg/kg; day 4 AM and PM, 80 mg/kg; day 5 AM and PM, 100 mg/kg) in order to induce morphine dependence. For patch clamp electrophysiology in slice, mice

received one last injection of morphine 100 mg/kg IP followed by naloxone 3 mg/kg to precipitate withdrawal, and were euthanized 30-45 minutes after naloxone injection. For morphine-induced Fos RNAscope, mice received an acute injection of morphine 10 mg/kg or saline on day 6, and were euthanized 20-30 minutes after the last morphine injection. For morphine-induced c-Fos immunoreactivity, mice received an acute injection of morphine 10 mg/kg one week after inducing dependence and were euthanized 2 hours after the last morphine injection.

3.2.4 Fos and Oprk1 RNAscope Fluorescence *in situ* Hybridization

Mice were anesthetized with 2% isoflurane and decapitated. Whole brains were rapidly dissected and flash-frozen in isopentane. 14-μm coronal sections were mounted to Superfrost Plus slides and immediately stored at -80C. The next day, multiplex fluorescence *in situ* hybridization was performed according to the manufacturer's specifications (ACD Bio). Briefly, sections were fixed in 4% paraformaldehyde in phosphate-buffered saline (4% PFA-PBS) for 15 minutes, dehydrated, and treated with protease IV for 15 minutes. Sections were then hybridized with gene-specific probes to mouse Oprk1 (ACD Bio # 316111) and Fos (ACD Bio # 316921). Slides were counterstained with DAPI (ACD Bio # 320858) and coverslipped with ProLong Gold Antifade Reagent with DAPI. Three-plex positive (ACD Bio # 320881) and negative (ACD Bio # 320871) controls were used.

3.2.5 c-Fos Immunohistochemistry

Mice were anesthetized with ketamine/acepromazine/xylazine and transcardially perfused with 10 mL PBS followed by 4%-PFA-PBS. Whole brains and spinal cords were dissected and

post-fixed in 4%-PFA-PBS for a minimum of 2h to overnight, and then cryoprotected in 30% sucrose-PBS until tissue sank. 60-µm sections were sliced in a cryostat. Slices were stained free-floating (brain) or fixed to Superfrost Plus slides (spinal cord) as previously described (Nguyen et al., 2022). Briefly, sections were washed with PBS and blocked in 5% normal donkey serum (NDS) in 0.2% Triton-X in PBS (PBS-Tx). Sections were incubated in rabbit c-Fos (Synaptic Systems) primary antibody overnight at room temperature in 5% NDS-PBS-Tx. After washing with PBS-Tx, sections were incubated in donkey anti-rabbit 488 (Invitrogen) secondary antibody for 2 hours at room temperature. Sections were mounted and coverslipped with ProLong Gold with DAPI.

3.2.6 Slice preparation

Oprk1^{cre}*;Rosa*^{tdT} mice were anaesthetized with 5% isoflurane, after reflexes to toe pinch were lost the animals were transcardially perfused with ice-cold glycerol-based slicing solution containing (in mM): 198 glycerol, 2.5 KCl, 10 $MgCl_2$, 0.5 $CaCl_2$, 1.2 NaH_2PO_4, 20 HEPES, 25 $NaHCO_3$ and 0.01 glucose. Brains were then rapidly dissected and 200 µm horizontal sections containing the VTA were made using a vibrating microtome (Campden Instruments 7000 smz). Slices were incubated in a warm (34°C) bath for 30 min in an oxygenated (95% O_2/5% CO_2) holding solution containing (in mM): 92 NaCl, 30 $NaHCO_3$, 20 HEPES, 35 glucose, 2.5 KCl, 1.2 NaH_2PO_4, 2 $MgCl_2$, 2 $CaCl_2$, 5 Na ascorbate, 2 Na pyruvate and 2 Thiourea. The holding solution and slices were then slowly brought to room temperature and left for at least 30 mins before recording.

3.2.7 Patch-clamp electrophysiology

Prior to recording a slice was transferred to a recording chamber that was constantly perfused with oxygenated recording solution containing (in mM): 124 NaCl, 2.5 KCl, 1.2 NaH_2PO_4, 24 $NaHCO_3$, 5 HEPES, 13 glucose, 2 $MgSO_4.7H_20$ and 2 $CaCl_2.2H_2O$. All recordings were made at room temperature. Neurons were visualized using a Zeiss upright microscope and Olympus XM10 camera. tdT neurons were identified using X-cite series LED. Neurons were only recorded if they were deemed to be tdT positive. Borosillicate glass recording electrodes were pulled with a Sutter P-97 horizontal puller to a resistance of 4-6MΩ and filled with a potassium gluconate-based internal solution containing (in mM): 136 K-gluconate, 5 KCl, 0.5 $CaCl_2.2H_2O$, 2 $MgCl_2.6H_2O$, 5 EGTA, 5 MgATP and 5 HEPES, or a Caesium-based internal solution containing (in mM): 130 CsCl, 10 HEPES, 10 EGTA, 1 MgCl2, 2 ATP and 0.3 GTP. Neurobiotin (0.2%) was also included in the internal solution for *post-hoc* cell identification. All data was collected with a Multiclamp 200B amplifier (Molecular Devices) digitized online using and ITC-18 computer interface (Instrutech) and stored using Axograph X software (Molecular devices).

3.2.8 Spontaneous and evoked action potentials

Spontaneous action potentials (APs) were collected in current clamp from resting membrane potential. Spontaneous activity was collected for 1-2 mins and frequency was assessed over the full time of recording. A depolarizing current step protocol was then applied from a membrane voltage of ~-60 mV (1 s duration, 10 pA increments). Frequency of evoked action potentials was assessed during the 1 s current steps and recordings were performed in the absence

of synaptic blockers. Baseline data was collected before DAMGO (1 μM) was bath applied and the protocol (or spontaneous activity recording) repeated.

3.2.9 Voltage-clamp recordings

Spontaneous EPSCs and IPSCs were collected in a continuous voltage-clamp recording. A 5 mV pulse was delivered every 30 s to monitor input and series resistance, if either deviated more that 15% the recording was abandoned. After 3 min baseline activity was collected DAMGO (1 μM) or U69593 (1 μM) was bath applied. In inhibitory recordings CNQX (10 μM) was applied for the duration of the recording to prevent analysis of EPSCs.

3.2.10 Post-hoc immunostaining

Following recording slices were immediately fixed in 4% paraformaldehyde overnight. Slices were washed in PBS and incubated at 4°C in rabbit anti tyrosine hydroxylase (1:1000). Slices were washed again and incubated at room temperature in donkey anti rabbit 488 (1:50) and streptavidin alexafluor 647 (1:50). Slices were mounted on glass slides and the whole slice was imaged to confirm recording location in the VTA.

3.2.11 Imaging

Sections were imaged at full tissue thickness using an upright epifluorescent microscope (Leica DMi8 Epifluorescent Microscope with 2.5x, 5x, 10x, 20x, or 40x objectives). All analysis was completed off-line using FIJI software (Image J, NIH), Python, and R. For electrophysiology,

presence of neurobiotin-containing cell bodies within the bounds of the VTA were identified based on Paxinos and Franklin's mouse brain atlas (Paxinos & Franklin, 2012); any patched cell found to reside outside of the VTA were not included in the analysis.

3.2.12 RNAscope Quantification

To quantify morphine-induced Fos expression, Oprk1+ and Fos+ cells were manually counted by an experimenter independent of the image acquisition. For manual counting, only cells with puncta forming a ring around a visible DAPI nucleus were included.

3.2.13 Statistical Analysis

All statistical analyses were analyzed with GraphPad Prism 9.0. Values are represented as mean ± SEM. Statistical significance was assessed using an unpaired t-test, paired t-test, two-way ANOVA, or two-way repeated measures ANOVA followed by Holm-Sidak post-hoc test, as described in the figure legends; parametric tests were justified by the normal distribution of reported data sets. Significance was indicated by $p < 0.05$. The n for each experiment is described in the figure legends; for morphine-induced fos studies, three images were averaged per animal. Sample sizes were selected based on previously published histological and RNAscope experiments (Chiang et al., 2020; Nguyen et al., 2022).

3.3 Results

3.3.1 Chronic opioids reduce morphine-induced c-Fos expression in VTA^{KOR} neurons

Given the diversity in neurotransmitter expression in VTA^{KOR} neurons as well as the unique effects of chronic opioids on dynorphin tone originating from different brain regions found in Chapter 2, we next sought to determine the effects of chronic opioids on the neural activity of VTA^{KOR} neurons. To address this, we quantified c-Fos expression in VTA^{KOR} neurons in opioid naïve and opioid-dependent mice after administration of morphine 10 mg/kg (Figure 7A). We found that while morphine 10 mg/kg was sufficient to significantly increase c-Fos expression in VTA^{KOR} neurons in opioid-naïve mice, there was no significant effect of this dose of morphine in opioid-dependent mice (Figure 7B-C). Interestingly, while there existed a main effect of chronic morphine dependence on c-Fos expression (Table 1), morphine 10 mg/kg was not sufficient to significantly increase c-Fos expression in all neurons in the opioid-naïve or opioid-dependent groups (Figure 7D). Thus, chronic exposure to opioids decreases acute opioid-induced c-Fos expression in the VTA, and in VTA^{KOR} neurons specifically.

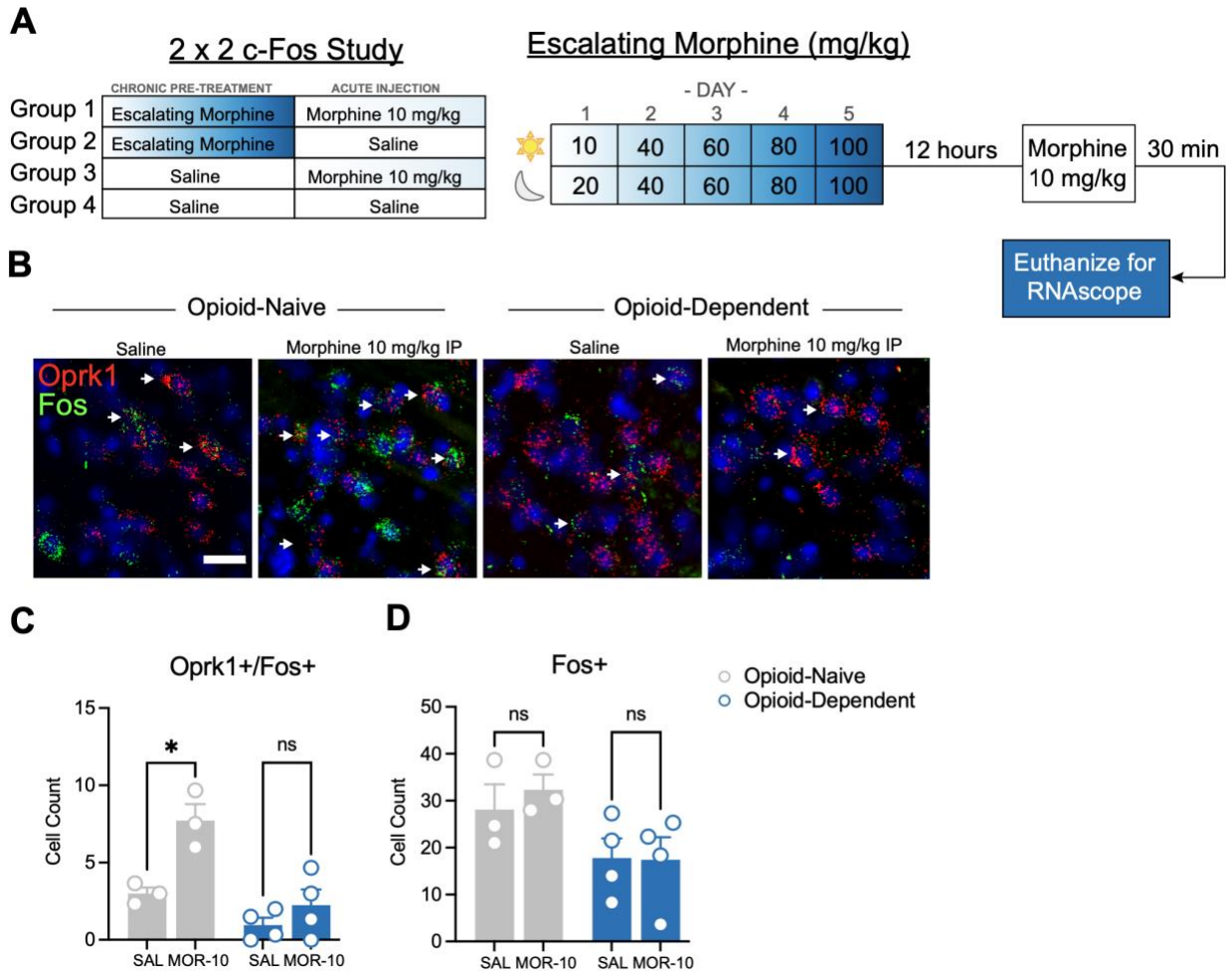

Figure 7 Chronic morphine decreases acute morphine-induced c-Fos expression in VTA^{KOR} neurons.

(A) Experimental design. Left: C57BL/6 mice were split into four groups in a 2x2 study based on chronic pre-treatment and acute injection. Right: mice received escalating doses of morphine or saline IP for 5 days. 12 hours later, mice received a smaller dose of morphine (10 mg/kg) IP or saline, and were euthanized 30 minutes later for RNAscope. (B) Example RNAscope FISH images from each group for Oprk1 (red) and Fos (green) in the VTA. Scale bar = 50 µm. (C) Counts of Oprk1+/Fos+ cells in the VTA in opioid-naïve (gray) and opioid-dependent (blue) mice. Data are mean ± SEM and each dot represents 2-3 averaged images from each animal (n = 3-4 mice per group). *indicates significantly different (2-way ANOVA with Sidak post-hoc test, $p<0.05$). (D) Counts of Fos+ cells in the VTA in opioid-naïve (gray) and opioid-dependent (blue) mice. Data are mean ± SEM and each dot represents 2-3 averaged images from each animal (n = 3-4 mice per group).

To investigate further whether this effect is specific to VTA^{KOR} neurons, we characterized the localization of KOR neurons and morphine-induced c-Fos expression within the VTA in more detail (Figure 8). We quantified Oprk1 fluorescence in a representative subset of RNAscope FISH images within the five major subregions of the VTA: the parabrachial pigmented nucleus (PBP), the paranigral nucleus (PN), the interpeduncular nucleus (IPn), the caudal linear nucleus of the raphe (CLi), and the interfascicular nucleus (IF) (Figure 8A-B). We found the majority of Oprk1 fluorescence was localized to the PBP (54.5% ± 2.7%) and the PN (20.6% ± 1.2%) while the IPn, CLi, and IF contained smaller proportions of Oprk1 fluorescence (14.5 ± 1.2%, 6.1% ± 0.5%, and 4.3% ± 0.9%, respectively) (Figure 8C). We also quantified c-Fos protein immunoreactivity in all VTA neurons induced by morphine 10 mg/kg in opioid-naïve and opioid-dependent mice (Figure 8D). We observed the most pronounced effect size of morphine 10 mg/kg within the PBP and PN, where the vast majority of VTA^{KOR} neurons reside (Figure 8E-F). Thus, the effects of chronic and acute morphine on c-Fos expression in the VTA is specific to VTA^{KOR} neurons.

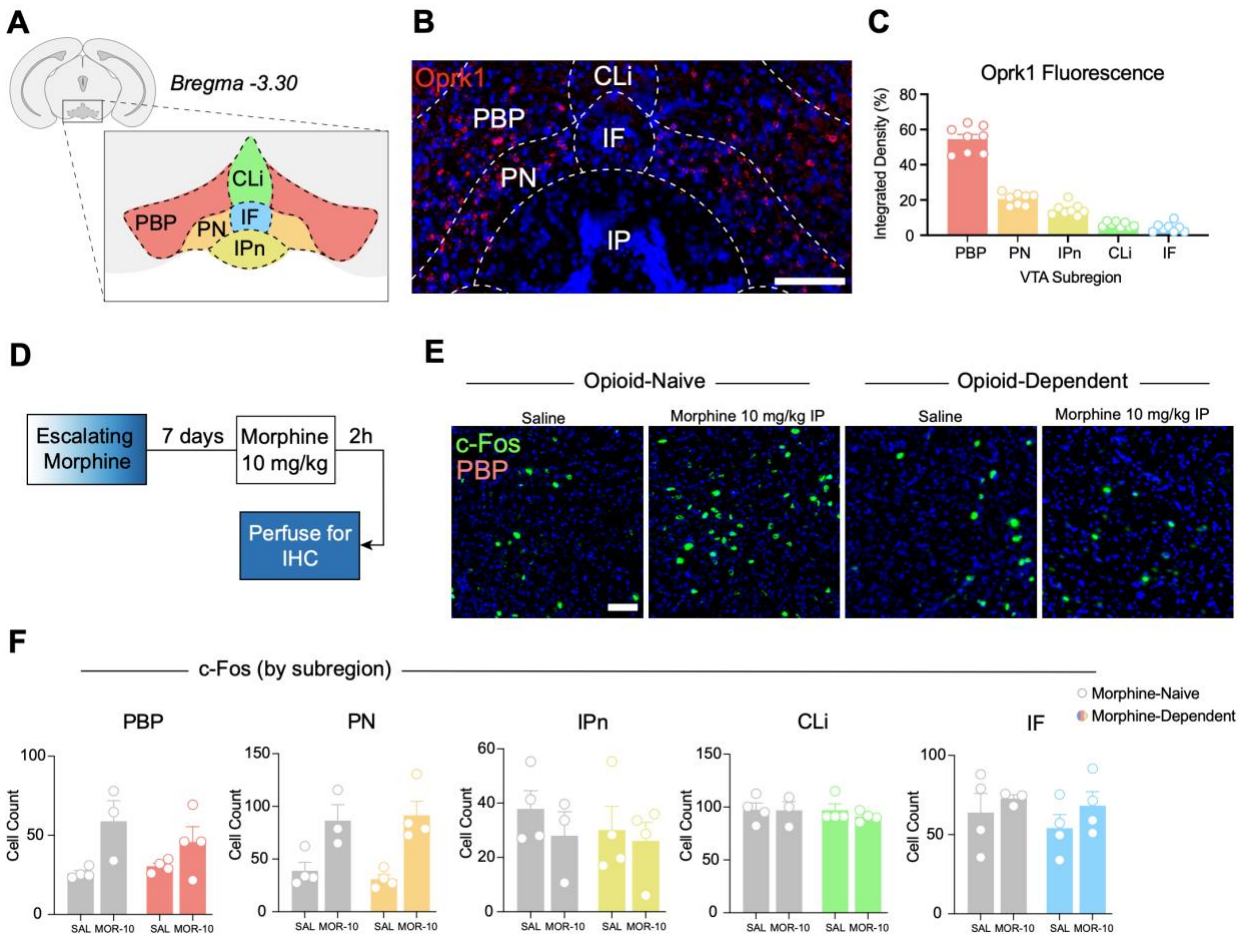

Figure 8 The effects of morphine on c-Fos expression in the VTA are specific to VTA^{KOR} neurons.

(A) Illustration of the subregions of the VTA: the parabrachial pigmented nucleus (PBP), the paranigral nucleus (PN), the interpeduncular nucleus (IPn), the caudal linear nucleus of the raphe (CLi), and the interfascicular nucleus (IF). (B) Representative RNAscope image of Oprk1 (red) in the VTA, with subregions denoted. (C) Integrated density of Oprk1 fluorescence. Dots represent one image per mouse (n = 8 mice). (D) Experimental design for morphine-induced c-Fos IHC. (E) Example images of c-Fos (green) in the PBP region of the VTA, from opioid-naïve and opioid-dependent mice. (F) Counts of c-Fos immunoreactive puncta by VTA subregion. Data are represented as mean ± SEM.

3.3.2 Opioid withdrawal augments the MOR-evoked excitatory and inhibitory drive onto VTA^{KOR} neurons

To dissect the physiological mechanisms underlying the decrease in neuronal activity induced by chronic morphine as described above, we used *ex vivo* patch clamp recordings from mice in opioid withdrawal (Figure 9). In order to selectively record from VTA^{KOR} neurons, we bred a KOR reporter mouse line (*Oprk1^{cre};Rosa^{tdT}*) which expresses tdTomato in Oprk1-expressing neurons and is highly sensitive for VTA^{KOR} neurons as measured by the colocalization of Oprk1 and tdTomato genes in VTA slices (Figure 9A). We induced morphine withdrawal through escalating doses of IP morphine for 6 days, followed by a single injection of naloxone, and mice were euthanized for recordings 30 minutes after naloxone administration (Figure 9B). Horizontal slices of the VTA were taken and cells with robust tdTomato fluorescence were recorded (Figure 9C). We found that morphine withdrawal did not significantly impact the spontaneous action potential frequency in aCSF or impact the change in frequency in response to the bath application of the MOR agonist DAMGO (Figure 9D-E). In addition, action potential frequency at rheobase, calculated by injecting a ramp of current to determine the minimum amount of current required to generate an action potential, did not change in morphine withdrawal mice in the presence of aCSF or DAMGO (Figure 9F-G). Thus, morphine withdrawal is not changing the intrinsic firing properties of VTA^{KOR} neurons.

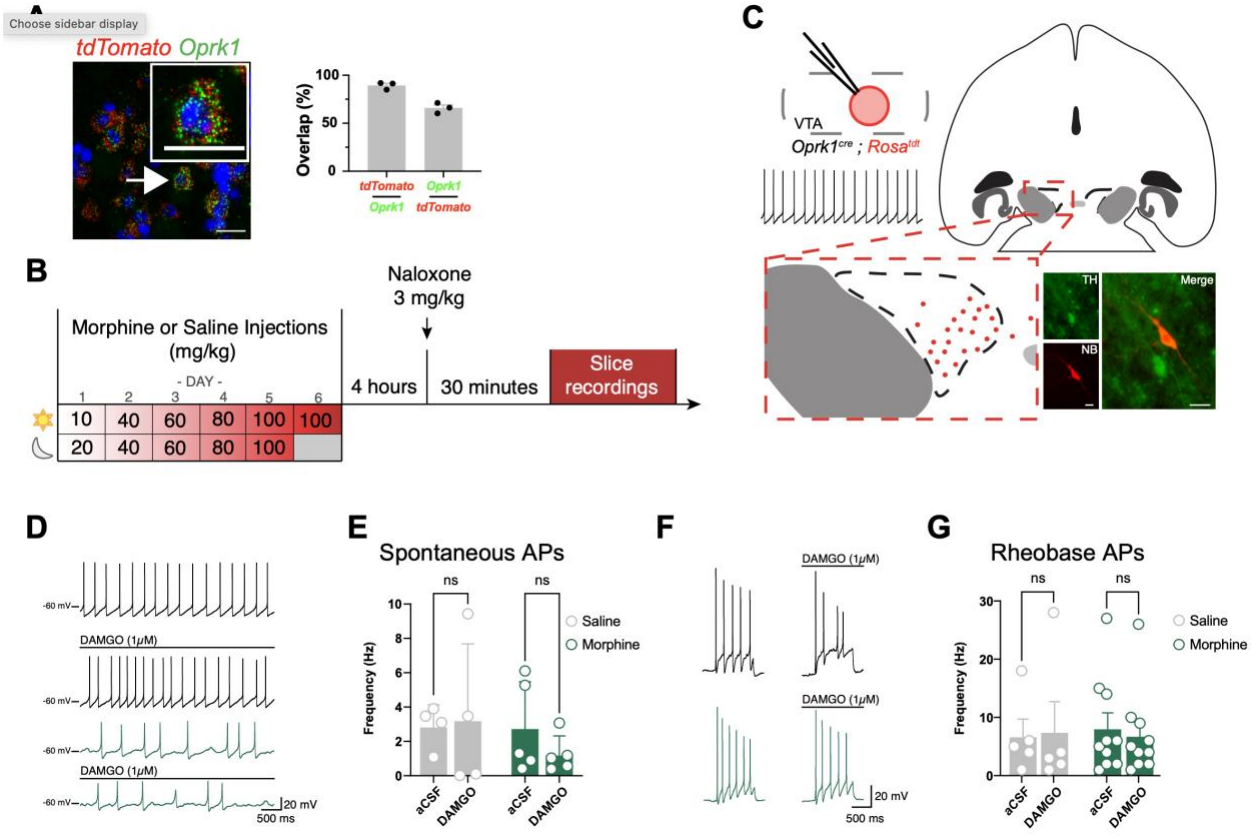

Figure 9 Opioid withdrawal does not alter action potential frequency of VTA^{KOR} neurons.

(A) Validation of the *Oprk1^{cre};Rosa^{tdT}* mouse line. Left: RNAscope FISH for tdTomato (red) and Oprk1 (green). Right: quantification of overlap between tdTomato and Oprk1. Scale bar = 25 µm. (B) Timeline of morphine paradigm before slice recordings. (C) Schematic of slice recording set up. Top left: whole-cell patch clamp recording were made from tdT neurons in the VTA, example spontaneous action potentials shown below. Top right: horizontal brain sections were taken and recording were made from the VTA. Bottom left: inset shows expanded view of the VTA in a horizontal section; the VTA is highlighted by the dashed line, red circles are locations of recorded and recovered neurons in the VTA. Bottom right: tdT neuron that was recovered by neurobiotin labelling following patch-clamp recording. Green = tyrosine hydroxylase (TH) immunostaining, red = neurobiotin (NB). Scale bar = 15 µm. (D) Example traces of spontaneous action potentials in current clamp recordings with and without DAMGO. Black traces are from saline animals, green traces are from morphine animals. (E) Quantification of spontaneous action potential (AP) frequency. Grey bars are saline animals, green bars are morphine animals. Data points are individual cells (n = 4-5 cells per group), and group data is represented as mean ± SEM. (F) Representative traces from the rheobase step from a depolarizing protocol with and without DAMGO. Black traces

are from saline animals, green traces are from morphine animals. (G) Quantification of AP frequency at rheobase. Grey bars are saline animals, green bars are morphine animals. Data points are individual cells (n = 5-10 cells per group), and group data is represented as mean ± SEM.

To determine whether opioid withdrawal altered the excitatory or inhibitory input onto VTA^{KOR} neurons, we measured the frequency of excitatory and inhibitory postsynaptic currents (EPSCs and IPSCs) (Figure 10). We found that EPSC frequency was similar between opioid-naïve and opioid withdrawal mice in the presence of aCSF. However, bath application of DAMGO significantly decreased EPSC frequency in opioid withdrawal mice without changing EPSC frequency in opioid-naïve mice (Figure 10A-B). When measuring IPSCs, we found that in the presence of aCSF, no difference in IPSC frequency was identified between opioid-naïve mice and opioid withdrawal mice. However, bath application of DAMGO significantly decreased IPSC frequency in morphine withdrawal mice, but did not decrease IPSC frequency in opioid-naïve mice (Figure 10C-D). By contrast, bath application of the KOR agonist U69,593 did not significantly change IPSC frequency of either group (Figure 10E-F). While investigating potential mechanisms for these effects, we noted that of all the cells patched, fewer cells from mice in morphine withdrawal survived the entirety of the recording paradigm, suggestive of poorer health of the cells (Figure 10G). Furthermore, we performed a more in-depth analysis of EPSC and IPSC properties, and investigated sex as a biological variable and found no notable differences between males and females (Appendix A Figure 1). Taken together, these experiments support that opioid withdrawal augments MOR-mediated reductions in excitatory and inhibitory drive onto VTA^{KOR} neurons.

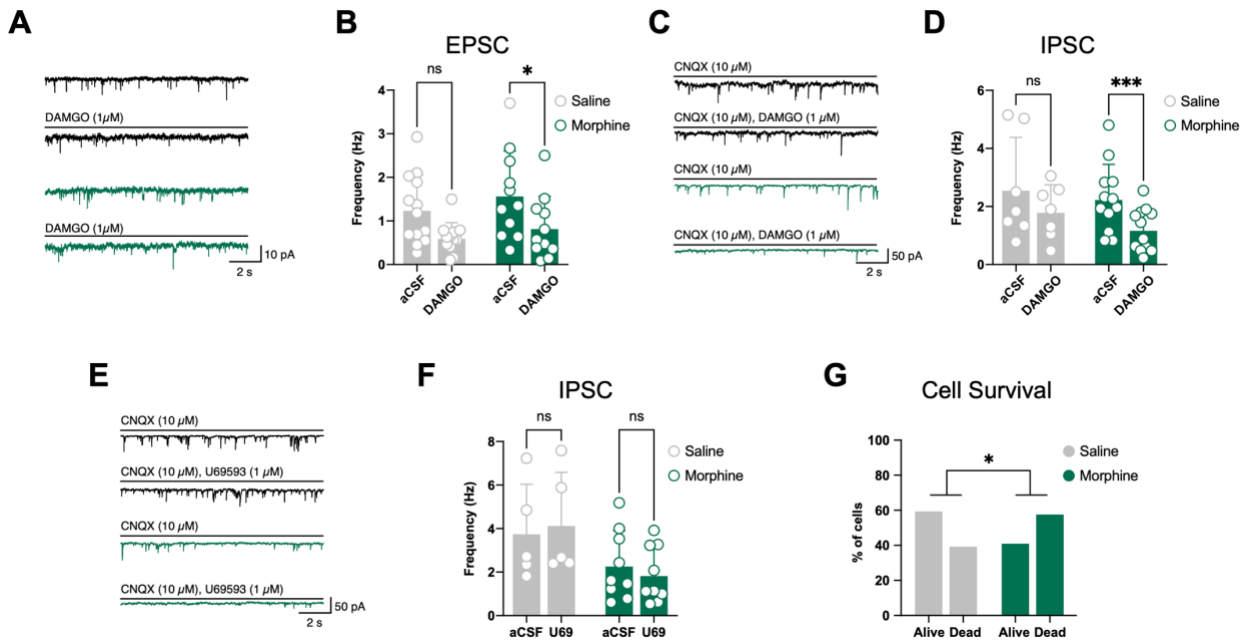

Figure 10 Opioid withdrawal augments MOR-mediated decreases in EPSCs and IPSCs in VTA^{KOR} neurons.

(A) Example traces of spontaneous excitatory post synaptic currents (EPSCs) with and without DAMGO. Black traces are from saline animals, green traces are from morphine animals. (B) Quantification of EPSC frequency. Grey bars are saline animals, green bars are morphine animals. Data points are individual cells (n = 11-13 cells per group), and group data is represented as mean ± SEM. *indicates significantly different (2-way RM ANOVA with Holm-Sidak post-hoc test, $p<0.05$ (C) Example traces of spontaneous inhibitory post synaptic currents (IPSCs) with and without DAMGO. (D) Quantification of IPSC frequency. Grey bars are saline animals, green bars are morphine animals. Data points are individual cells (n = 7-12 cells per group), and group data is represented as mean ± SEM. ***indicates significantly different (2-way RM ANOVA with Holm-Sidak post-hoc test, $p<0.001$. (E) Example traces of spontaneous inhibitory post synaptic currents (IPSCs) with and without U69,593. (F) Quantification of IPSC frequency. Grey bars are saline animals, green bars are morphine animals. Data points are individual cells (n = 5-9 cells per group), and group data is represented as mean ± SEM. (G) Graphed data illustrating cell health in saline and morphine animals. Grey bars are percent of cells from saline animals that survived (alive) or did not survive (dead) the full recording paradigm. Green bars are the same but for morphine animals. *Indicates significantly different (Chi-squared test, $p<0.05$).

Table 2 Summary of F Statistics for ANOVAs in Chapter 3

Sub-Figure	Test	Effect	F (DFn, DFd)	p value	Significant?
7C	2-way ANOVA with Sidak correction	Interaction	F (1, 10) = 4.448	P=0.0411	Yes
		Acute Drug	F (1, 10) = 13.67	P=0.0041	Yes
		Morphine Dependence	F (1, 10) = 21.34	P=0.0010	Yes
7D	2-way ANOVA with Sidak correction	Interaction	F (1, 10) = 0.2509	P=0.6273	No
		Acute Drug	F (1, 10) = 0.1757	P=0.6840	No
		Morphine Dependence	F (1, 10) = 7.559	P=0.0205	Yes
9E	Mixed effects analysis with Sidak correction	Drug	F (1, 8) = 0.2254	P=0.6476	No
		Treatment	F (1, 6) = 0.7422	P=0.422	No
		Drug x Treatment	F (1, 6) = 0.5989	P=0.4684	No
9G	2-way RM ANOVA with Sidak correction	Drug x Treatment	F (1, 20) = 0.05509	P=0.8168	No
		Drug	F (1, 20) = 0.3669	P=0.5515	No
		Treatment	F (1, 20) = 0.2037	P=0.6566	No
10B	Mixed effects analysis with Sidak correction	Drug	F (1, 44) = 10.29	P=0.0025	Yes
		Treatment	F (1, 44) = 1.636	P=0.2076	No
		Drug x Treatment	F (1, 44) = 0.06126	P=0.8057	No
10D	2-way RM ANOVA with Sidak correction	Drug x Treatment	F (1, 17) = 0.5896	P=0.4531	No
		Drug	F (1, 17) = 21.71	P=0.0002	Yes
		Treatment	F (1, 17) = 0.8238	P=0.3768	No
10F	2-way RM ANOVA with Sidak correction	Drug	F (1, 16) = 0.01517	P=0.9035	No
		Treatment	F (1, 8) = 18.86	P=0.0025	Yes
		Drug x Treatment	F (1, 8) = 0.4827	P=0.5069	No

3.4 Discussion

In this chapter we provide molecular and electrophysiological evidence that chronic opioids depress VTA^{KOR} neural activity. We used RNAscope FISH to quantify c-Fos, a marker of neuronal activity, in VTA^{KOR} neurons, and designed a 2x2 experiment determining how a chronic escalating pre-exposure to opioids would impact c-Fos induced by acute morphine. We showed that mice rendered dependent to opioids had a decrease in acute morphine-induced c-Fos

expression in VTA^{KOR} neurons, indicating an overall inhibitory effect of chronic opioids on VTA^{KOR} neurons. Furthermore, we bred genetically engineered mice expressing Cre recombinase under the *Oprk1* promoter to mice expressing the fluorescent reporter tdTomato in the presence of Cre, to generate the *Oprk1*$^{cre;tdTomato}$ mouse. This empowered us to selectively target VTA^{KOR} neurons *ex vivo* and characterize their firing properties through patch clamp electrophysiology in VTA slices. We found that while opioid withdrawal does not significantly alter the spontaneous firing properties of VTA^{KOR} neurons, it does augment MOR-mediated inhibition of EPSCs and IPSCs onto VTA^{KOR} neurons. Together, these experiments revealed complex effects of chronic opioids on the molecular and electrophysiological properties of VTA^{KOR} neurons and their inputs, and uncovered novel mechanisms by which opioids impact this subpopulation of neurons.

A novel finding through our molecular experiments was that morphine-induced c-Fos expression in the VTA is specific to VTA^{KOR} neurons. We confirmed by this by quantifying c-Fos expression in neurons globally and observing no effect, and correlating the effects of morphine on c-Fos expression with subregions of the VTA in which KOR expression is localized. This is consistent with our RNAscope FISH data indicating VTA^{KOR} neurons are largely dopaminergic (i.e. principal neurons); however, these experiments do not address whether morphine-induced c-Fos expression manifests in any specific genetic subpopulation of VTA^{KOR} neurons. Our work is also consistent with at least one prior *in vivo* electrophysiology study in which morphine-naïve rats show a morphine-induced increase in dopamine neuron activity, while morphine-dependent rats did not show this effect (Georges et al., 2006). Together, these results support the kappa overdrive model, in which chronic opioids are paradoxically depressing VTA neural activity.

An additional novel finding was that chronic opioids enhance MOR-mediated inhibition of EPSCs and IPSCs. While our electrophysiology data does not directly support the kappa overdrive

model, this finding expands our understanding of how chronic opioids could be impacting signaling pathways in the midbrain. Interestingly, opioid withdrawal did not manifest in differences in the spontaneous firing properties of VTA^{KOR} neurons. Prior studies have not been consistent in this measure; some prior work has indicated opioid withdrawal chronically decreases dopamine neuron activity (Diana et al., 1995) while a contradictory study shows an increase in a basal dopamine neuron firing rate in opioid withdrawal (Georges et al., 2006). There are a few potential reasons for this inconsistency. Firstly, it is possible that chronic opioids impact solely a specific subpopulation of VTA^{KOR} neurons, such as a specific projection or neurochemical identity. Furthermore, we incidentally showed that VTA^{KOR} cells from mice in withdrawal were significantly less likely to survive than VTA^{KOR} cells. Therefore, the diverse properties we observed from the cells which survived could represent, at least in part, a compensatory mechanism in response to chronic morphine-exposed cells undergoing cell death or exhibiting excitotoxity. This hypothesis is supported by a recent transcriptomics paper identified that markers of DNA damage, neuroinflammation and excitotoxicity are upregulated in the context of opioid use disorder (Phan et al., 2023). Future studies will need to investigate these mechanisms more in-depth.

The effects of acute opioids on VTA dopamine neurons are well-characterized; acute morphine administration robustly enhances VTA dopamine release in the NAc (Di Chiara & Imperato, 1988) and increases VTA dopamine neuron firing (Gysling & Wang, 1983) through inhibition of GABA interneurons (Johnson & North, 1992). However, the effects of chronic opioids on VTA neurons are lesser understood, and no study to our knowledge has investigated the effects of opioid withdrawal on VTA^{KOR} neurons. Therefore, our results, both positive and

negative, are highly novel and advance our understanding of opioid withdrawal mechanisms in the midbrain.

Importantly, these studies do not directly address how these molecular or electrophysiological changes impact dopamine release downstream. Follow-up studies will be necessary to determine how the effects of chronic opioids on c-Fos expression and MOR-evoked reductions in EPSCs and IPSCs onto VTA^{KOR} neurons directly translates to differences in downstream reward signaling. Furthermore, the electrophysiology experiments described here are limited in that they do not distinguish between dopaminergic, glutamatergic, and/or GABAergic neurons via *post hoc* staining, or different projections of VTA^{KOR} neurons through retrograde labeling. Given our RNAscope FISH has uncovered the heterogeneity of this population, follow-up studies will be necessary to delve deeper into projection-specific and neurotransmitter-specific mechanisms, and to adequately sample from and evaluate all subpopulations identified in all experimental groups.

4.0 Chapter 4: Activation of VTA→PAG^{KOR} Neurons Attenuates Opioid Withdrawal-Associated Gastrointestinal Distress

4.1 Introduction

Our work has demonstrated that opioid withdrawal is associated with an upregulation in midbrain KOR and dynorphin expression and with inhibited VTA^{KOR} neuronal activity. Previous studies have also shown that KOR antagonism and resultant disinhibition of VTA neurons prevents or attenuate aversion and associated reductions in dopamine release (Liu et al., 2019; Robble et al., 2020). Buprenorphine, a MOR partial agonist with KOR antagonist activity, is an effective pharmacological therapy for OUD (Haight et al., 2019; Lee et al., 2018). However, preclinical pharmacological studies show KOR antagonism has different effects on opioid withdrawal behaviors, with some studies showing KOR inhibition attenuates withdrawal (Lutz et al., 2014; Schlosburg et al., 2013; Zan et al., 2015) while others show KOR inhibition exacerbates opioid withdrawal behaviors (Le Guen et al., 2003; Maldonado, Negus, et al., 1992; R Spanagel et al., 1994). Pharmacological studies such as these are limited in their ability to distinguish between the effects of KOR agonism or antagonism in different subpopulations of VTA^{KOR} neurons. This chapter describes experiments in which VTA^{KOR} neurons are genetically targeted and activated *in vivo* to identify distinct neural projections of VTA^{KOR} neurons as well as their functional role in opioid withdrawal behaviors. Given the complexity of KOR and dynorphin circuitry as well as the extensive range of projection targets of VTA neurons (Breton et al., 2019), we intend to identify a novel, noncanonical circuit critical for opioid withdrawal behaviors.

4.2 Methods

4.2.1 Subjects

Oprk1^{cre} mice (Cai et al., 2016) were maintained on a C57BL/6 background. Mice were group-housed in a temperature and humidity-controlled room maintained on a 12h/12h light-dark cycle (lights on at 0700). Animals were given *ad libitum* access to pelleted chow and water. All protocols and procedures were approved by the Institutional Care and Use Committee of the University of Pittsburgh.

4.2.2 Viruses

AAV2-hSyn-DIO-mCherry (Addgene viral prep # 50459-AAV2) and AAV2-hSyn-DIO-hM3D(Gq)-mCherry (Addgene viral prep # 44361-AAV2) were gifts from Bryan Roth (Krashes et al., 2011). AAVrg-DIO-FlpO (Stanford Gene Vector and Virus Core), AAV8-hSyn-fDIO-hM3D(Gq)-mCherry, (Stanford Gene Vector and Virus Core), and AAV8-hSyn-fDIO-hM4D(Gi)-mCherry (Stanford Gene Vector and Virus Core) were gifts from Karl Diesseroth.

4.2.3 Drugs

Clozapine-*N*-oxide (CNO; 0.5 mg/ml Tocris #4936), morphine sulfate (4 mg/ml; Covetrus), and naloxone (0.3 mg/ml; Sigma Aldrich #PHR1802) were dissolved in sterile saline (0.9% NaCl) and administered intraperitoneally.

4.2.4 Stereotaxic Surgery

Mice were anesthetized with 2% isoflurane and fixed in a stereotaxic frame. Ophthalmic ointment was applied to the eyes and the scalp was shaved and disinfected with betadine and 70% ethanol. The cranium was exposed with a midline incision and sutures were unveiled with 3% hydrogen peroxide. Bregma and lambda suture lines were leveled to within 100 μm. A small burr hole was drilled into the skull and a custom-made 33-gauge metal needle was lowered slowly into the injection site. 250 nl of virus was injected bilaterally into the ventral tegmental area (VTA: AP -3.30 mm, ML ±0.35 mm, DV -4.80 mm from top of skull) or ventrolateral periaqueductal gray (vlPAG; AP -4.70 mm, ML ±0.74 mm, DV -3.00 mm from top of skull) using a Hamilton syringe. The needle was kept in place for 15 minutes to allow for diffusion of the virus and then slowly withdrawn. The incision was closed with VetBond glue and animals were given an intraperitoneal injection of ketoprofen (5 mg/kg) and buprenorphine (0.1 mg/kg) for analgesia. Animals were given 4 weeks to recover before beginning behavioral experiments.

4.2.5 Precipitation of Morphine Withdrawal and Spontaneous Behaviors

Mice were given twice daily IP injections of morphine (Covetrus) at escalating doses for 5 days and a single dose on day 6 (day 1 AM, 10 mg/kg; day 1 PM, 20 mg/kg; day 2 AM and PM, 40 mg/kg; day 3 AM and PM, 60 mg/kg; day 4 AM and PM, 80 mg/kg; day 5 AM and PM, 100 mg/kg; day 6 AM, 100 mg/kg) in order to induce morphine dependence. Four hours after the last morphine injection, mice received injections of naloxone 3 mg/kg IP (Sigma Aldrich Cat# PHR1802) and were immediately placed in plexiglass containers. Withdrawal-associated spontaneous behaviors such as jumping, shakes and tremors were recorded for 30 minutes. Body

weight loss was calculated by subtracting body weight before and 30 minutes after naloxone injection. Fecal matter and urine were collected on absorbent pads during the duration of the 30-minute behavioral experiment; defecation and urination were calculated by subtracting the weight of the absorbent pad before (W0), 30 minutes after naloxone injection (W30), and 24 hours after the conclusion of the behavioral experiment (W24):

$$\text{Defecation} = W24 - W0; \quad \text{Urination} = W30 - W24.$$

4.2.6 Open Field

Mice were habituated to the testing room for 1 hour. 30 minutes after injecting CNO 5 mg/kg IP, mice were then placed in an open field chamber (27.3 cm x 27.3 cm, Omnitech Electronics, Inc.) for 60 minutes. Mouse locomotive behaviors including distance traveled and margin time were recorded and summarized by VersaMax software.

4.2.7 Light-Dark Assay

The light-dark assay was performed as previously described as a measure of anxiety-like behavior (Bourin & Hascoët, 2003). Briefly, mice were habituated to the testing room for 1 hour. 30 minutes after injecting CNO 5 mg/kg IP, mice were placed in an open field activity chamber (27.3 cm x 27.3 cm, Omnitech Electronics, Inc.) containing a black insert which splits the field into a light and dark chamber. The activity of the mice, specifically time spent in the dark chamber, was recorded automatically by the VersaMax software.

4.2.8 Tail Suspension Test

The mouse tail suspension test was performed as described elsewhere as a measure of behavioral despair (Can et al., 2012). Briefly, mice were habituated to the testing room for 1 hour. A "climbstopper" (4 cm long, 1.6 cm OD, 1.3 cm ID, polyethylene tube) was placed at the base of the tail to inhibit the mice from climbing up their own tails. The tail of the mice was fixed to a 6-inch piece of 1-inch wide laboratory tape. The tape was placed on a bar suspended horizontally 2 feet above the table between two ring stands. The mobility for all 6 minutes was quantified manually from video footage, and immobility time was calculated by subtracting the mobility time (in seconds) from 360.

4.2.9 Conditioned Place Aversion

In order to determine the effects of cell type-specific neural modulation on the aversive nature of naloxone precipitated morphine withdrawal, we performed a conditioned place aversion (CPA) assay. CPA trains subjects to associate a stimulus with certain visual and tactile cues, and is a highly sensitive measure of the aversiveness of opioid withdrawal in rodents (Azar et al., 2003). Briefly, mice were acclimated to the testing room prior to testing. Experiments were conducted in a 3-chamber box consisting of a center chamber, and a left and right chamber which differ in both tactile and visual cues. The left chamber was decorated with vertically striped walls and a rough floor, while the right chamber was decorated with horizontal stripes and a smooth floor. The center chamber was decorated with white walls and a bright light to discourage exploration of the center chamber. CPA boxes were custom-built and generously provided by the laboratory of Dr. Bradley Taylor (Cooper et al., 2022). *Habituation (Day 1):* Morphine-dependent

mice were placed into the center chamber and allowed to explore all 3 chambers of the CPA box for 30 minutes. *Preconditioning (Day 2):* Mice were placed into the center chamber and allowed to explore all chambers for 30 minutes. Movement of the mice were tracked automatically with beam breaks. Time spent in each chamber was quantified for the first 15 minutes; any mice with a baseline preference for either chamber (>200 seconds) was excluded from final analyses. *Conditioning (Days 3-5):* Mice were pre-treated with CNO (5 mg/kg IP) 30 minutes prior to conditioning. The mouse then received naloxone (3 mg/kg IP) or no injection and was immediately confined to the paired or unpaired chamber, respectively, for 30 minutes. *Postconditioning (Day 6):* Mice were placed in the center chamber and allowed to explore all 3 chambers for 30 minutes. Time spent in each chamber was quantified for the first 15 minutes. A preference score was calculated by subtracting the time spent in the paired chamber on the preconditioning day from the time spent in the paired chamber on the postconditioning day ("pre minus post").

4.2.10 Immunohistochemistry

Mice were anesthetized with ketamine/acepromazine/xylazine and transcardially perfused with 10 mL PBS followed by 4%-PFA-PBS. Whole brains and spinal cords were dissected and post-fixed in 4%-PFA-PBS for a minimum of 2h to overnight, and then cryoprotected in 30% sucrose-PBS until tissue sank. 60-μm sections were sliced in a cryostat. Slices were stained free-floating (brain) or fixed to Superfrost Plus slides (spinal cord) as previously described (Nguyen et al., 2022). Briefly, sections were washed with PBS and blocked in 5% normal donkey serum (NDS) in 0.2% Triton-X in PBS (PBS-Tx). Sections were incubated in primary antibodies overnight at room temperature in 5% NDS-PBS-Tx. Primary antibodies used were rabbit anti-RFP (Rockland), chicken anti-RFP (Rockland), rabbit anti-tyrosine hydroxylase (Millipore), mouse

anti-GAD67 (EMD Millipore), and guinea pig anti-VGlut2 (EMD Millipore). After washing with PBS-Tx, sections were incubated in secondary antibody for 2 hours at room temperature. Secondaries used include donkey anti-rabbit 488 (Invitrogen), donkey anti-rabbit 594 (Invitrogen), donkey anti-chicken 555 (Invitrogen), donkey anti-guinea pig 647 (Invitrogen), and donkey anti-mouse 750 (Abcam). Sections were mounted and coverslipped with ProLong Gold with DAPI.

4.2.11 Imaging and Quantification

Sections were imaged at full tissue thickness using an upright epifluorescent microscope (Olympus BX53 with UPlanSApo 4x, 10x, or 20x objectives, Leica DM6B Epifluorescent Microscope with 2.5x, 10x, 20x, or 40x objectives or Leica DMi8 Epifluorescent Microscope with 2.5x, 5x, 10x, 20x, or 40x objectives). All analysis was completed off-line using FIJI software (Image J, NIH). For anterograde tracing, presence of mCherry-immunoreactive fibers were manually identified based on Paxinos and Franklin's mouse brain atlas (Paxinos & Franklin, 2012).

4.2.12 Quantification and Statistical Analysis

All statistical analyses were analyzed with GraphPad Prism 9.0. Values are represented as mean ± SEM. Statistical significance was assessed using a paired t-test or two-way repeated-measures ANOVA followed by Holm-Sidak post-hoc test; parametric tests were justified by the normal distribution of reported data sets. Significance was indicated by $p < 0.05$. The n for each experiment is described in the figure legends. Sample sizes were calculated to achieve a power of

0.8; expected effect sizes were determined through pilot experiments and previously published behavioral experiments.

4.3 Results

4.3.1 Chemogenetic activation of VTA^{KOR} neurons attenuates opioid withdrawal

Given that chronic opioids have complex effects on the neural activity of VTA^{KOR} neurons and their inputs, we questioned whether these activity changes are responsible for the aversive, dysautonomic, and negative affective symptoms associated with cessation of opioids. To further address this issue, we tested whether activating VTA^{KOR} neurons would diminish the behavioral responses to naloxone-precipitated opioid withdrawal. To this end, an AAV encoding an excitatory designer receptor exclusively activated by designer drug (DREADD), hM3D(Gq), as well as an mCherry reporter, was stereotaxically delivered into the VTA of *Oprk1^{cre}* mice (Figure 11A). Behaviors were tested in the presence of the DREADD ligand CNO (5 mg/kg IP) both in the opioid-naïve condition and for 30 minutes after eliciting opioid withdrawal (Figure 11B). In opioid-naïve mice, withdrawal-associated behaviors such as jumping, shakes and tremors, body weight loss, defecation, and urination were minimal, and CNO had no effect on these behaviors. However, rapidly eliciting opioid withdrawal with naloxone (3 mg/kg IP) was associated with significant jumping (Figure 11C) and shakes and tremors (Figure 11D), which were all significantly reduced when VTA^{KOR} neurons were chemogenetically activated by CNO. Interestingly, opioid withdrawal-associated body weight loss (Figure 11E), defecation (Figure 11F) and urination (Figure 11G) were also significantly reduced when VTA^{KOR} neurons were

chemogenetically activated by CNO. Thus, depressed activity of VTA^{KOR} neurons is necessary for multiple opioid withdrawal-associated behaviors, and central midbrain circuits are mediating dysautonomic withdrawal symptoms such as body weight loss, diarrhea and micturition.

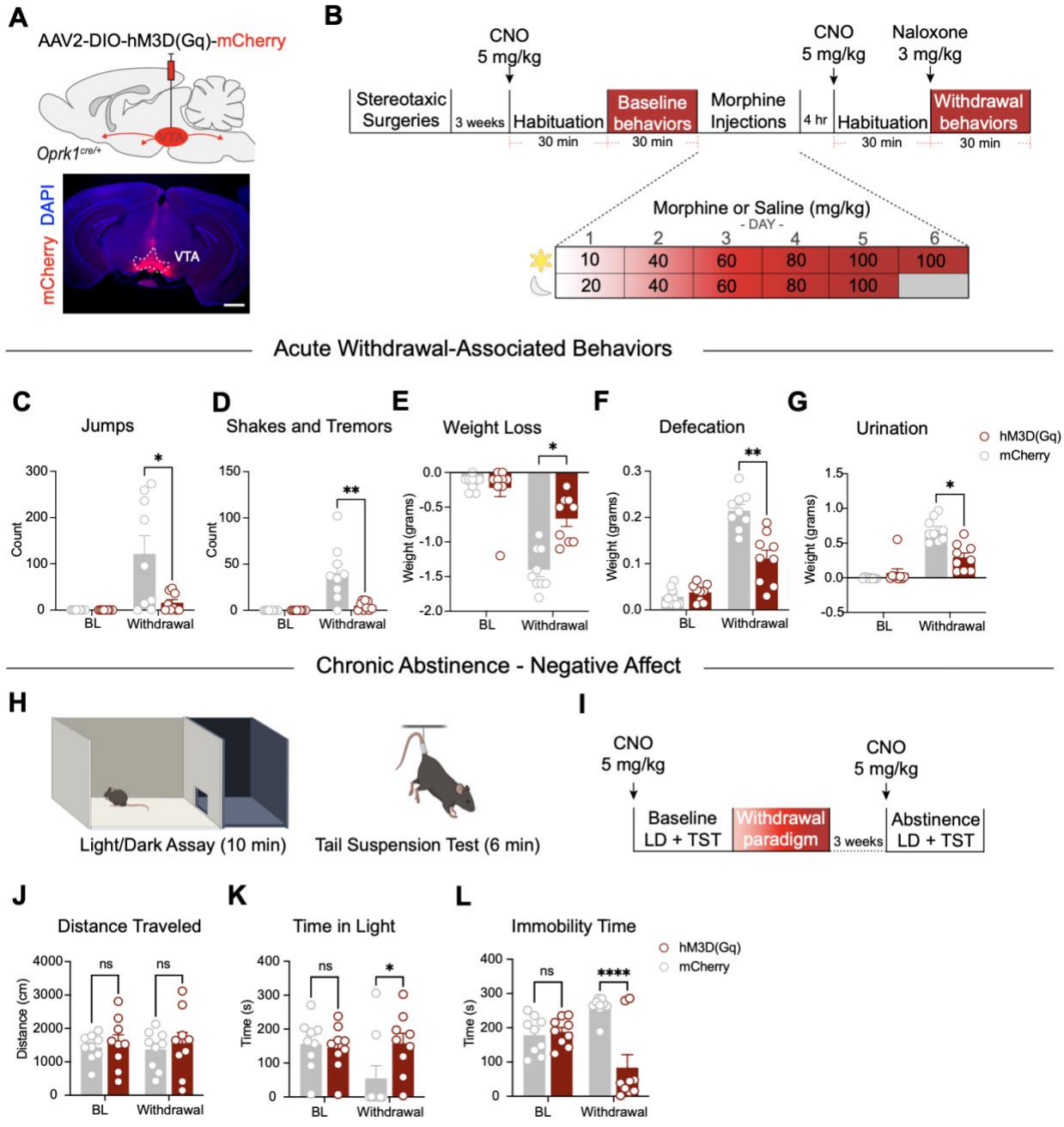

Figure 11 Chemogenetic activation of VTA^{KOR} neurons attenuates acute withdrawal associated-behaviors and chronic abstinence-associated negative affect.

(A) Top: Illustration of viral insertion of hM3D(Gq) into VTA^{KOR} neurons. Bottom: representative image of a mouse VTA slice with mCherry (red) viral reporter. Scale bar = 500 μm. (B) Timeline of naloxone-precipitated morphine withdrawal behavioral paradigm. (C) Quantification of number of jumps before and during morphine withdrawal. Grey bars are mCherry animals, red bars are hM3D(Gq) animals. Data points are individual animals (n = 9 mice per group), and group data is represented as mean ± SEM. *Indicates significantly different (2-way RM ANOVA with Holm-Sidak post-hoc test; $p<0.05$). (D) Quantification of number of shakes and tremors before and during morphine withdrawal. Grey bars are mCherry animals, red bars are hM3D(Gq) animals. Data points are individual animals (n = 9 mice per group), and group data is represented as mean ± SEM. **Indicates significantly different (2-way RM ANOVA with Holm-Sidak post-hoc test; $p<0.01$). (E) Quantification of body weight loss before and during morphine withdrawal. Grey bars are mCherry animals, red bars are hM3D(Gq) animals. Data points are individual animals (n = 9 mice per group), and group data is represented as mean ± SEM. *Indicates significantly different (2-way RM ANOVA with Holm-Sidak post-hoc test; $p<0.05$). (F) Quantification of weight of defecation before and during morphine withdrawal. Grey bars are mCherry animals, red bars are hM3D(Gq) animals. Data points are individual animals (n = 9 mice per group), and group data is represented as mean ± SEM. **Indicates significantly different (2-way RM ANOVA with Holm-Sidak post-hoc test; $p<0.01$). (G) Quantification of weight of urination before and during morphine withdrawal. Grey bars are mCherry animals, red bars are hM3D(Gq) animals. Data points are individual animals (n = 9 mice per group), and group data is represented as mean ± SEM. *Indicates significantly different (2-way RM ANOVA with Holm-Sidak post-hoc test; $p<0.05$). (H) Left: illustration of light-dark (LD) chamber. Right: illustration of tail suspension test (TST). (I) Timeline of chronic abstinence behavioral measurements after opioid withdrawal. (J) Quantification of distance traveled in the LD assay before and three weeks after morphine withdrawal. Grey bars are mCherry animals, red bars are hM3D(Gq) animals. Data points are individual animals (n = 9 mice per group), and group data is represented as mean ± SEM. (K) Quantification of time in the light chamber in the LD assay before and three weeks after morphine withdrawal. Grey bars are mCherry animals, red bars are hM3D(Gq) animals. Data points are individual animals (n = 9 mice per group), and group data is represented as mean ± SEM. *Indicates significantly different (2-way RM ANOVA with Holm-Sidak post-hoc test; $p<0.05$). (K) Quantification of time in the light chamber in the LD assay before and three weeks after morphine withdrawal. Grey bars are mCherry animals, red bars are hM3D(Gq) animals. Data points are individual animals (n = 9 mice per group), and group data is represented as mean ± SEM. *Indicates significantly different (2-way RM

with Holm-Sidak post-hoc test; $p<0.05$). (L) Quantification of immobility in a TST before and three weeks after morphine withdrawal. Grey bars are mCherry animals, red bars are hM3D(Gq) animals. Data points are individual animals (n = 9 mice per group), and group data is represented as mean ± SEM. ****Indicates significantly different (2-way RM ANOVA with Holm-Sidak post-hoc test; $p<0.0001$).

Opioid withdrawal is an emotionally distressing experience, and the VTA is thought to be involved in aversive behaviors in a variety of negative affective states. While acute opioid withdrawal subsides quickly, symptoms of anxiety and depression can persist for weeks after cessation of opioids (Zan et al., 2015). This prolonged negative affective state presents a constant threat to individuals attempting to maintain opioid abstinence long-term. To assess the affective state of mice in chronic abstinence, we performed a light-dark (LD) assay and tail suspension test (TST) (Figure 11H) three weeks after the onset of morphine withdrawal (Figure 11I). Consistent with previous studies, control mice in chronic morphine abstinence show decreased time in the light chamber of a light-dark apparatus without showing significant changes in locomotion generally (Figure 11J-K). However, chemogenetic activation of VTA^{KOR} neurons significantly increased time spent in the light chamber (Figure 11K). Chronic morphine abstinence also increased immobility time in the TST, which was significantly decreased by chemogenetic activation of VTA^{KOR} neurons (Figure 11L). Thus, depressed activity of VTA^{KOR} neurons may underly chronic stress and behavioral despair associated with chronic opioid abstinence.

To further explore the role of VTA^{KOR} neurons in the aversive aspects of opioid withdrawal, we utilized a naloxone-precipitated opioid withdrawal-associated conditioned place aversion (CPA) paradigm (Figure 12A). In opioid-dependent mice expressing hM3D(Gq) in VTA^{KOR} neurons, mice were trained over three days to associate a specific environment with injection of CNO and naloxone (Figure 12B). Consistent with previous studies, opioid-dependent

control mice showed a robust CPA to the naloxone-associated chamber (Azar et al., 2003). However, chemogenetic activation of VTA^{KOR} neurons during the conditioning phase abolished the learning of this negative association (Figure 12C). Taken together, these data suggest that inhibition of VTA^{KOR} neurons drives multiple dimensions of opioid withdrawal, including dysautonomic and gastrointestinal effects, as well as the negative emotional and aversive manifestations of chronic abstinence.

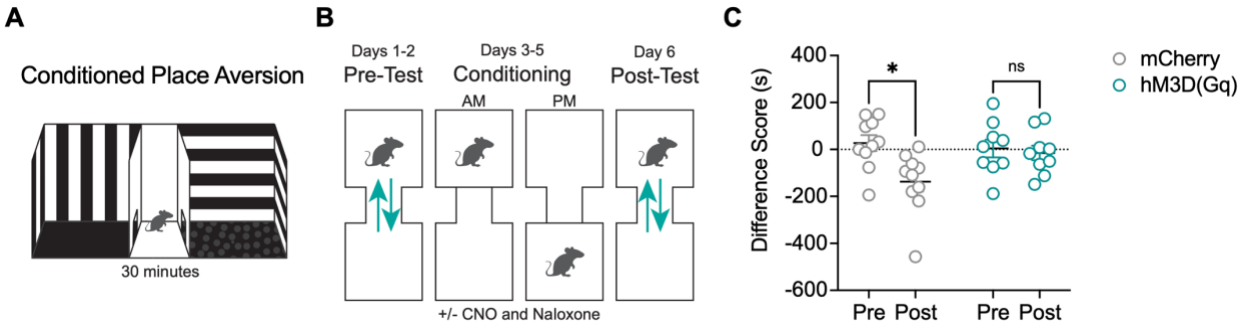

Figure 12 Chemogenetic activation of VTA^{KOR} neurons abolishes naloxone-precipitated opioid withdrawal-associated CPA.

(A) Ilustration of the three-chamber CPA box. (B) Schematic of conditioning paradigm. (C) Quantification of difference in time spent in the naloxone and CNO-paired chamber before and after conditioning. Gray circles are mCherry mice and teal circles are hM3D(Gq) mice. Data points are individual animals (n = 9 mice per group), and group data is represented as mean ± SEM. *Indicates significantly different (2-way RM with Holm-Sidak post-hoc test; $p<0.05$).

Table 3 Summary of F Statistics for ANOVAs in Figure 11

Sub-Figure	Test	Effect	F (DFn, DFd)	p value	Significant?
11C	2-way RM ANOVA with Sidak correction	Interaction	F (1, 16) = 6.988	P=0.0177	Yes
		Withdrawal	F (1, 16) = 11.78	P=0.0034	Yes
		Virus	F (1, 16) = 6.988	P=0.0177	Yes
11D	2-way RM ANOVA with Sidak correction	Interaction	F (1, 16) = 12.36	P=0.0029	Yes
		Withdrawal	F (1, 16) = 20.15	P=0.0004	Yes
		Virus	F (1, 16) = 12.36	P=0.0029	Yes
11E	2-way RM ANOVA with Sidak correction	Interaction	F (1, 16) = 22.30	P=0.0002	Yes
		Withdrawal	F (1, 16) = 97.95	P<0.0001	Yes
		Virus	F (1, 16) = 8.914	P=0.0087	Yes
11F	2-way RM ANOVA with Sidak correction	Interaction	F (1, 16) = 17.99	P=0.0006	Yes
		Withdrawal	F (1, 16) = 94.89	P<0.0001	Yes
		Virus	F (1, 16) = 19.18	P=0.0005	Yes
11G	2-way RM ANOVA with Sidak correction	Interaction	F (1, 16) = 23.91	P=0.0002	Yes
		Withdrawal	F (1, 16) = 92.33	P<0.0001	Yes
		Virus	F (1, 16) = 8.125	P=0.0116	Yes
11J	2-way RM ANOVA with Sidak correction	Interaction	F (1, 16) = 0.1375	P=0.7157	No
		Withdrawal	F (1, 16) = 0.1562	P=0.6979	No
		Virus	F (1, 16) = 0.2248	P=0.6418	No
11K	2-way RM ANOVA with Sidak correction	Interaction	F (1, 16) = 6.191	P=0.0242	Yes
		Withdrawal	F (1, 16) = 3.729	P=0.0714	No
		Virus	F (1, 16) = 1.778	P=0.2011	No
11L	2-way RM ANOVA with Sidak correction	Interaction	F (1, 16) = 24.00	P=0.0002	Yes
		Withdrawal	F (1, 16) = 0.3193	P=0.5799	No
		Virus	F (1, 16) = 10.86	P=0.0046	Yes

4.3.2 VTA^{KOR} neurons project to diverse brain regions

Signals involved in reward, motivated behaviors, and aversion are conveyed from the VTA to many regions of the brain via largely non-overlapping projections to the hindbrain, midbrain, and forebrain (Albanese & Minciacchi, 1983; Breton et al., 2019; Fallon, 1981; Geisler et al.,

2007). Given the necessity of VTA^{KOR} neurons for behavioral responses to opioid withdrawal including diarrhea and micturition as described above, we sought to explore the efferent projections of VTA^{KOR} neurons. Toward this end, a Cre-dependent anterograde AAV encoding mCherry was stereotaxically delivered into the VTA of *Oprk1*^{cre} mice (Figure 13A). We observed VTA^{KOR} efferent projections to numerous regions of the brain (Figure 13B-E; Appendix B Table 1-12). In the rostral forebrain, consisting of the cortex and basal ganglia, we identified mCherry-immunoreactive fibers in the medial prefrontal cortex (mPFC), NAc core and shell (NAcC and NAcSh), caudate-putamen (CPu), and ventral pallidum (Figure 13B, Appendix B Table 1, Appendix B Table 2). In limbic structures such as the thalamus, hypothalamus, and epithalamus, we identified mCherry-immunoreactive fibers in the bed nucleus of the stria terminalis (BNST), lateral habenula (LHb), central medial thalamic nucleus (CM), zona incerta (ZI), and lateral hypothalamus (LH/LHA) (Figure 13C, Appendix B Table 3, Appendix B Table 4, Appendix B Table 5, Appendix B Table 6). In the midbrain and pons, we identified mCherry-immunoreactive fibers in the ventrolateral periaqueductal gray (vlPAG), lateral parabrachial nucleus (lPBN), dorsal raphe (DR), and the pontine reticular nucleus (PnO) (Figure 13D, Appendix B Table 7, Appendix B Table 8, Appendix B Table 9, Appendix B Table 10). Finally, we found mCherry-immunoreactive fibers in a number of medullary regions including the inferior olive (IO), raphe obscurus nucleus (ROb), medullary reticular nuclei (MRn) such as the intermediate reticular nucleus (IRt), the lateral paragigantocellular nucleus (LPGi), the rostral ventromedial medulla (RVM), and sacral spinal cord (Figure 13E, Appendix B Table 11, Appendix B Table 12). Thus, VTA^{KOR} neurons project to several brain regions implicated in hedonic homeostasis, aversion, autonomic dysregulation, and gastrointestinal motility.

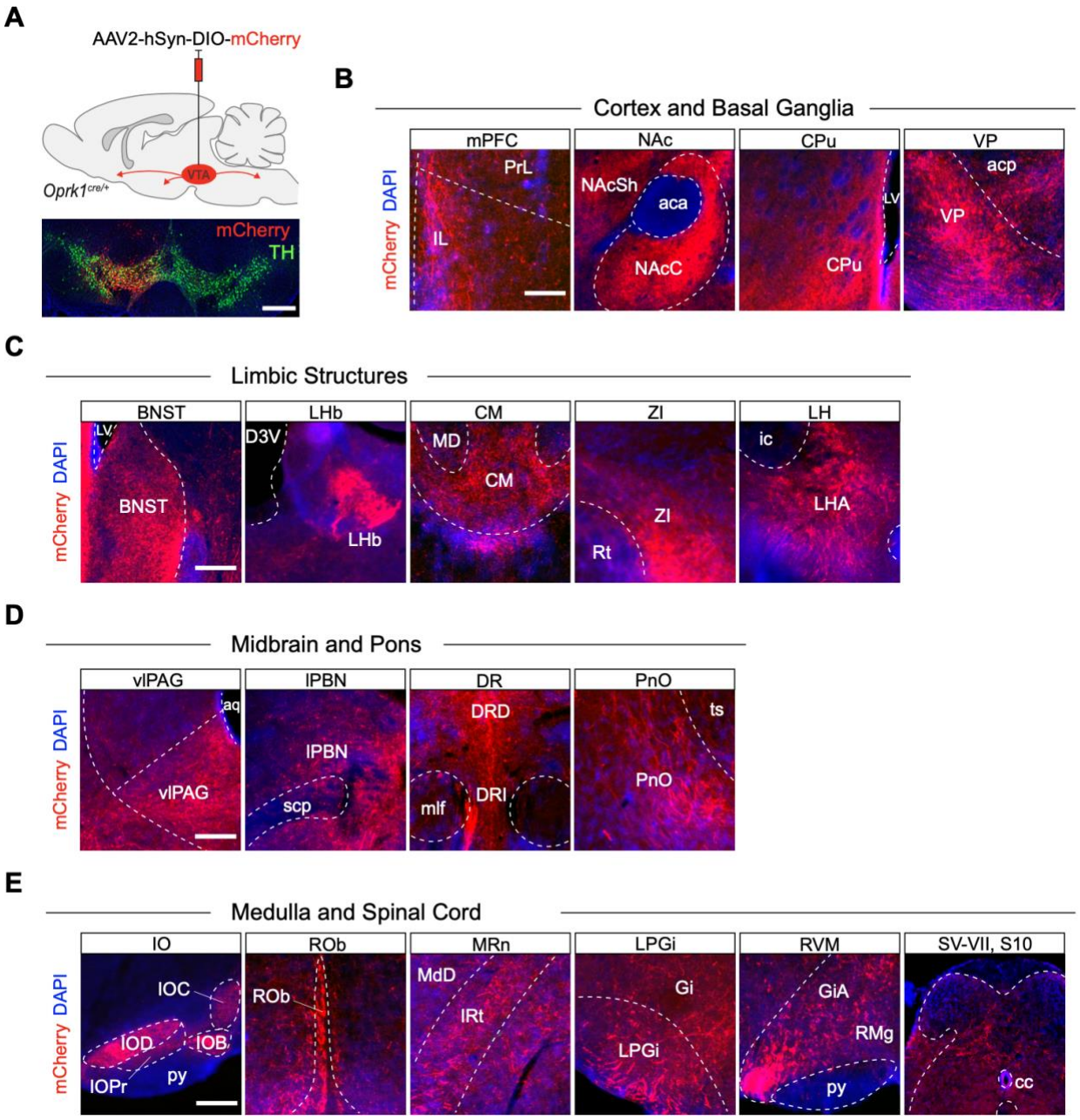

Figure 13 VTA^{KOR} neurons project to diverse regions throughout the forebrain, midbrain, and hindbrain.

(A) Top: illustration of viral delivery of mCherry into VTA^{KOR} neurons. Bottom: representative image of a mouse VTA slice containing mCherry (red)-immunoreactive cell bodies, counterstained with TH (green) to delineate the VTA. Scale bar = 250 µm. (B) Representative images of regions in the cortex and basal ganglia with mCherry (red)-immunoreactive fibers. mPFC, medial prefrontal cortex; PrL, prelimbic cortex; IL, infralimbic cortex; NAc, nucleus accumbens; NAcC, nucleus accumbens core; NAcSh, nucleus accumbens shell; aca, anterior commissure anterior

part; CPu, caudate putamen; VP, ventral pallidum; acp, anterior commissure, posterior. Scale bar = 100 μm. (C) Representative images of regions in the limbic system with mCherry (red)-immunoreactive fibers. BNST, bed nucleus of the stria terminalis; D3V, dorsal third ventricle; LHb, lateral habenula; CM, central medial thalamic nucleus; MD, medial dorsal thalamic nucleus; ZI, zona incerta; Rt, reticular thalamic nucleus; LH/LHA, lateral hypothalamic area; ic, internal capsule. Scale bar = 100 μm. (D) Representative images of regions in the midbrain and pons with mCherry (red)-immunoreactive fibers. vlPAG, ventrolateral periaqueductal gray; aq, aqueduct; lPBN, lateral parabrachial nucleus; scp, superior cerebellar peduncle (brachium conjunctivum); DR, dorsal raphe nucleus; DRD, dorsal raphe nucleus dorsal part; DRI, dorsal raphe nucleus interstitial part; mlf, medial longitudinal fasciculus; PnO, pontine reticular nucleus, oral part; ts, tectospinal tract. Scale bar = 100 μm. (E) Representative images of regions in the medulla and spinal cord with mCherry (red)-immunoreactive fibers. IO, inferior olive; IOPr, inferior olive principal nucleus; IOD, inferior olive dorsal nucleus; IOB, inferior olive subnucleus B of medial nucleus; IOC, inferior olive subnucleus C of medial nucleus; py, pyramidal tract; ROb, raphe obscurus nucleus; MRn, medullary reticular nucleus; MdD, medullary reticular nucleus dorsal part; IRt, intermediate reticular nucleus; LPGi, lateral paragigantocellular nucleus; Gi, giganticellular reticular nucleus; RVM, rostral ventromedial medulla; GiA, giganticellular reticular nucleus alpha part; RMg, raphe magnus nucleus; SV-VII, sacral laminae V-VII; SX, sacral lamina X; cc, central canal. Scale bar = 100 μm.

4.3.3 VTA→vlPAG^{KOR} neurons selectively modulate opioid withdrawal-associated body weight loss, defecation and urination

Given the anatomical diversity of VTA^{KOR} neurons identified above, and the fascinating finding that activating VTA^{KOR} neurons was sufficient to reduce opioid withdrawal-associated defecation, we were particularly interested in exploring which downstream brain targets were critical in modulating the gastrointestinal tract. Specifically, the vlPAG is a critical hub for autonomic function, homeostatic regulation, and the integration of interoceptive signals. At least one previous study has shown opioid signaling as well as the cAMP-PKA pathway in the vlPAG

to be important in opioid withdrawal-associated diarrhea and body weight loss (Maldonado, Fournié-Zaluski, et al., 1992; Punch et al., 1997). Of note, the vlPAG is also an important center for reward; lesions of the vlPAG attenuate preference for morphine (Olmstead & Franklin, 1997). Therefore, we sought to determine whether the subpopulation of VTA^{KOR} neurons projecting to the vlPAG ($VTA \rightarrow vlPAG^{KOR}$ neurons) plays a role in the development of opioid withdrawal symptoms. To this end, an intersectional chemogenetic approach was utilized wherein a retrograde Cre-dependent virus encoding Flp recombinase and an anterograde Flp-dependent AAV encoding the excitatory DREADD hM3D(Gq) were stereotaxically delivered into the vlPAG and VTA, respectively, of *Oprk1*^{cre} mice (Figure 14A). Behaviors were tested in the presence of the DREADD ligand CNO (5 mg/kg IP) both in the opioid-naïve condition and for 30 minutes after eliciting opioid withdrawal (Figure 14B). In opioid-naïve mice, withdrawal-associated behaviors such as jumping, shakes and tremors, body weight loss, defecation, and urination were minimal; CNO significantly decreased body weight loss urination in the hM3D(Gq) group. Furthermore, rapidly eliciting opioid withdrawal with naloxone (3 mg/kg IP) was associated with significant jumping (Figure 14C) and shakes and tremors (Figure 14D), which remained unchanged with chemogenetic activation of $VTA \rightarrow vlPAG^{KOR}$ neurons. However, opioid withdrawal-associated body weight loss (Figure 14E) and defecation (Figure 14F) were significantly reduced when $VTA \rightarrow vlPAG^{KOR}$ neurons were chemogenetically activated by CNO (Table 4). We also observed significant main effects of withdrawal and chemogenetic activation on urination (Figure 14G), though the interaction between these terms was insignificant (Table 4). Thus, depressed activity of $VTA \rightarrow vlPAG^{KOR}$ neurons is specifically critical, at least in part, for the development of acute withdrawal-associated gastrointestinal and urinary effects.

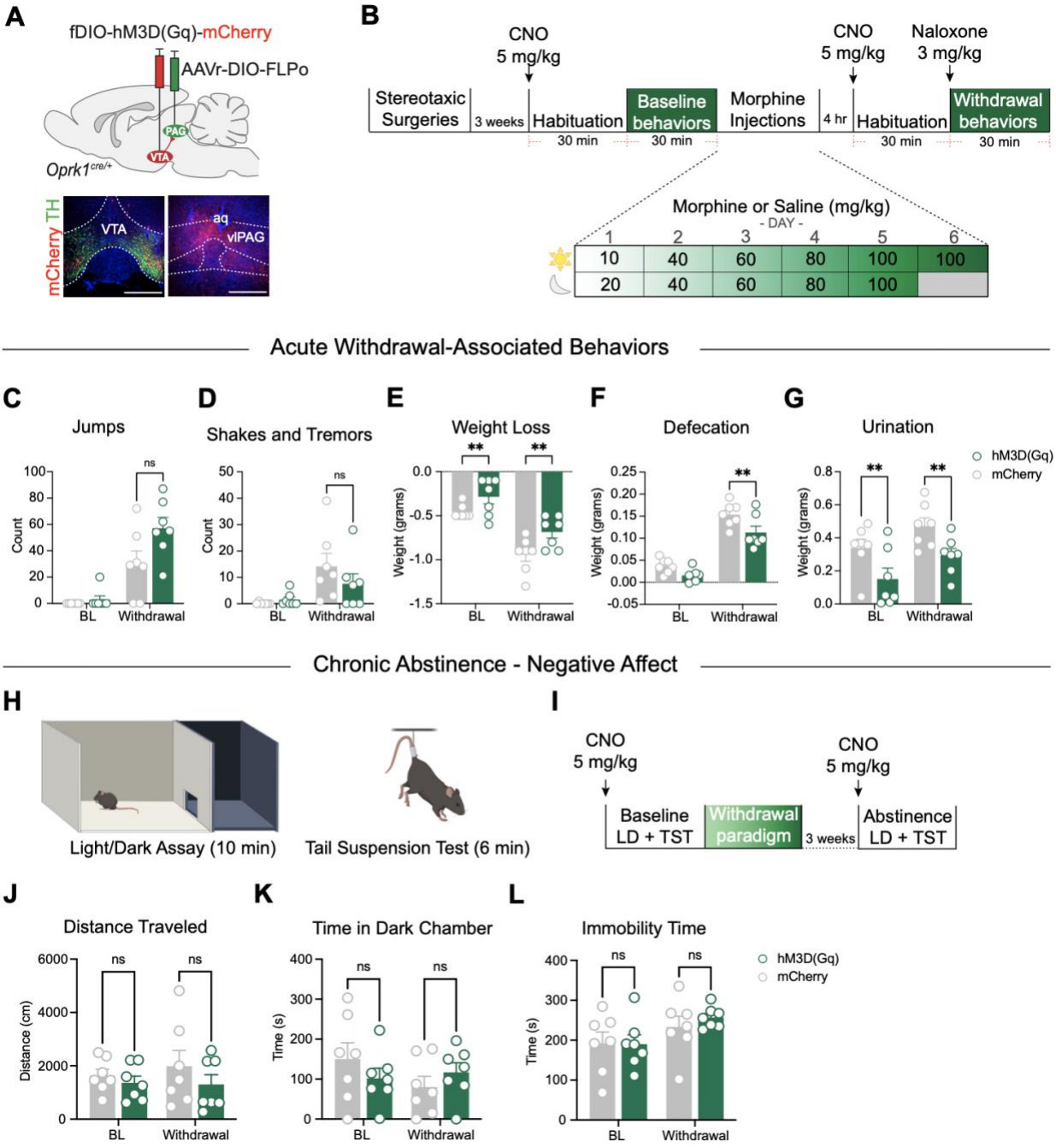

Figure 14 Chemogenetic activation of VTA→vlPAG^{KOR} neurons selectively attenuates opioid-withdrawal associated body weight loss, defecation, and urination.

(A) Top: Illustration of intersectional chemogenetic approach to virally insert hM3D(Gq) into VTA→vlPAG^{KOR} neurons. Bottom left representative image of a mouse VTA slice with mCherry (red)-immunoreactive cell bodies, counterstained with TH (green) to delineate the VTA. Scale bar = 250 µm. Borrom right: representative of a mouse

vlPAG slice with mCherry (red)-immunoreactive fibers. Scale bar = 250 μm. (B) Timeline of naloxone-precipitated morphine withdrawal behavioral paradigm. (C) Quantification of number of jumps before and during morphine withdrawal. Grey bars are mCherry animals, green bars are hM3D(Gq) animals. Data points are individual animals (n = 7 mice per group), and group data is represented as mean ± SEM. (D) Quantification of number of shakes and tremors before and during morphine withdrawal. Grey bars are mCherry animals, green bars are hM3D(Gq) animals. Data points are individual animals (n = 7 mice per group), and group data is represented as mean ± SEM. (E) Quantification of body weight loss before and during morphine withdrawal. Grey bars are mCherry animals, green bars are hM3D(Gq) animals. Data points are individual animals (n = 7 mice per group), and group data is represented as mean ± SEM. **Indicates significantly different (2-way RM ANOVA with Holm-Sidak post-hoc test; $p<0.01$). (F) Quantification of weight of defecation before and during morphine withdrawal. Grey bars are mCherry animals, green bars are hM3D(Gq) animals. Data points are individual animals (n = 7 mice per group), and group data is represented as mean ± SEM. **Indicates significantly different (2-way RM ANOVA with Holm-Sidak post-hoc test; $p<0.01$). (G) Quantification of weight of urination before and during morphine withdrawal. Grey bars are mCherry animals, green bars are hM3D(Gq) animals. Data points are individual animals (n = 7 mice per group), and group data is represented as mean ± SEM. **Indicates significantly different (2-way RM ANOVA with Holm-Sidak post-hoc test; $p<0.01$). (H) Left: illustration of light-dark (LD) chamber. Right: illustration of tail suspension test (TST). (I) Timeline of chronic abstinence behavioral measurements after opioid withdrawal. (J) Quantification of distance traveled in the LD assay before and three weeks after morphine withdrawal. Grey bars are mCherry animals, green bars are hM3D(Gq) animals. Data points are individual animals (n = 7 mice per group), and group data is represented as mean ± SEM. (K) Quantification of time in the light chamber in the LD assay before and three weeks after morphine withdrawal. Grey bars are mCherry animals, green bars are hM3D(Gq) animals. Data points are individual animals (n = 7 mice per group), and group data is represented as mean ± SEM. (K) Quantification of time in the light chamber in the LD assay before and three weeks after morphine withdrawal. Grey bars are mCherry animals, green bars are hM3D(Gq) animals. Data points are individual animals (n = 7 mice per group), and group data is represented as mean ± SEM. L) Quantification of immobility in a TST before and three weeks after morphine withdrawal. Grey bars are mCherry animals, green bars are hM3D(Gq) animals. Data points are individual animals (n = 7 mice per group), and group data is represented as mean ± SEM.

To further assess the role of VTA→vlPAG^{KOR} neurons in the affective state of mice in chronic abstinence, we performed an LD assay and TST (Figure 14H) three weeks after the onset of morphine withdrawal (Figure 14I). Chemogenetic activation of VTA→vlPAG^{KOR} neurons had no significant effect on locomotion (Figure 14J), time spent in the light chamber in a LD assay (Figure 14K), and immobility time in the TST (Figure 14L). Thus, inhibition of VTA→vlPAG^{KOR} neurons is not necessary for the development of opioid-withdrawal associated stress and behavioral despair.

Table 4 Summary of F Statistics for ANOVAs in Figure 14

Sub-Figure	Test	Effect	F (DFn, DFd)	p value	Significant?
14C	2-way RM ANOVA with Sidak correction	Interaction	F (1, 12) = 3.516	P=0.0853	No
		Withdrawal	F (1, 12) = 43.00	P<0.0001	Yes
		Virus	F (1, 12) = 5.093	P=0.0435	Yes
14D	2-way RM ANOVA with Sidak correction	Interaction	F (1, 12) = 1.670	P=0.2206	No
		Withdrawal	F (1, 12) = 10.43	P=0.0072	Yes
		Virus	F (1, 12) = 0.6564	P=0.4336	No
14E	2-way RM ANOVA with Sidak correction	Interaction	F (1, 12) = 0.8308	P=0.0380	Yes
		Withdrawal	F (1, 12) = 55.98	P<0.0001	Yes
		Virus	F (1, 12) = 8.824	P=0.0117	Yes
14F	2-way RM ANOVA with Sidak correction	Interaction	F (1, 12) = 5.093	P=0.0435	Yes
		Withdrawal	F (1, 12) = 103.9	P<0.0001	Yes
		Virus	F (1, 12) = 12.86	P=0.0037	Yes
14G	2-way RM ANOVA with Sidak correction	Interaction	F (1, 12) = 0.006771	P=0.9358	No
		Withdrawal	F (1, 12) = 6.643	P=0.0242	Yes
		Virus	F (1, 12) = 11.47	P=0.0054	Yes
14J	2-way RM ANOVA with Sidak correction	Interaction	F (1, 12) = 0.9881	P=0.3398	No
		Withdrawal	F (1, 12) = 0.4931	P=0.4959	No
		Virus	F (1, 12) = 0.8910	P=0.3638	No
14K	2-way RM ANOVA with Sidak correction	Interaction	F (1, 12) = 1.743	P=0.2114	No
		Withdrawal	F (1, 12) = 0.7331	P=0.4087	No
		Virus	F (1, 12) = 0.04505	P=0.8355	No
14L	2-way RM ANOVA with Sidak correction	Interaction	F (1, 12) = 1.115	P=0.3118	No
		Withdrawal	F (1, 12) = 19.94	P=0.0008	Yes

		Virus	F (1, 12) = 0.1273	P=0.7275	No

4.3.4 Chemogenetic inhibition of VTA^{KOR} neurons does not precipitate opioid withdrawal

Midbrain KOR signaling has been heavily implicated in aversive and negative affective states. Injection of KOR agonists decreases dopamine release in the NAc and hyperpolarizes VTA dopamine neurons (Di Chiara & Imperato, 1988; Margolis et al., 2003). Given the finding that activating VTA^{KOR} neurons, particularly the VTA→vlPAG^{KOR} neural subpopulation, attenuates opioid withdrawal behaviors as described above, we next sought to determine whether inhibition of VTA^{KOR} neurons, as described in the kappa overdrive model, was sufficient to precipitate opioid withdrawal in morphine-dependent mice. To this end, a Cre-dependent anterograde AAV encoding the inhibitory DREADD hM4D(Gi) was stereotaxically delivered into the VTA of *Oprk1^{cre}* mice (Figure 15A). Behaviors were tested in the presence of the DREADD ligand CNO (5 mg/kg IP) both in the opioid-naïve condition and four hours after the final injection of morphine (Figure 15B).

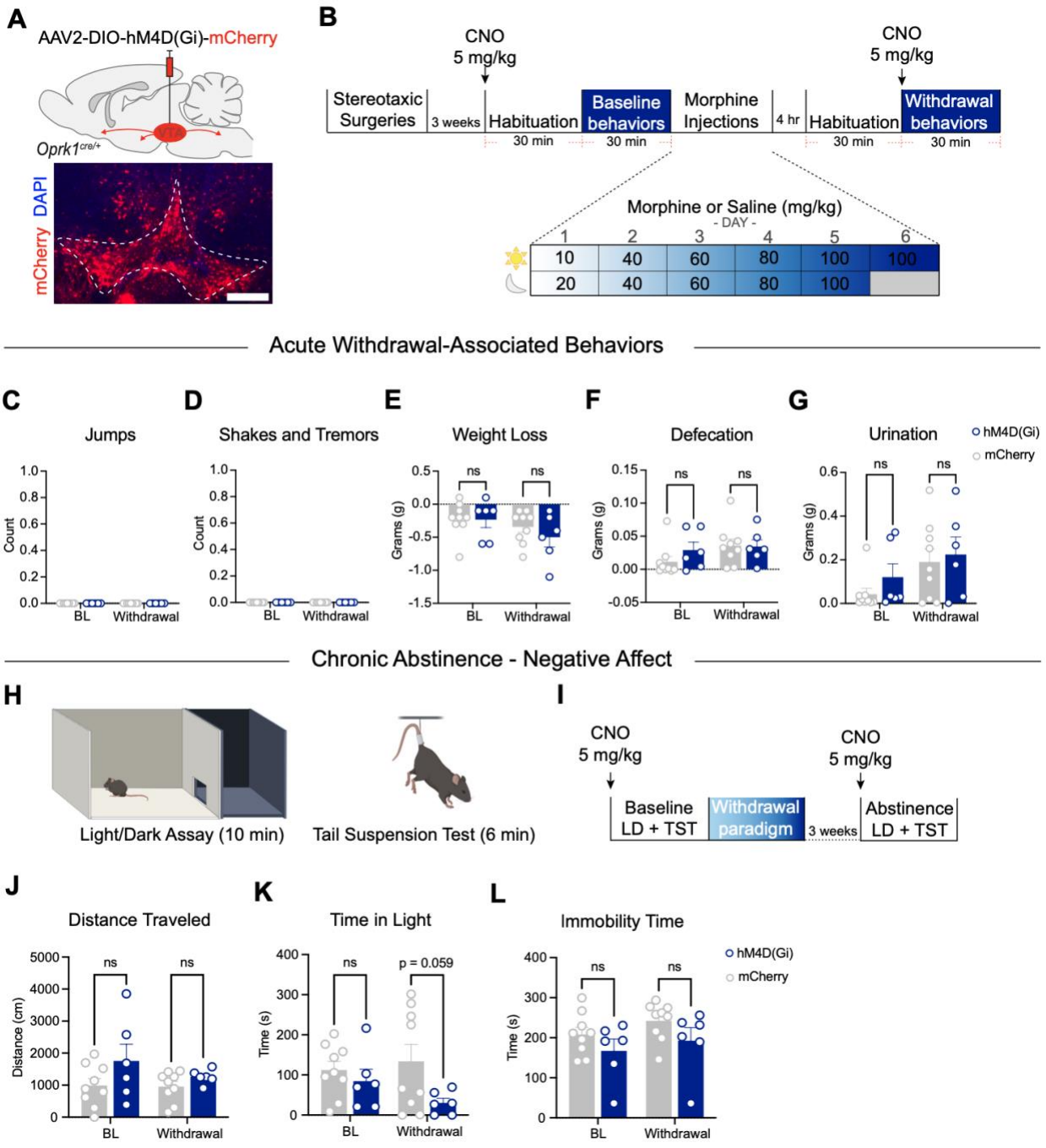

Figure 15 Chemogenetic inhibition of VTA^{KOR} neurons does not precipitate acute opioid withdrawal associated-behaviors and does not exacerbate chronic abstinence-associated negative affect.

(A) Top: Illustration of viral insertion of hM4D(Gi) into VTA^{KOR} neurons. Bottom: representative image of a mouse VTA slice with mCherry (red) viral reporter. Scale bar = 250 µm. (B) Timeline of CNO-precipitated morphine withdrawal behavioral paradigm. (C) Quantification of number of jumps before and during morphine withdrawal.

Grey bars are mCherry animals, blue bars are hM4D(Gi) animals. Data points are individual animals (n = 6 - 9 mice per group), and group data is represented as mean ± SEM. (D) Quantification of number of shakes and tremors before and during morphine withdrawal. Grey bars are mCherry animals, blue bars are hM4D(Gi) animals. Data points are individual animals (n = 6 - 9 mice per group), and group data is represented as mean ± SEM. (E) Quantification of body weight loss before and during morphine withdrawal. Grey bars are mCherry animals, blue bars are hM4D(Gi) animals. Data points are individual animals (n = 6 - 9 mice per group), and group data is represented as mean ± SEM. (F) Quantification of weight of defecation before and during morphine withdrawal. Grey bars are mCherry animals, red bars are hM3D(Gq) animals. Grey bars are mCherry animals, blue bars are hM4D(Gi) animals. Data points are individual animals (n = 6 - 9 mice per group), and group data is represented as mean ± SEM. (G) Quantification of weight of urination before and during morphine withdrawal. Grey bars are mCherry animals, blue bars are hM4D(Gi) animals. Data points are individual animals (n = 6 - 9 mice per group), and group data is represented as mean ± SEM. (H) Left: illustration of light-dark (LD) chamber. Right: illustration of tail suspension test (TST). (I) Timeline of chronic abstinence behavioral measurements after opioid withdrawal. (J) Quantification of distance traveled in the LD assay before and three weeks after morphine withdrawal. Grey bars are mCherry animals, blue bars are hM4D(Gi) animals. Data points are individual animals (n = 6 - 9 mice per group), and group data is represented as mean ± SEM. (K) Quantification of time in the light chamber in the LD assay before and three weeks after morphine withdrawal. Grey bars are mCherry animals, blue bars are hM4D(Gi) animals. Data points are individual animals (n = 6 - 9 mice per group), and group data is represented as mean ± SEM. (L) Quantification of immobility in a TST before and three weeks after morphine withdrawal. Grey bars are mCherry animals, blue bars are hM4D(Gi) animals. Data points are individual animals (n = 6 - 9 mice per group), and group data is represented as mean ± SEM. p=0.059 indicates a trending decrease in time in the light chamber (2-way RM ANOVA with Holm-Sidak post-hoc test).

In opioid-naïve mice, withdrawal-associated behaviors such as jumping, shakes and tremors, body weight loss, defecation, and urination were minimal, and CNO had no effect on these behaviors. Four hours after the induction of morphine dependence, injection of CNO did not significantly increase jumping (Figure 15C), shakes and tremors (Figure 15D), body weight loss (Figure 15E), defecation (Figure 15F), and urination (Figure 15G). Furthermore, when evaluating

chronic abstinence-associated negative affect (Figure 15H-I), chemogenetic inhibition of VTA^{KOR} neurons with CNO had no effect on locomotion (Figure 15J), time in the light chamber (Figure 15K), or immobility time (Figure 15L). Thus, chemogenetic inhibition of VTA^{KOR} neurons was not sufficient to precipitate any of the withdrawal-associated behaviors in morphine-dependent mice.

Table 5 Summary of F Statistics for ANOVAs in Figure 15

Sub-Figure	Test	Effect	F (DFn, DFd)	p value	Significant?
15C	2-way RM ANOVA with Sidak correction	Interaction	F (1, 13) = 0.000	P>0.9999	No
		Drug	F (1, 13) = 0.000	P>0.9999	No
		Virus	F (1, 13) = 0.000	P>0.9999	No
15D	2-way RM ANOVA with Sidak correction	Interaction	F (1, 13) = 0.000	P>0.9999	No
		Drug	F (1, 13) = 0.000	P>0.9999	No
		Virus	F (1, 13) = 0.000	P>0.9999	No
15E	2-way RM ANOVA with Sidak correction	Interaction	F (1, 13) = 0.3987	P=0.5387	No
		Drug	F (1, 13) = 2.890	P=0.1129	No
		Virus	F (1, 13) = 0.7500	P=0.4022	No
15F	2-way RM ANOVA with Sidak correction	Interaction	F (1, 13) = 0.8490	P=0.3736	No
		Drug	F (1, 13) = 2.102	P=0.1708	No
		Virus	F (1, 13) = 0.6547	P=0.4330	No
15G	2-way RM ANOVA with Sidak correction	Interaction	F (1, 13) = 0.1501	P=0.7047	No
		Drug	F (1, 13) = 4.967	P=0.0441	Yes
		Virus	F (1, 13) = 0.9384	P=0.3504	No
15J	2-way RM ANOVA with Sidak correction	Interaction	F (1, 13) = 0.6273	P=0.4426	No
		Drug	F (1, 13) = 0.8134	P=0.3835	No
		Virus	F (1, 13) = 4.822	P=0.0469	Yes
15K	2-way RM ANOVA with Sidak correction	Interaction	F (1, 13) = 1.795	P=0.2032	No
		Drug	F (1, 13) = 0.3321	P=0.5743	No
		Virus	F (1, 13) = 3.495	P=0.0842	No
15L	2-way RM ANOVA with Sidak correction	Interaction	F (1, 13) = 0.2834	P=0.6035	No
		Drug	F (1, 13) = 12.01	P=0.0042	Yes
		Virus	F (1, 13) = 2.115	P=0.1696	No

4.4 Discussion

In this chapter we provide behavioral evidence that VTA^{KOR} neural inhibition is critical in the development of opioid withdrawal. We utilized a genetically engineered mouse expressing Cre-recombinase under the *Oprk1* promoter in order to target VTA^{KOR} neurons in vivo to determine their role in multiple dimensions of opioid withdrawal behavior. We found that activation of VTA^{KOR} neurons was sufficient to attenuate several acute withdrawal behaviors, chronic behavioral despair and anxiety-like behaviors, and withdrawal-associated conditioning. Anterograde tracing of VTA^{KOR} neurons determined these behavioral effects could be due to any of several downstream brain regions. When we activated $VTA{\rightarrow}vlPAG^{KOR}$ neurons specifically, opioid withdrawal-associated body weight loss, diarrhea, and micturition were selectively attenuated. Chemogenetic inhibition of VTA^{KOR} neurons, on the other hand, was not successful in inducing a withdrawal phenotype in opioid-dependent mice. Together, these data strongly implicate a novel circuit in the development of opioid withdrawal.

An important novel finding in our behavioral experiments was the impact of chemogenetic activation of VTA^{KOR} neurons on multiple behavioral dimensions, including gastrointestinal manifestations. This finding indicates that opioids modulate gut motility, at least in part, through central midbrain circuits. While this is not consistent with the consensus that opioids and opioid antagonists alter transit time via peripheral mechanisms, there is some evidence central circuits are involved. For instance, in opioid-dependent mice, injection of naloxone ICV and locally into the VTA is sufficient to induce withdrawal symptoms including diarrhea (Baumeister et al., 1989; Laschka et al., 1976). However, the brain regions and cell types involved in this phenomenon were otherwise unknown. Thus, our findings represent a major conceptual advance in our understanding of how opioids modulate central neural circuits to impact gut function.

Another novel finding was the anatomical diversity of VTA^{KOR} neurons, identified through viral anterograde tracing. VTA^{KOR} neurons project throughout the forebrain, midbrain, and hindbrain, and project as distally as deep laminae of the sacral spinal cord. One drawback to our anterograde tracing experiment is that our approach does not distinguish true synaptic connections from fibers of passage. For example, the LHA is known to house both fibers of passage and GABAergic synapses from the VTA (Yu et al., 2021). To follow-up, an anterograde tracing approach using a synaptophysin-fused reporter virus will be essential to investigate further whether the brain regions identified in our studies indeed receive synaptic input from the VTA.

Another important novel finding in our behavioral experiments was the impact of chemogenetic activation of VTA→vlPAG^{KOR} neurons on gastrointestinal activity in the context of opioid withdrawal. This is consistent with a previous study showing that augmenting enkephalin tone in the PAG modulated withdrawal symptoms, including diarrhea and weight loss (Maldonado, Fournié-Zaluski, et al., 1992). Furthermore, the vlPAG has reciprocal connectivity with the VTA, via sending and receiving GABAergic input (Breton et al., 2019; Omelchenko & Sesack, 2010). Importantly, our tracing studies did not address the neurochemical composition of separate VTA^{KOR} projections. In the future, an in-depth genetic and anatomical characterization of VTA→vlPAG^{KOR} neurons will be essential in our mechanistic understanding of opioid withdrawal circuitry.

One confounding variable in our behavioral experiments is the impact of modulating withdrawal-associated anxiety on gastrointestinal and genitourinary activity, meaning it is possible that activation of VTA^{KOR} neurons reduces diarrhea by reducing negative affect, rather than directly impacting anxiety. This While the behavioral experiments activating VTA→vlPAG^{KOR} neurons decreased withdrawal-associated diarrhea and urination without significantly decreasing

anxiety measures, such as jumping or time in the light chamber on the LD assay, we cannot confirm with certainty the internal affective state of the animals. Taken together, these studies identify a novel circuit mechanism by which KOR agonists and antagonists modulate opioid withdrawal symptoms and join the growing body of evidence that the vlPAG is a critical site in opioid-mediated gastrointestinal motility.

5.0 Chapter 5: Conclusions

5.1 Summary

The purpose of the experiments described in this dissertation was to evaluate the central assertion of the kappa overdrive model of addiction: that chronic opioids augment aversive KOR and dynorphin signaling to inhibit VTA dopamine neural activity, leading to an aversive, dysautonomic, and negative affective state manifested as opioid withdrawal symptoms. In particular, these experiments sought to characterize the anatomy, physiological properties, and function of VTA^{KOR} neurons in the context of opioid dependence and withdrawal. We used a combination of molecular, genetic, physiological, and behavioral approaches to dissect this neural population. Firstly, we used a combination of RNAscope FISH and Cre-dependent viral retrograde tracing to show that chronic opioids increased dynorphin expression in the LC and DR, and that this does not impact inputs to the VTA directly. These experiments, while supportive of the kappa overdrive model, also challenged our assumption that dynorphin would modulate VTA^{KOR} neurons via synapsing at the cell body. Subsequently, we found that opioid withdrawal depressed VTA^{KOR} neuronal activity by augmenting the MOR-mediated inhibition of excitatory and inhibitory drive onto VTA^{KOR} neurons. Finally, our chemogenetic experiments in a behavioral model of opioid withdrawal uncovered a novel cell-type specific circuit from the VTA to the vlPAG which expresses MOR, which is critical in opioid withdrawal-associated diarrhea. Our experiments expand upon our understanding of opioid withdrawal circuits, and of the role of the VTA and other midbrain centers more generally in homeostasis.

5.2 Limitations

5.2.1 Genetic approaches for neural modulation *in vivo*

Intersectional cre- and flp-dependent viral approaches in genetically engineered mice has enabled us to address deeper, more granular questions about brain neurocircuitry and function. Despite our careful design and execution of the experiments used here, there are several shortcomings to utilizing genetic approaches *in vivo* and *ex vivo* which will need to be addressed in future studies. Firstly, the specificity of Cre-mediated recombination is dependent on the stability of promoter expression throughout an animal's development. For example, while our *Oprk1*$^{cre;tdTomato}$ mouse was exceptionally sensitive for identifying VTA^{KOR} neurons (~89%), it was only ~66% specific, meaning in our electrophysiology studies, it is likely we recorded from some KOR- cells. This is likely due to transient expression of KOR during earlier developmental periods. This could be circumvented by targeting VTA^{KOR} neurons virally for electrophysiology experiments; however microinjections run the risk of tissue damage and insufficient or off-target labeling. The construction of the *Oprk1*^{cre} allele also requires the substitution of one copy of the *Oprk1* gene, which could potentially impact the physiology of the neurons and several behavioral sequelae. Furthermore, chemogenetic activation and inhibition do not produce neural activity which endogenous physiological activity. It is also for this reason, at least in part, that it is difficult to interpret our negative findings with chemogenetic inhibition. Finally, CNO as a DREADD ligand has the potential to be metabolized to clozapine, which may have impacted our results on anxiety measures and gastrointestinal function. Going forward, newer DREADD ligands such as compound-21 will need to be evaluated and incorporated into future study designs to limit these confounds.

5.3 Future Directions

5.3.1 Non-canonical neurotransmitters in opioid reward and withdrawal

Canonically, withdrawal-associated aversion is proposed to be dependent on the KOR-dependent inhibition of VTA dopamine neurons projecting to the NAc and mPFC. However, the results of these experiments challenge and expand upon this consensus. Firstly, our RNAscope FISH characterization of VTA^{KOR} neurons has shown that KOR is expressed on not only putative dopamine neurons in the VTA, but also putative glutamate and GABA neurons. These results differ from previously published slice recordings showing that KOR agonists selectively hyperpolarize VTA neurons immunoreactive for TH (Margolis et al., 2003, 2006). There are a few potential explanations for this. Firstly, bath applying KOR agonists in the VTA will only show effects of KOR expression at the cell bodies being patched, whereas RNAscope FISH will identify all VTA^{KOR} neurons regardless of localization of KOR protein in the neuron. Therefore, while KOR localized to the cell body may be specific to putative dopamine neurons, it's likely that additional VTA populations releasing glutamate and GABA may express KOR along the axon or terminal. Consistent with our findings, retrograde chemical tracing has shown putative dopamine neurons only make up approximately one-half of VTA neurons, depending on the projection (Breton 2019). Thus, our findings call into question the necessity of dopamine expression in these circuits for the development of opioid withdrawal.

Given dopamine, glutamate, and GABA expression and release are heavily overlapping in the VTA (Kim et al., 2019; Miranda-Barrientos et al., 2021; Mongia et al., 2019; Yoo et al., 2016), our results highlight the need to further investigate the relative contributions of glutamate and GABA to rewarding and aversive circuits. Until recently, it has been difficult to assess the

relative importance of different neurotransmitters in VTA DA cells which co-express glutamate and GABA. However, novel genetic techniques have inspired new experiments which get at this question. In a recent study, optogenetic activation of VTA glutamate neurons was sufficient to induce real-time place preference and optogenetic self-stimulation even when TH was conditionally ablated from this population with CRISPR AAVs (Zell et al., 2020). Opioid withdrawal also manifests as sex-dependent alterations in VTA GABA neuron activity (Kalamarides et al., 2023). These recent papers, as well as the results of this dissertation, highlight the importance of investigating non-canonical signaling pathways in the context of addiction and withdrawal.

5.3.2 Upstream dynorphin neurons and downstream targets

Our quantitative RNAscope analysis revealed that opioid withdrawal significantly increased prodynorphin mRNA transcript in the LC and DR; however, this effect was not observed in the subset of neurons which projected to the VTA. This indicates that opioid-induced increases in dynorphin signaling do not lead to withdrawal through release of dynorphin in the VTA specifically. There are two possibilities for this finding. Firstly, it is possible that LC and DR neurons are modulating VTA^{KOR} neurons at the axon or the terminal, rather than the cell body. Consistent with this, a recent study found dynorphin neurons in the DR induced social deficits in opioid withdrawal by modulating serotonin neurons projecting to the NAc (Pomrenze et al., 2022). This is consistent with prior work showing that in KOR KO mice, specifically re-expressing KOR in dorsal raphe serotonergic neurons was sufficient to reinstate KOR agonist-induced CPA (Land et al., 2009). Alternatively, the increase in dynorphin tone may impact different circuits altogether.

5.3.3 Opioids and the Brain-Gut Axis

The peripheral mechanisms by which opioids induce constipation (and opioid antagonists diarrhea) are well-characterized and reviewed elsewhere (Bharucha & Lacy, 2020; Farmer et al., 2018). While there exists a vague consensus that opioids modulate gastrointestinal motility through primarily peripheral mechanisms, the results of this dissertation do not support this consensus, and a growing body of evidence has implicated the importance of central circuits in opioid-induced constipation. Opioid agonists administered ICV, particularly MOR and DOR agonists, are constipating in opioid-naïve rodents (Shook et al., 1989). In opioid-dependent rats, opioid withdrawal-associated diarrhea and other behavioral signs could be elicited by administering a peripherally restricted opioid receptor antagonist either systemically or ICV, indicating both central and peripheral mechanisms underly opioid withdrawal-associated diarrhea (Laschka et al., 1976).

Few studies have identified brain regions implicated in these central opioid-mediated mechanisms. Naloxone injection directly into the VTA and substantia nigra of morphine-dependent rats induced opioid withdrawal-associated diarrhea, indicating the ventral midbrain mediates the gastrointestinal effects of opioid withdrawal (Baumeister et al., 1989). Furthermore, injecting a local inhibitor of enkephalin metabolism into the PAG attenuated naloxone precipitated morphine withdrawal in rats, including diarrhea (Maldonado, Negus, et al., 1992). Given the vlPAG is critical for opioid reward (Olmstead and Franklin 1997), we sought to determine the role for VTA^{KOR} neurons projecting to the vlPAG in opioid withdrawal. To our knowledge, our study was the first to identify a functional role for $VTA \rightarrow vlPAG^{KOR}$ neural projections in opioid withdrawal-associated gastrointestinal distress. While this finding represents a major conceptual advance in our understanding of the role of midbrain circuitry in opioid withdrawal, it prompts

many additional questions of study. Going forward, more research effort must be devoted to the neural circuits and substrates underlying the central mechanisms by which opioids impact the brain-gut axis.

Appendix A Quantification of VTA^{KOR} EPSC and IPSC Properties in Opioid Withdrawal

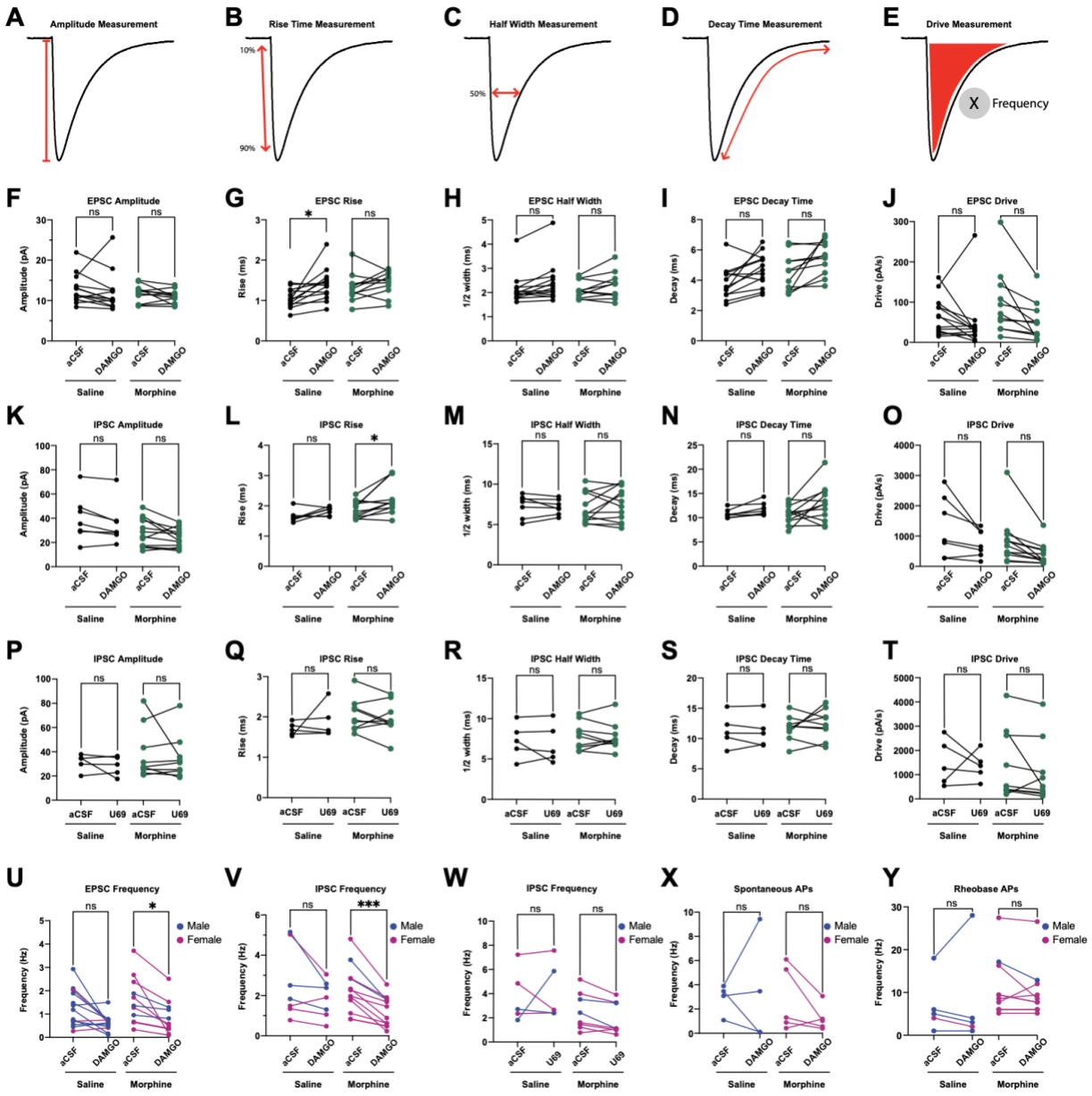

Appendix A Figure 1 Quantification of VTA^{KOR} electrophysiological properties.

(A) Schematic showing EPSC and IPSC amplitude measurement. Amplitude identified as the difference between the average baseline 3 ms before the EPSC (or IPSC) onset and the peak of the EPSC. (B) Schematic showing EPSC and IPSC rise time measurement. Rise time was calculated as the time between 10 and 90% of the EPSC (or IPSC)

amplitude. (C) Schematic showing EPSC and IPSC half width measurement. Half width was calculated as the time between the rise and decay phase of the EPSC (or IPSC) at 50% of the peak even amplitude. (D) Schematic showing the EPSC and IPSC decay time measurement. Decay time was calculated using a single exponential curve. (E) Schematic showing the EPSC and IPSC drive measurement. Drive was calculated as the area above the curve of each even multiplied by the frequency. (F) Quantification of EPSC amplitude in saline and morphine animals before and after DAMGO application. (G) Quantification of EPSC rise in saline and morphine animals before and after DAMGO application. *Indicates significantly different (2-way RM ANOVA with Hom-Sidak post-hoc test; $p<0.05$). (H) Quantification of EPSC half width in saline and morphine animals before and after DAMGO application. (I) Quantification of EPSC decay time in saline and morphine animals before and after DAMGO application. (J) Quantification of EPSC drive in saline and morphine animals before and after DAMGO application. (K) Quantification of IPSC amplitude in saline and morphine animals before and after DAMGO application. (L) Quantification of IPSC rise in saline and morphine animals before and after DAMGO application. *Indicates significantly different (2-way RM ANOVA with Hom-Sidak post-hoc test; $p<0.05$). (M) Quantification of IPSC half width in saline and morphine animals before and after DAMGO application. (N) Quantification of IPSC decay time in saline and morphine animals before and after DAMGO application. (O) Quantification of IPSC drive in saline and morphine animals before and after DAMGO application. (P) Quantification of IPSC amplitude in saline and morphine animals before and after U69 application. (Q) Quantification of IPSC rise in saline and morphine animals before and after U69 application. (R) Quantification of IPSC half width in saline and morphine animals before and after U69 application. (S) Quantification of IPSC decay time in saline and morphine animals before and after U69 application. (T) Quantification of IPSC drive in saline and morphine animals before and after U69 application. (U) Quantification of EPSC frequency in saline and morphine animals before and after DAMGO application. Neurons from male animals are colored blue, neurons from female animals are colored pink. *Indicates significantly different (2-way RM ANOVA with Hom-Sidak post-hoc test; $p<0.05$). (V) Quantification of IPSC frequency in saline and morphine animals before and after DAMGO application. Neurons from male animals are colored blue, neurons from female animals are colored pink. ***Indicates significantly different (2-way RM ANOVA with Hom-Sidak post-hoc test; $p<0.001$). W) Quantification of IPSC frequency in saline and morphine animals before and after U69 application. Neurons from male animals are colored blue, neurons from female animals are colored pink. (X) Quantification of spontaneous action potential frequency in saline and morphine

animals before and after DAMGO application. Neurons from male animals are colored blue, neurons from female animals are colored pink. (Y) Quantification of action potential frequency at rheobase in saline and morphine animals before and after DAMGO application. Neurons from male animals are colored blue, neurons from female animals are colored pink.

Appendix B Quantification of VTA^{KOR} Neurons Throughout the Brain

Appendix B Table 1 Anterograde Tracing of VTA^{KOR} Neurons (Basal Ganglia)

Quantification of number of mice containing mCherry-immunoreactive fibers after injection of AAV2-hSyn-DIO-mCherry into the VTA of *Oprk1*^{cre} mice. n = 6 mice, with 60 µm representative slices collected in triplicate throughout the brain. Regions featured in Figure 13 are highlighted in green.

Category	Region Abbr.	Region Description	Fibers present?						TOTAL
			1	2	3	4	5	6	
Ventral Striatum	AcbSh/LAcbSh	accumbens nucleus, shell	Y	Y	Y	Y	Y	Y	6
Ventral Striatum	AcbC	accumbens nucleus, core	Y	Y	Y	Y	Y	Y	6
Ventral Striatum	Tu	olfactory tubercle	N	Y	Y	Y	Y	N	4
Ventral Striatum	ICj	islands of Calleja	N	Y	N	N	N	N	1
Dorsal Striatum	CPu	caudate putamen	Y	Y	Y	Y	Y	Y	6
Associated Structures	SI	substantia innominata	Y	N	Y	Y	Y	Y	5
Misc.	VP	ventral pallidum	Y	Y	Y	Y	Y	Y	6
Misc.	LGP	lateral globus pallidus	N	Y	Y	Y	N	N	3
Misc.	MGP	medial globus pallidus (entopeduncular nucleus)	N	N	Y	N	N	N	1
Misc.	ns	nigrostriatal bundle	Y	Y	Y	Y	Y	Y	6
Substantia Nigra	SNR	substantia nigra, reticular part	N	N	Y	N	N	N	1
Substantia Nigra	SNC	substantia nigra, compact part	N	N	Y	N	N	N	1

Appendix B Table 2 Anterograde Tracing of VTA^{KOR} Neurons (Cortex)

Quantification of number of mice containing mCherry-immunoreactive fibers after injection of AAV2-hSyn-DIO-mCherry into the VTA of *Oprk1^{cre}* mice. n = 6 mice, with 60 µm representative slices collected in triplicate throughout the brain. Regions in Figure 13 are highlighted in green.

Category	Region Abbr.	Region Description	Fibers present?						TOTAL
			1	2	3	4	5	6	
Medial Prefrontal Cortex	Cg2	cingulate cortex, area 2	Y	N	N	N	N	N	1
Medial Prefrontal Cortex	IL	infralimbic cortex	Y	Y	N	Y	Y	Y	5
Medial Prefrontal Cortex	PrL	prelimbic cortex	N	Y	Y	N	Y	N	3
Orbitomedial Prefrontal Cortex	MO	medial orbital cortex	Y	Y	N	N	Y	Y	4
Orbitomedial Prefrontal Cortex	VO	ventral orbital cortex	Y	Y	N	N	N	N	2
Misc.	Pir	piriform cortex	N	Y	N	N	N	N	1
Misc.	RSG	retrosplenial granular cortex	N	Y	Y	N	N	N	2
Misc.	RSA	retrosplenial agranular cortex	N	N	Y	N	N	N	1
Misc.	DP	dorsal peduncular cortex	N	Y	N	N	N	Y	2
Misc.	V1	primary visual cortex	N	N	Y	N	N	N	1
Misc.	ic	internal capsule	N	N	Y	N	N	Y	2
Olfactory Bulb	VTT	ventral tenia tecta	N	Y	N	N	N	N	1
Olfactory Bulb	DTT	dorsal tenia tecta	N	Y	N	N	N	N	1
Olfactory Bulb	IPF	interpeduncular fossa	N	Y	N	N	N	N	1
Olfactory Bulb	Mi	mitral cell layer of the olfactory bulb	N	Y	N	N	N	N	1
Olfactory Bulb	EPI	external plexiform layer of the olfactory bulb	N	Y	N	N	N	N	1
Corpus Callosum	fmi	forceps minor of the corpus callosum	N	N	Y	N	Y	N	2
Corpus Callosum	f	fornix	Y	N	N	N	Y	Y	3
Anterior Commisure	aca	anterior commisure, anterior part	Y	Y	Y	N	N	N	3
Anterior Commisure	acp	anterior commissure, posterior	N	N	N	Y	N	N	1
Anterior Commisure	IPACM	interstitial nucleus of the posterior limb of the anterior commissure, medial part	N	Y	Y	Y	Y	Y	5
Anterior Commisure	IPACL	interstitial nucleus of the posterior limb of the anterior commissure, lateral part	N	Y	Y	Y	Y	N	4
Anterior Commisure	AC	anterior commissural nucleus	N	N	Y	N	N	N	1
Posterior Commissure	pc	posterior commissure	N	N	Y	N	N	N	1
Posterior Commissure	PCom	nucleus of the posterior commissure	N	N	N	Y	N	N	1

Appendix B Table 3 Anterograde Tracing of VTA^{KOR} Neurons (Thalamus)

Quantification of number of mice containing mCherry-immunoreactive fibers after injection of AAV2-hSyn-DIO-mCherry into the VTA of *Oprk1^{cre}* mice. n = 6 mice, with 60 µm representative slices collected in triplicate throughout the brain. Regions featured in Figure 13 are highlighted in green.

Category	Region Abbr.	Region Description	Fibers present?						TOTAL
			1	2	3	4	5	6	
Thalamus	LHb	lateral habenular nucleus	Y	Y	Y	Y	Y	Y	6
Thalamus	MHb	medial habenular nucleus	Y	N	N	Y	N	Y	3
Thalamus	fr	fasciculus retroflexus	N	N	Y	N	N	Y	2
Thalamus	MD	mediodorsal thalamic nucleus	Y	Y	Y	N	Y	N	4
Thalamus	MDL	mediodorsal thalamic nucleus, lateral part	N	N	N	N	N	Y	1
Thalamus	PT	paratenial thalamic nucleus	Y	N	N	N	N	N	1
Thalamus	Rt	reticular thalamic nucleus	N	N	Y	N	N	Y	2
Thalamus	CM	central medial thalamic nucleus	Y	Y	Y	Y	Y	Y	6
Thalamus	Re	reuniens thalamic nucleus	Y	Y	N	N	Y	N	3
Thalamus	PC	paracentral thalamic nucleus	N	Y	N	N	N	N	1
Thalamus	VM	ventromedial thalamic nucleus	N	Y	Y	N	Y	Y	4
Thalamus	PV	paraventricular thalamic nucleus	Y	N	N	Y	N	Y	3
Thalamus	PF	parafascicular thalamic nucleus	N	N	N	N	N	Y	1
Thalamus	LDVL	laterodorsal thalamic nucleus, ventrolateral part	N	N	N	N	Y	N	1
Thalamus	LDDM	laterodorsal thalamic nucleus, dorsomedial part	N	N	N	N	Y	N	1
Thalamus	Rh	rhomboid thalamic nucleus	Y	N	N	Y	N	N	2
Thalamus	IMD	intermediodorsal thalamic nucleus	Y	Y	Y	N	N	Y	4
Thalamus	STh	subthalamic nucleus	N	N	Y	Y	N	Y	3
Thalamus	PSTh	parasubthalamic nucleus	N	N	Y	N	N	Y	2
Thalamus	ZI	zona incerta	N	Y	N	N	N	Y	2
Thalamus	ZID	zona incerta, dorsal part	Y	Y	Y	Y	Y	Y	6
Thalamus	ZIV	zona incerta, ventral part	Y	Y	N	Y	Y	Y	5
Thalamus	sm	stria medullaris of the thalamus	N	N	N	Y	N	Y	2
Thalamus	mt	mammillothalamic tract	N	N	N	N	Y	Y	2
Thalamus	pv	periventricular fiber system	N	Y	N	Y	N	Y	3
Thalamus	SMT	submammillothalamic nucleus	N	Y	N	N	N	N	1
Thalamus	Gus	gustatory thalamic nucleus	N	N	Y	N	N	N	1

Appendix B Table 4 Anterograde Tracing of VTA^{KOR} Neurons (Hypothalamus)

Quantification of number of mice containing mCherry-immunoreactive fibers after injection of AAV2-hSyn-DIO-mCherry into the VTA of *Oprk1^{cre}* mice. n = 6 mice, with 60 µm representative slices collected in triplicate throughout the brain. Regions featured in Figure 13 are highlighted in green.

Category	Region Abbr.	Region Description	Fibers present?						TOTAL
			1	2	3	4	5	6	
Hypothalamus	Pe	Periventricular hypothalamic nucleus	N	Y	Y	N	N	N	2
Hypothalamus	LH	lateral hypothalamic area	Y	Y	Y	Y	Y	Y	6
Hypothalamus	PH	posterior hypothalamic area	N	Y	Y	N	N	Y	3
Hypothalamus	MCLH	magnocellular nucleus of the lateral hypothalamus	Y	Y	N	N	N	Y	3
Hypothalamus	DM	dorsomedial hypothalamic nucleus	N	N	Y	Y	N	N	2
Hypothalamus	DMD	dorsomedial hypothalamic nucleus, dorsal part	Y	N	N	N	N	N	1
Hypothalamus	LPO	lateral preoptic area	Y	N	Y	Y	Y	Y	5
Hypothalamus	MPA	medial preoptic area	Y	N	N	N	Y	Y	3
Hypothalamus	MCPO	magnocellular preoptic nucleus	Y	Y	N	Y	Y	Y	5
Hypothalamus	MnPO	median preoptic nucleus	Y	N	N	N	N	Y	2
Hypothalamus	VMPO	ventromedial preoptic nucleus	N	N	Y	N	N	N	1
Hypothalamus	ADP	anterodorsal preoptic nucleus	N	Y	N	N	N	N	1
Hypothalamus	Arc	arcuate hypothalamic nucleus	N	N	Y	N	N	N	1
Hypothalamus	ArcLP	arcuate hypothalamic nucleus, lateroposterior part	N	N	Y	N	N	N	1
Hypothalamus	ArcMP	arcuate hypothalamic nucleus, medial posterior part	N	N	Y	Y	N	N	2
Hypothalamus	LA	lateroanterior hypothalamic nucleus	N	Y	N	N	N	N	1
Hypothalamus	A14	A14 dopamine cells	N	Y	N	N	N	N	1
Hypothalamus	3V	3rd ventricle	N	Y	Y	N	N	N	2
Hypothalamus	SCh	suprachiasmatic nucleus	N	N	Y	N	N	N	1
Hypothalamus	PaMP	paraventricular hypothalamic nucleus, medial parvicellular part	N	Y	N	N	N	N	1
Hypothalamus	PaMM	paraventricular hypothalamic nucleus, medial magnocellular part	N	Y	Y	N	N	N	2
Hypothalamus	PaLM	paraventricular hypothalamic nucleus, lateral magnocellular part	N	Y	N	N	N	N	1
Hypothalamus	PaPo	paraventricular hypothalamic nucleus, posterior part	N	Y	N	N	N	N	1
Hypothalamus	AHP	anterior hypothalamic area, posterior part	N	Y	Y	N	N	N	2
Hypothalamus	SubI	subincertal nucleus	N	N	Y	N	Y	N	2
Hypothalamus	ME	median eminence	N	N	N	Y	N	N	1
Hypothalamus	Gem	gemini hypothalamic nucleus	N	N	N	Y	N	N	1
Hypothalamus	DTM	dorsal tuberomammillary nucleus	N	N	Y	N	N	N	1

Appendix B Table 5 Anterograde Tracing of VTA^{KOR} Neurons (Amygdala)

Quantification of number of mice containing mCherry-immunoreactive fibers after injection of AAV2-hSyn-DIO-mCherry into the VTA of *Oprk1^{cre}* mice. n = 6 mice, with 60 µm representative slices collected in triplicate throughout the brain. Regions featured in Figure 13 are highlighted in green.

Category	Region Abbr.	Region Description	Fibers present?						TOTAL
			1	2	3	4	5	6	
Amygdala	CeM	central amygdaloid nucleus, medial division	N	N	Y	N	N	N	1
Amygdala	Me	medial amygdaloid nucleus	N	N	N	Y	N	N	1
Amygdala	ACo	anterior cortical amygdaloid nucleus	N	Y	Y	N	N	N	2
Amygdala	CxA	cortex-amygdala transition zone	N	Y	Y	N	N	N	2
Amygdala	I	intercalated nuclei of the amygdala	N	Y	Y	N	N	N	2
Amygdala	SLEA	sublenticular extended amygdala	Y	N	Y	Y	N	N	3
Amygdala	SLEAC	sublenticular extended amygdala, central part	N	N	Y	Y	Y	Y	4
Amygdala	SLEAM	sublenticular extended amygdala, medial part	Y	N	Y	Y	Y	Y	5
Amygdala	AAV	anterior amygdaloid area, ventral part	N	Y	Y	N	N	Y	3
Amygdala	AAD	anterior amygdaloid area, dorsal part	N	Y	Y	Y	Y	Y	5
Amygdala	LOT	nucleus of the lateral olfactory tract	N	Y	Y	N	N	N	2

Appendix B Table 6 Anterograde Tracing of VTA^{KOR} Neurons (Misc. Limbic)

Quantification of number of mice containing mCherry-immunoreactive fibers after injection of AAV2-hSyn-DIO-mCherry into the VTA of *Oprk1^{cre}* mice. n = 6 mice, with 60 µm representative slices collected in triplicate throughout the brain. Regions featured in Figure 13 are highlighted in green.

Category	Region Abbr.	Region Description	Fibers present?						TOTAL
			1	2	3	4	5	6	
(n/a)	BST	bed nucleus of the stria terminalis	Y	Y	Y	Y	Y	Y	6
(n/a)	BSTLV	bed nucleus of the stria terminalis, lateral division, ventral part	N	Y	Y	N	N	Y	3
(n/a)	BSTLP	bed nucleus of the stria terminalis, lateral division, posterior part	Y	N	N	Y	N	N	2
(n/a)	BSTLD	bed nucleus of the stria terminalis, lateral division, dorsal part	Y	N	N	N	N	N	1
(n/a)	BSTMPI	bed nucleus of the stria terminalis, medial division, posterointermediate part	N	N	N	N	N	Y	1
(n/a)	BSTMPL	bed nucleus of the stria terminalis, medial division, posterolateral part	N	N	N	N	N	Y	1
(n/a)	mfb	medial forebrain bundle	Y	Y	Y	Y	Y	Y	6
Septal Area	MS	medial septal nucleus	N	Y	Y	N	Y	Y	4
Septal Area	LSD	lateral septal nucleus, dorsal part	Y	Y	N	N	N	N	2
Septal Area	LSV	lateral septal nucleus, ventral part	Y	Y	N	N	N	N	2
Septal Area	LSI	lateral septal nucleus, intermediate part	N	Y	N	N	N	N	1
Septal Area	Ld	lambdoid septal zone	N	Y	N	N	Y	Y	3
Diagonal Band of Broca	VDB	nucleus of the vertical limb of the diagonal band	N	N	N	N	Y	Y	2
Diagonal Band of Broca	HDB	nucleus of the horizontal limb of the diagonal band	Y	Y	Y	Y	Y	Y	6

Appendix B Table 7 Anterograde Tracing of VTA^{KOR} Neurons (Reticular Formation)

Quantification of number of mice containing mCherry-immunoreactive fibers after injection of AAV2-hSyn-DIO-mCherry into the VTA of *Oprk1^{cre}* mice. n = 6 mice, with 60 µm representative slices collected in triplicate throughout the brain. Regions featured in Figure 13 are highlighted in green.

Category	Region Abbr.	Region Description	Fibers present?						TOTAL
			1	2	3	4	5	6	
Midbrain Reticular Formation	MnR	median raphe nucleus	Y	Y	N	Y	Y	N	4
Midbrain Reticular Formation	PMnR	paramedian raphe nucleus	Y	Y	N	Y	N	Y	4
Midbrain Reticular Formation	DR	dorsal raphe nucleus	Y	Y	N	N	N	Y	3
Midbrain Reticular Formation	DRC	dorsal raphe nucleus, caudal part	Y	Y	Y	N	N	Y	4
Midbrain Reticular Formation	DRI	dorsal raphe nucleus, interfascicular part	Y	Y	Y	Y	N	Y	5
Midbrain Reticular Formation	DRD	dorsal raphe nucleus, dorsal part	Y	N	Y	Y	N	N	3
Midbrain Reticular Formation	DRV	dorsal raphe nucleus, ventral part	Y	N	Y	Y	N	N	3
Midbrain Reticular Formation	DRVL	dorsal raphe nucleus, ventrolateral part	Y	N	Y	Y	N	N	3
Midbrain Reticular Formation	RC	raphe cap	Y	N	N	N	N	Y	2
Pontine Reticular Formation	PnR	pontine raphe nucleus	N	Y	Y	N	N	N	2
Pontine Reticular Formation	PnC	pontine reticular nucleus, caudal part	N	Y	Y	Y	Y	Y	5
Pontine Reticular Formation	PnV	pontine reticular nucleus, ventral part	N	N	N	N	N	Y	1
Pontine Reticular Formation	PnO	pontine reticular nucleus, oral part	Y	Y	Y	Y	Y	Y	6
Medullary Reticular Nuclei	MdV	medullary reticular nucleus, ventral part	Y	Y	Y	Y	Y	Y	6
Medullary Reticular Nuclei	MdD	medullary reticular nucleus, dorsal part	Y	N	Y	Y	Y	Y	5
Medullary Reticular Nuclei	IRt	intermediate reticular nucleus	Y	Y	Y	Y	Y	Y	6
Medullary Reticular Nuclei	LRt	lateral reticular nucleus	Y	Y	Y	Y	Y	Y	6
Medullary Reticular Nuclei	PMn	paramedian reticular nucleus	Y	Y	N	Y	Y	N	4
Medullary Reticular Nuclei	RVL	rostroventrolateral reticular nucleus	Y	Y	N	Y	Y	Y	5
Medullary Reticular Nuclei	GiV	gigantocellular reticular nucleus, ventral part	N	Y	N	Y	Y	N	3

Appendix B Table 8 Anterograde Tracing of VTA^{KOR} Neurons (Midbrain)

Quantification of number of mice containing mCherry-immunoreactive fibers after injection of AAV2-hSyn-DIO-mCherry into the VTA of *Oprk1^{cre}* mice. n = 6 mice, with 60 µm representative slices collected in triplicate throughout the brain. Regions featured in Figure 13 are highlighted in green.

Category	Region Abbr.	Region Description	Fibers present?						TOTAL
			1	2	3	4	5	6	
Periaqueductal Gray	PAG	periaqueductal gray	Y	Y	Y	Y	Y	Y	6
Periaqueductal Gray	VLPAG	ventrolateral periaqueductal gray	Y	Y	Y	Y	Y	Y	6
Parabrachial Nucleus	MPB	medial parabrachial nucleus	N	Y	N	Y	N	Y	3
Parabrachial Nucleus	LPB	lateral parabrachial nucleus	N	N	N	Y	Y	Y	3
Parabrachial Nucleus	LPBV	lateral parabrachial nucleus, ventral part	N	N	N	N	N	Y	1
Parabrachial Nucleus	LPBC	lateral parabrachial nucleus, central part	N	N	N	N	N	Y	1
Parabrachial Nucleus	LPBI	lateral parabrachial nucleus, internal part	N	N	N	N	N	Y	1
Parabrachial Nucleus	LPBD	lateral parabrachial nucleus, dorsal part	N	N	N	N	N	Y	1
Parabrachial Nucleus	LPBE	lateral parabrachial nucleus, external part	N	N	N	Y	N	Y	2
Ventral Tegmental Area	PBP	parabrachial pigmented nucleus	Y	Y	Y	Y	Y	Y	6
Ventral Tegmental Area	PN	paranigral nucleus	Y	Y	Y	Y	Y	Y	6
Ventral Tegmental Area	RLi	rostral linear nucleus of the raphe	Y	Y	Y	Y	Y	Y	6
Ventral Tegmental Area	CLi	caudal linear nucleus of the raphe	Y	Y	Y	Y	Y	Y	6
Ventral Tegmental Area	IF	interfascicular nucleus	Y	Y	Y	Y	Y	Y	6
Tegmentum	VTg	ventral tegmental nucleus	N	N	N	Y	N	N	1
Tegmentum	VLTg	ventrolateral tegmental area	Y	N	N	Y	N	N	2
Tegmentum	LDTg	laterodorsal tegmental nucleus	N	Y	Y	Y	N	Y	4
Tegmentum	LDTgV	laterodorsal tegmental nucleus, ventral part	N	N	Y	N	N	Y	2
Tegmentum	DTgP	dorsal tegmental nucleus, pericentral part	N	Y	N	N	N	N	1
Tegmentum	DTgC	dorsal tegmental nucleus, central part	N	N	N	Y	N	N	1
Tegmentum	DMTg	dorsomedial tegmental area	Y	Y	Y	N	N	Y	4
Tegmentum	PPTg	pedunculopontine tegmental nucleus	Y	N	Y	N	N	Y	3
Tegmentum	SPTg	subpedencular tegmental nucleus	N	N	Y	N	N	N	1
Tegmentum	A8	A8 dopamine cells	N	Y	N	N	N	N	1
Tegmentum	IPR	interpeduncular nucleus, rostral subnucleus	Y	Y	N	N	N	N	2

Appendix B Table 9 Anterograde Tracing of VTA^{KOR} Neurons (Midbrain cont.)

Quantification of number of mice containing mCherry-immunoreactive fibers after injection of AAV2-hSyn-DIO-mCherry into the VTA of *Oprk1^{cre}* mice. n = 6 mice, with 60 µm representative slices collected in triplicate throughout the brain. Regions featured in Figure 13 are highlighted in green.

Category	Region Abbr.	Region Description	Fibers present?						TOTAL
			1	2	3	4	5	6	
Cerebellar Tracts	scp	superior cerebellar peduncle (brachium conjunctivum)	N	Y	Y	Y	Y	Y	5
Cerebellar Tracts	mcp	middle cerebellar peduncle	N	N	Y	N	N	N	1
Cerebellar Tracts	bp	brachium pontis (stem of middle cerebellar peduncle	N	Y	N	N	N	N	1
Cerebellar Tracts	vsc	ventral spinocerebellar tract	N	N	Y	N	N	N	1
Spinal Tracts	LVPO	lateroventral periolivary nucleus	N	N	N	N	Y	Y	2
Spinal Tracts	DPO	dorsal periolivary region	N	N	N	N	Y	N	1
Spinal Tracts	EW	Edinger-Westphal nucleus	Y	Y	N	N	N	N	2
Spinal Tracts	InCG	interstitial nucleus of Cajal, greater part	N	Y	N	N	N	N	1
Spinal Tracts	DpMe	deep mesencephalic nucleus	Y	Y	N	N	Y	Y	4
Spinal Tracts	PL	paralemniscal nucleus	N	N	N	Y	N	N	1
Spinal Tracts	VLL	ventral nucleus of the lateral lemniscus	N	N	N	N	N	Y	1
Spinal Tracts	PR	prerubral field	N	N	N	Y	N	N	1
Spinal Tracts	RR	retrorubral nucleus	N	N	N	N	N	Y	1
Spinal Tracts	RRF	retrorubral field	N	Y	N	N	N	N	1
Spinal Tracts	rs	rubrospinal tract	N	Y	N	N	N	Y	2
Cranial Nerves	Pr5	principal sensory trigeminal nucleus	N	N	Y	N	N	N	1
Cranial Nerves	Pr5VL	principal sensory trigeminal nucleus, ventrolateral part	N	N	Y	Y	N	N	2
Cranial Nerves	PC5	parvicellular motor trigeminal nucleus	N	N	Y	N	N	N	1
Cranial Nerves	Mo5	motor trigeminal nucleus	Y	N	N	Y	N	N	2
Cranial Nerves	Su5	supratrigeminal nucleus	N	N	N	Y	N	N	1
Cranial Nerves	I5	intertrigeminal nucleus	N	N	N	Y	N	N	1
Cranial Nerves	P5	peritrigeminal zone	Y	N	Y	Y	N	N	3
Cranial Nerves	Pa4	paratrochlear nucleus	N	N	N	Y	N	N	1
Cranial Nerves	Su3C	supraoculomotor cap	N	N	N	N	N	Y	1
Cranial Nerves	Su3	supraoculomotor periaqueductal gray	N	N	N	N	N	Y	1
Cranial Nerves	3PC	oculomotor nucleus, parvicellular part	N	N	N	N	N	Y	1
Cranial Nerves	3N	oculomotor nucleus	N	Y	N	N	N	Y	2

Appendix B Table 10 Anterograde Tracing of VTA^{KOR} Neurons (Pons)

Quantification of number of mice containing mCherry-immunoreactive fibers after injection of AAV2-hSyn-DIO-mCherry into the VTA of *Oprk1^{cre}* mice. n = 6 mice, with 60 µm representative slices collected in triplicate throughout the brain. Regions featured in FIGURE X are highlighted in green.

Category	Region Abbr.	Region Description	Fibers present?						TOTAL
			1	2	3	4	5	6	
Misc.	Bar	Barrington's nucleus	N	N	Y	N	N	N	1
Misc.	A5	A5 noradrenaline cells	N	N	N	Y	N	N	1
Misc.	Cl	claustrum	Y	N	N	N	N	N	1
Misc.	PPy	parapyramidal nucleus	N	N	Y	N	N	N	1
Misc.	CGPn	central gray of the pons	Y	Y	N	N	N	N	2
Misc.	LC	locus coeruleus	N	N	N	N	N	Y	1
Misc.	SubCV	subcoeruleus nucleus, ventral part	N	N	Y	Y	N	Y	3
Misc.	SubCD	subcoeruleus nucleus, dorsal part	N	N	Y	N	N	Y	2
Misc.	RtTG	reticulotegmental nucleus of the pons	N	N	Y	N	N	Y	2
Misc.	RtTgP	reticulotegmental nucleus of the pons, pericentral part	N	N	N	N	N	Y	1

Appendix B Table 11 Anterograde Tracing of VTA^{KOR} Neurons (Medulla)

Quantification of number of mice containing mCherry-immunoreactive fibers after injection of AAV2-hSyn-DIO-mCherry into the VTA of *Oprk1^{cre}* mice. n = 6 mice, with 60 µm representative slices collected in triplicate throughout the brain. Regions featured in Figure 13 are highlighted in green.

Category	Region Abbr.	Region Description	Fibers present?						TOTAL
			1	2	3	4	5	6	
Dorsal Vagal Complex	SolC	nucleus of the solitary tract, commissural part	Y	N	Y	Y	N	N	3
Dorsal Vagal Complex	SolVL	nucleus of the solitary tract, ventrolateral part	Y	N	Y	Y	N	N	3
Dorsal Vagal Complex	SolV	solitary nucleus, ventral part	N	N	Y	Y	N	N	2
Dorsal Vagal Complex	SolM	nucleus of the solitary tract, medial part	Y	N	Y	Y	N	N	3
Dorsal Vagal Complex	SolI	nucleus of the solitary tract, interstitial part	N	N	Y	Y	N	N	2
Dorsal Vagal Complex	SolDL	solitary nucleus, dorsolateral part	Y	N	Y	Y	N	N	3
Dorsal Vagal Complex	SolCe	nucleus of the solitary tract, central part	N	N	Y	N	N	N	1
Dorsal Vagal Complex	SolG	nucleus of the solitary tract, gelatinous part	N	N	Y	N	N	N	1
Dorsal Vagal Complex	sol	solitary tract	N	N	Y	N	N	N	1
Dorsal Vagal Complex	AP	area postrema	Y	N	Y	Y	N	N	3
Dorsal Vagal Complex	10N	dorsal motor nucleus of vagus	N	N	Y	Y	N	N	2
Cranial Nerves	Sp5C	spinal trigeminal nucleus, caudal part	N	N	Y	N	N	N	1
Cranial Nerves	12N	hypoglossal nucleus	N	N	N	Y	Y	Y	3
Cranial Nerves	Amb	ambiguus nucleus	N	N	N	Y	N	N	1
Spinal Tracts	Cu	cuneate nucleus	N	N	Y	N	N	N	1
Spinal Tracts	ts	tectospinal tract	N	Y	N	Y	Y	N	3
Spinal Tracts	IOA	inferior olive, subnucleus A of medial nucleus	Y	N	N	N	N	N	1
Spinal Tracts	IOB	inferior olive, subnucleus B of medial nucleus	Y	Y	N	N	Y	N	3
Spinal Tracts	IOBe	inferior olive, beta subnucleus	Y	N	N	N	Y	Y	3
Spinal Tracts	IOC	inferior olive, subnucleus C of medial nucleus	Y	N	N	N	Y	N	2
Spinal Tracts	IOD	inferior olive, dorsal nucleus	Y	Y	Y	Y	Y	Y	6
Spinal Tracts	IOK	inferior olive, cap of Kooy of the medial nucleus	Y	N	N	N	Y	Y	3
Spinal Tracts	IOM	inferior olive, medial nucleus	N	Y	Y	Y	Y	Y	5
Spinal Tracts	IOPr	inferior olive, principal nucleus	Y	Y	Y	Y	Y	Y	6
Spinal Tracts	IOVL	inferior olive, ventrolateral protrusion	Y	N	N	N	Y	N	2
Spinal Tracts	IODM	inferior olive, dorsomedial cell group	N	Y	N	N	Y	Y	3
Spinal Tracts	mlf	medial longitudinal fasciculus	N	Y	Y	Y	Y	N	4

Appendix B Table 12 Anterograde Tracing of VTA^{KOR} Neurons (Medulla cont.)

Quantification of number of mice containing mCherry-immunoreactive fibers after injection of AAV2-hSyn-DIO-mCherry into the VTA of *Oprk1^{cre}* mice. n = 6 mice, with 60 µm representative slices collected in triplicate throughout the brain. Regions featured in Figure 13 are highlighted in green.

Category	Region Abbr.	Region Description	Fibers present?						TOTAL
			1	2	3	4	5	6	
Medullary Raphe Nuclei	ROb	raphe obscurus nucleus	Y	Y	Y	Y	Y	Y	6
Medullary Raphe Nuclei	RPa	raphe pallidus nucleus	Y	N	N	Y	N	N	2
Rostral Ventromedial Medulla (RVM)	RMg	raphe magnus nucleus	Y	Y	N	Y	Y	Y	5
Rostral Ventromedial Medulla (RVM)	Gi	gigantocellular reticular nucleus	Y	Y	N	Y	Y	Y	5
Rostral Ventromedial Medulla (RVM)	GiA	gigantocellular reticular nucleus, alpha part	Y	Y	Y	Y	Y	Y	6
Paragigantocellular Nuclei	LPGi	lateral paragigantocellular nucleus	Y	Y	Y	Y	Y	Y	6
Paragigantocellular Nuclei	DPGi	dorsal paragigantocellular nucleus	N	N	N	Y	N	N	1
Misc.	A1	A1 noradrenaline cells	Y	N	N	N	Y	Y	3
Misc.	A1/C1	noradrenaline/adrenaline cells	N	N	Y	N	N	N	1
Misc.	C1	C1 adrenaline cells	Y	N	N	N	N	N	1

Bibliography

Abrimian, A., Kraft, T., & Pan, Y.-X. (2021). Endogenous Opioid Peptides and Alternatively Spliced Mu Opioid Receptor Seven Transmembrane Carboxyl-Terminal Variants. *International Journal of Molecular Sciences*, *22*(7). https://doi.org/10.3390/ijms22073779

Aguilar, J. I., Dunn, M., Mingote, S., Karam, C. S., Farino, Z. J., Sonders, M. S., Choi, S. J., Grygoruk, A., Zhang, Y., Cela, C., Choi, B. J., Flores, J., Freyberg, R. J., McCabe, B. D., Mosharov, E. V., Krantz, D. E., Javitch, J. A., Sulzer, D., Sames, D., … Freyberg, Z. (2017). Neuronal depolarization drives increased dopamine synaptic vesicle loading via VGLUT. *Neuron*, *95*(5), 1074-1088.e7. https://doi.org/10.1016/j.neuron.2017.07.038

Albanese, A., & Minciacchi, D. (1983). Organization of the ascending projections from the ventral tegmental area: a multiple fluorescent retrograde tracer study in the rat. *The Journal of Comparative Neurology*, *216*(4), 406–420. https://doi.org/10.1002/cne.902160406

American Psychiatric Association. (2013). *Diagnostic and Statistical Manual of Mental Disorders* (Fifth Edition, p. 989). Generic.

Azar, M. R., Jones, B. C., & Schulteis, G. (2003). Conditioned place aversion is a highly sensitive index of acute opioid dependence and withdrawal. *Psychopharmacology*, *170*(1), 42–50. https://doi.org/10.1007/s00213-003-1514-y

Bals-Kubik, R., Ableitner, A., Herz, A., & Shippenberg, T. S. (1993). Neuroanatomical sites mediating the motivational effects of opioids as mapped by the conditioned place preference paradigm in rats. *The Journal of Pharmacology and Experimental Therapeutics*, *264*(1), 489–495.

Baumeister, A. A., Anticich, T. G., Hebert, G., Hawkins, M. F., & Nagy, M. (1989). Evidence that physical dependence on morphine is mediated by the ventral midbrain. *Neuropharmacology*, *28*(11), 1151–1157. https://doi.org/10.1016/0028-3908(89)90204-9

Bharucha, A. E., & Lacy, B. E. (2020). Mechanisms, evaluation, and management of chronic constipation. *Gastroenterology*, *158*(5), 1232-1249.e3. https://doi.org/10.1053/j.gastro.2019.12.034

Blackwood, C. A., Hoerle, R., Leary, M., Schroeder, J., Job, M. O., McCoy, M. T., Ladenheim, B., Jayanthi, S., & Cadet, J. L. (2019). Molecular Adaptations in the Rat Dorsal Striatum and Hippocampus Following Abstinence-Induced Incubation of Drug Seeking After Escalated Oxycodone Self-Administration. *Molecular Neurobiology*, *56*(5), 3603–3615. https://doi.org/10.1007/s12035-018-1318-z

Bloodgood, D. W., Hardaway, J. A., Stanhope, C. M., Pati, D., Pina, M. M., Neira, S., Desai, S., Boyt, K. M., Palmiter, R. D., & Kash, T. L. (2021). Kappa opioid receptor and dynorphin signaling in the central amygdala regulates alcohol intake. *Molecular Psychiatry*, *26*(6), 2187–2199. https://doi.org/10.1038/s41380-020-0690-z

Bourin, M., & Hascoët, M. (2003). The mouse light/dark box test. *European Journal of Pharmacology*, *463*(1–3), 55–65. https://doi.org/10.1016/s0014-2999(03)01274-3

Bozarth, M. A., & Wise, R. A. (1981). Intracranial self-administration of morphine into the ventral tegmental area in rats. *Life Sciences*, *28*(5), 551–555. https://doi.org/10.1016/0024-3205(81)90148-x

Bozarth, M. A., & Wise, R. A. (1984). Anatomically distinct opiate receptor fields mediate reward and physical dependence. *Science*, *224*(4648), 516–517. https://doi.org/10.1126/science.6324347

Breton, J. M., Charbit, A. R., Snyder, B. J., Fong, P. T. K., Dias, E. V., Himmels, P., Lock, H., & Margolis, E. B. (2019). Relative contributions and mapping of ventral tegmental area dopamine and GABA neurons by projection target in the rat. *The Journal of Comparative Neurology*, *527*(5), 916–941. https://doi.org/10.1002/cne.24572

Browne, C. J., Futamura, R., Minier-Toribio, A., Hicks, E. M., Ramakrishnan, A., Martínez-Rivera, F., Estill, M., Godino, A., Parise, E. M., Torres-Berrío, A., Cunningham, A. M., Hamilton, P. J., Walker, D. M., Huckins, L. M., Hurd, Y. L., Shen, L., & Nestler, E. J. (2023). Transcriptional signatures of heroin intake and seeking throughout the brain reward circuit. *BioRxiv*. https://doi.org/10.1101/2023.01.11.523688

Browne, C. J., Godino, A., Salery, M., & Nestler, E. J. (2020). Epigenetic mechanisms of opioid addiction. *Biological Psychiatry*, *87*(1), 22–33. https://doi.org/10.1016/j.biopsych.2019.06.027

Buck, S. A., Torregrossa, M. M., Logan, R. W., & Freyberg, Z. (2021). Roles of dopamine and glutamate co-release in the nucleus accumbens in mediating the actions of drugs of abuse. *The FEBS Journal*, *288*(5), 1462–1474. https://doi.org/10.1111/febs.15496

Cai, X., Huang, H., Kuzirian, M. S., Snyder, L. M., Matsushita, M., Lee, M. C., Ferguson, C., Homanics, G. E., Barth, A. L., & Ross, S. E. (2016). Generation of a KOR-Cre knockin mouse strain to study cells involved in kappa opioid signaling. *Genesis*, *54*(1), 29–37. https://doi.org/10.1002/dvg.22910

Can, A., Dao, D. T., Terrillion, C. E., Piantadosi, S. C., Bhat, S., & Gould, T. D. (2012). The tail suspension test. *Journal of Visualized Experiments*, *59*, e3769. https://doi.org/10.3791/3769

Che, T., Dwivedi-Agnihotri, H., Shukla, A. K., & Roth, B. L. (2021). Biased ligands at opioid receptors: Current status and future directions. *Science Signaling*, *14*(677). https://doi.org/10.1126/scisignal.aav0320

Chefer, V. I., Bäckman, C. M., Gigante, E. D., & Shippenberg, T. S. (2013). Kappa opioid receptors on dopaminergic neurons are necessary for kappa-mediated place aversion. *Neuropsychopharmacology*, *38*(13), 2623–2631. https://doi.org/10.1038/npp.2013.171

Chiang, M. C., Nguyen, E. K., Canto-Bustos, M., Papale, A. E., Oswald, A.-M. M., & Ross, S. E. (2020). Divergent Neural Pathways Emanating from the Lateral Parabrachial Nucleus Mediate Distinct Components of the Pain Response. *Neuron*, *106*(6), 927-939.e5. https://doi.org/10.1016/j.neuron.2020.03.014

Cohen, J. (1988). *Statistical Power Analysis for the Behavioral Sciences (2nd Edition)* (2nd ed., p. 400). Routledge.

Cooper, A. H., Hedden, N. S., Corder, G., Lamerand, S. R., Donahue, R. R., Morales-Medina, J. C., Selan, L., Prasoon, P., & Taylor, B. K. (2022). Endogenous μ-opioid receptor activity in the lateral and capsular subdivisions of the right central nucleus of the amygdala prevents chronic postoperative pain. *Journal of Neuroscience Research*, *100*(1), 48–65. https://doi.org/10.1002/jnr.24846

Csete, J., Kamarulzaman, A., Kazatchkine, M., Altice, F., Balicki, M., Buxton, J., Cepeda, J., Comfort, M., Goosby, E., Goulão, J., Hart, C., Kerr, T., Lajous, A. M., Lewis, S., Martin, N., Mejía, D., Camacho, A., Mathieson, D., Obot, I., … Beyrer, C. (2016). Public health and international drug policy. *The Lancet*, *387*(10026), 1427–1480. https://doi.org/10.1016/S0140-6736(16)00619-X

David, V., Durkin, T. P., & Cazala, P. (2002). Differential effects of the dopamine D2/D3 receptor antagonist sulpiride on self-administration of morphine into the ventral tegmental area or the nucleus accumbens. *Psychopharmacology*, *160*(3), 307–317. https://doi.org/10.1007/s00213-001-0981-2

Demidenko, M. I., Dobscha, S. K., Morasco, B. J., Meath, T. H. A., Ilgen, M. A., & Lovejoy, T. I. (2017). Suicidal ideation and suicidal self-directed violence following clinician-initiated prescription opioid discontinuation among long-term opioid users. *General Hospital Psychiatry*, *47*, 29–35. https://doi.org/10.1016/j.genhosppsych.2017.04.011

Devine, D. P., Leone, P., Pocock, D., & Wise, R. A. (1993). Differential involvement of ventral tegmental mu, delta and kappa opioid receptors in modulation of basal mesolimbic dopamine release: in vivo microdialysis studies. *The Journal of Pharmacology and Experimental Therapeutics*, *266*(3), 1236–1246.

Diana, M., Pistis, M., Muntoni, A., & Gessa, G. (1995). Profound decrease of mesolimbic dopaminergic neuronal activity in morphine withdrawn rats. *The Journal of Pharmacology and Experimental Therapeutics*, *272*(2), 781–785.

Di Chiara, G., & Imperato, A. (1988). Drugs abused by humans preferentially increase synaptic dopamine concentrations in the mesolimbic system of freely moving rats. *Proceedings of the National Academy of Sciences of the United States of America*, *85*(14), 5274–5278. https://doi.org/10.1073/pnas.85.14.5274

Dos Santos, R. G., Bouso, J. C., Alcázar-Córcoles, M. Á., & Hallak, J. E. C. (2018). Efficacy, tolerability, and safety of serotonergic psychedelics for the management of mood, anxiety, and substance-use disorders: a systematic review of systematic reviews. *Expert Review of Clinical Pharmacology*, *11*(9), 889–902. https://doi.org/10.1080/17512433.2018.1511424

Ehrich, J. M., Messinger, D. I., Knakal, C. R., Kuhar, J. R., Schattauer, S. S., Bruchas, M. R., Zweifel, L. S., Kieffer, B. L., Phillips, P. E. M., & Chavkin, C. (2015). Kappa Opioid Receptor-Induced Aversion Requires p38 MAPK Activation in VTA Dopamine Neurons. *The Journal of Neuroscience*, *35*(37), 12917–12931. https://doi.org/10.1523/JNEUROSCI.2444-15.2015

Fallon, J. H. (1981). Collateralization of monoamine neurons: mesotelencephalic dopamine projections to caudate, septum, and frontal cortex. *The Journal of Neuroscience*, *1*(12), 1361–1368. https://doi.org/10.1523/JNEUROSCI.01-12-01361.1981

Farmer, A. D., Holt, C. B., Downes, T. J., Ruggeri, E., Del Vecchio, S., & De Giorgio, R. (2018). Pathophysiology, diagnosis, and management of opioid-induced constipation. *The Lancet. Gastroenterology & Hepatology*, *3*(3), 203–212. https://doi.org/10.1016/S2468-1253(18)30008-6

Farrell, M. (1994). Opiate withdrawal. *Addiction*, *89*(11), 1471–1475. https://doi.org/10.1111/j.1360-0443.1994.tb03745.x

Fenton, J. J., Magnan, E., Tseregounis, I. E., Xing, G., Agnoli, A. L., & Tancredi, D. J. (2022). Long-term Risk of Overdose or Mental Health Crisis After Opioid Dose Tapering. *JAMA Network Open*, *5*(6), e2216726. https://doi.org/10.1001/jamanetworkopen.2022.16726

Geisler, S., Derst, C., Veh, R. W., & Zahm, D. S. (2007). Glutamatergic afferents of the ventral tegmental area in the rat. *The Journal of Neuroscience*, *27*(21), 5730–5743. https://doi.org/10.1523/JNEUROSCI.0012-07.2007

Georges, F., Le Moine, C., & Aston-Jones, G. (2006). No effect of morphine on ventral tegmental dopamine neurons during withdrawal. *The Journal of Neuroscience*, *26*(21), 5720–5726. https://doi.org/10.1523/JNEUROSCI.5032-05.2006

George, O., & Koob, G. F. (2017). Individual differences in the neuropsychopathology of addiction. *Dialogues in Clinical Neuroscience*, *19*(3), 217–229. https://doi.org/10.31887/DCNS.2017.19.3/gkoob

Gossop, M., & Strang, J. (1991). A comparison of the withdrawal responses of heroin and methadone addicts during detoxification. *The British Journal of Psychiatry*, *158*, 697–699. https://doi.org/10.1192/bjp.158.5.697

Greenwald, N. F., Miller, G., Moen, E., Kong, A., Kagel, A., Dougherty, T., Fullaway, C. C., McIntosh, B. J., Leow, K. X., Schwartz, M. S., Pavelchek, C., Cui, S., Camplisson, I., Bar-Tal, O., Singh, J., Fong, M., Chaudhry, G., Abraham, Z., Moseley, J., … Van Valen, D. (2022). Whole-cell segmentation of tissue images with human-level performance using

large-scale data annotation and deep learning. *Nature Biotechnology*, *40*(4), 555–565. https://doi.org/10.1038/s41587-021-01094-0

Gysling, K., & Wang, R. Y. (1983). Morphine-induced activation of A10 dopamine neurons in the rat. *Brain Research*, *277*(1), 119–127. https://doi.org/10.1016/0006-8993(83)90913-7

Haight, B. R., Learned, S. M., Laffont, C. M., Fudala, P. J., Zhao, Y., Garofalo, A. S., Greenwald, M. K., Nadipelli, V. R., Ling, W., Heidbreder, C., & RB-US-13-0001 Study Investigators. (2019). Efficacy and safety of a monthly buprenorphine depot injection for opioid use disorder: a multicentre, randomised, double-blind, placebo-controlled, phase 3 trial. *The Lancet*, *393*(10173), 778–790. https://doi.org/10.1016/S0140-6736(18)32259-1

Helal, M. A., Habib, E. S., & Chittiboyina, A. G. (2017). Selective kappa opioid antagonists for treatment of addiction, are we there yet? *European Journal of Medicinal Chemistry*, *141*, 632–647. https://doi.org/10.1016/j.ejmech.2017.10.012

Jalabert, M., Bourdy, R., Courtin, J., Veinante, P., Manzoni, O. J., Barrot, M., & Georges, F. (2011). Neuronal circuits underlying acute morphine action on dopamine neurons. *Proceedings of the National Academy of Sciences of the United States of America*, *108*(39), 16446–16450. https://doi.org/10.1073/pnas.1105418108

James, J. R., Scott, J. M., Klein, J. W., Jackson, S., McKinney, C., Novack, M., Chew, L., & Merrill, J. O. (2019). Mortality After Discontinuation of Primary Care-Based Chronic Opioid Therapy for Pain: a Retrospective Cohort Study. *Journal of General Internal Medicine*, *34*(12), 2749–2755. https://doi.org/10.1007/s11606-019-05301-2

Johnson, S. W., & North, R. A. (1992). Opioids excite dopamine neurons by hyperpolarization of local interneurons. *The Journal of Neuroscience*, *12*(2), 483–488. https://doi.org/10.1523/JNEUROSCI.12-02-00483.1992

Kalamarides, D. J., Singh, A., Wolfman, S. L., & Dani, J. A. (2023). Sex differences in VTA GABA transmission and plasticity during opioid withdrawal. *Scientific Reports*, *13*(1), 8460. https://doi.org/10.1038/s41598-023-35673-9

Kanof, P. D., Aronson, M. J., & Ness, R. (1993). Organic mood syndrome associated with detoxification from methadone maintenance. *The American Journal of Psychiatry*, *150*(3), 423–428. https://doi.org/10.1176/ajp.150.3.423

Kim, H. J., Kim, M., Kang, B., Yun, S., Ryeo, S. E., Hwang, D., & Kim, J.-H. (2019). Systematic analysis of expression signatures of neuronal subpopulations in the VTA. *Molecular Brain*, *12*(1), 110. https://doi.org/10.1186/s13041-019-0530-8

Krantz, M. J., Palmer, R. B., & Haigney, M. C. P. (2021). Cardiovascular Complications of Opioid Use: JACC State-of-the-Art Review. *Journal of the American College of Cardiology*, *77*(2), 205–223. https://doi.org/10.1016/j.jacc.2020.11.002

Krashes, M. J., Koda, S., Ye, C., Rogan, S. C., Adams, A. C., Cusher, D. S., Maratos-Flier, E., Roth, B. L., & Lowell, B. B. (2011). Rapid, reversible activation of AgRP neurons drives

feeding behavior in mice. *The Journal of Clinical Investigation*, *121*(4), 1424–1428. https://doi.org/10.1172/JCI46229

Krashes, M. J., Shah, B. P., Madara, J. C., Olson, D. P., Strochlic, D. E., Garfield, A. S., Vong, L., Pei, H., Watabe-Uchida, M., Uchida, N., Liberles, S. D., & Lowell, B. B. (2014). An excitatory paraventricular nucleus to AgRP neuron circuit that drives hunger. *Nature*, *507*(7491), 238–242. https://doi.org/10.1038/nature12956

Land, B. B., Bruchas, M. R., Schattauer, S., Giardino, W. J., Aita, M., Messinger, D., Hnasko, T. S., Palmiter, R. D., & Chavkin, C. (2009). Activation of the kappa opioid receptor in the dorsal raphe nucleus mediates the aversive effects of stress and reinstates drug seeking. *Proceedings of the National Academy of Sciences of the United States of America*, *106*(45), 19168–19173. https://doi.org/10.1073/pnas.0910705106

Laschka, E., Herz, A., & Bläsig, J. (1976). Sites of action of morphine involved in the development of physical dependence in rats. I. Comparison of precipitated morphine withdrawal after intraperitoneal and intraventricular injection of morphine antagonists. *Psychopharmacologia*, *46*(2), 133–139. https://doi.org/10.1007/BF00421382

Lee, J. D., Nunes, E. V., Novo, P., Bachrach, K., Bailey, G. L., Bhatt, S., Farkas, S., Fishman, M., Gauthier, P., Hodgkins, C. C., King, J., Lindblad, R., Liu, D., Matthews, A. G., May, J., Peavy, K. M., Ross, S., Salazar, D., Schkolnik, P., … Rotrosen, J. (2018). Comparative effectiveness of extended-release naltrexone versus buprenorphine-naloxone for opioid relapse prevention (X:BOT): a multicentre, open-label, randomised controlled trial. *The Lancet*, *391*(10118), 309–318. https://doi.org/10.1016/S0140-6736(17)32812-X

Le Guen, S., Gestreau, C., & Besson, J.-M. (2003). Morphine withdrawal precipitated by specific mu, delta or kappa opioid receptor antagonists: a c-Fos protein study in the rat central nervous system. *The European Journal of Neuroscience*, *17*(11), 2425–2437. https://doi.org/10.1046/j.1460-9568.2003.02678.x

Liu, S. S., Pickens, S., Burma, N. E., Ibarra-Lecue, I., Yang, H., Xue, L., Cook, C., Hakimian, J. K., Severino, A. L., Lueptow, L., Komarek, K., Taylor, A. M. W., Olmstead, M. C., Carroll, F. I., Bass, C. E., Andrews, A. M., Walwyn, W., Trang, T., Evans, C. J., … Cahill, C. M. (2019). Kappa opioid receptors drive a tonic aversive component of chronic pain. *The Journal of Neuroscience*, *39*(21), 4162–4178. https://doi.org/10.1523/JNEUROSCI.0274-19.2019

Lutz, P.-E., Ayranci, G., Chu-Sin-Chung, P., Matifas, A., Koebel, P., Filliol, D., Befort, K., Ouagazzal, A.-M., & Kieffer, B. L. (2014). Distinct mu, delta, and kappa opioid receptor mechanisms underlie low sociability and depressive-like behaviors during heroin abstinence. *Neuropsychopharmacology*, *39*(11), 2694–2705. https://doi.org/10.1038/npp.2014.126

Madisen, L., Zwingman, T. A., Sunkin, S. M., Oh, S. W., Zariwala, H. A., Gu, H., Ng, L. L., Palmiter, R. D., Hawrylycz, M. J., Jones, A. R., Lein, E. S., & Zeng, H. (2010). A robust and high-throughput Cre reporting and characterization system for the whole mouse brain. *Nature Neuroscience*, *13*(1), 133–140. https://doi.org/10.1038/nn.2467

Maldonado, R., Fournié-Zaluski, M. C., & Roques, B. P. (1992). Attenuation of the morphine withdrawal syndrome by inhibition of catabolism of endogenous enkephalins in the periaqueductal gray matter. *Naunyn-Schmiedeberg's Archives of Pharmacology*, *345*(4), 466–472. https://doi.org/10.1007/BF00176626

Maldonado, R., Negus, S., & Koob, G. F. (1992). Precipitation of morphine withdrawal syndrome in rats by administration of mu-, delta- and kappa-selective opioid antagonists. *Neuropharmacology*, *31*(12), 1231–1241. https://doi.org/10.1016/0028-3908(92)90051-p

Margolis, E. B., Hjelmstad, G. O., Bonci, A., & Fields, H. L. (2003). Kappa-opioid agonists directly inhibit midbrain dopaminergic neurons. *The Journal of Neuroscience*, *23*(31), 9981–9986.

Margolis, E. B., & Karkhanis, A. N. (2019). Dopaminergic cellular and circuit contributions to kappa opioid receptor mediated aversion. *Neurochemistry International*, *129*, 104504. https://doi.org/10.1016/j.neuint.2019.104504

Margolis, E. B., Lock, H., Chefer, V. I., Shippenberg, T. S., Hjelmstad, G. O., & Fields, H. L. (2006). Kappa opioids selectively control dopaminergic neurons projecting to the prefrontal cortex. *Proceedings of the National Academy of Sciences of the United States of America*, *103*(8), 2938–2942. https://doi.org/10.1073/pnas.0511159103

Mazei-Robison, M. S., Koo, J. W., Friedman, A. K., Lansink, C. S., Robison, A. J., Vinish, M., Krishnan, V., Kim, S., Siuta, M. A., Galli, A., Niswender, K. D., Appasani, R., Horvath, M. C., Neve, R. L., Worley, P. F., Snyder, S. H., Hurd, Y. L., Cheer, J. F., Han, M.-H., … Nestler, E. J. (2011). Role for mTOR signaling and neuronal activity in morphine-induced adaptations in ventral tegmental area dopamine neurons. *Neuron*, *72*(6), 977–990. https://doi.org/10.1016/j.neuron.2011.10.012

Mazei-Robison, M. S., & Nestler, E. J. (2012). Opiate-induced molecular and cellular plasticity of ventral tegmental area and locus coeruleus catecholamine neurons. *Cold Spring Harbor Perspectives in Medicine*, *2*(7), a012070. https://doi.org/10.1101/cshperspect.a012070

Miranda-Barrientos, J., Chambers, I., Mongia, S., Liu, B., Wang, H.-L., Mateo-Semidey, G. E., Margolis, E. B., Zhang, S., & Morales, M. (2021). Ventral tegmental area GABA, glutamate, and glutamate-GABA neurons are heterogeneous in their electrophysiological and pharmacological properties. *The European Journal of Neuroscience*. https://doi.org/10.1111/ejn.15156

Mongia, S., Yamaguchi, T., Liu, B., Zhang, S., Wang, H., & Morales, M. (2019). The Ventral Tegmental Area has calbindin neurons with the capability to co-release glutamate and dopamine into the nucleus accumbens. *The European Journal of Neuroscience*, *50*(12), 3968–3984. https://doi.org/10.1111/ejn.14493

Nair-Roberts, R. G., Chatelain-Badie, S. D., Benson, E., White-Cooper, H., Bolam, J. P., & Ungless, M. A. (2008). Stereological estimates of dopaminergic, GABAergic and glutamatergic neurons in the ventral tegmental area, substantia nigra and retrorubral field

in the rat. *Neuroscience*, *152*(4), 1024–1031. https://doi.org/10.1016/j.neuroscience.2008.01.046

National Inventory of Collateral Consequences of Conviction. (2023). *What are collateral consequences?*

Nguyen, E., Smith, K. M., Cramer, N., Holland, R. A., Bleimeister, I. H., Flores-Felix, K., Silberberg, H., Keller, A., Le Pichon, C. E., & Ross, S. E. (2022). Medullary kappa-opioid receptor neurons inhibit pain and itch through a descending circuit. *Brain: A Journal of Neurology*, *145*(7), 2586–2601. https://doi.org/10.1093/brain/awac189

Office of National Drug Control Policy. (2016). *Progress toward Some National Drug Control Strategy Goals, but None Have Been Fully Achieved*.

Oliva, E. M., Bowe, T., Manhapra, A., Kertesz, S., Hah, J. M., Henderson, P., Robinson, A., Paik, M., Sandbrink, F., Gordon, A. J., & Trafton, J. A. (2020). Associations between stopping prescriptions for opioids, length of opioid treatment, and overdose or suicide deaths in US veterans: observational evaluation. *BMJ (Clinical Research Ed.)*, *368*, m283. https://doi.org/10.1136/bmj.m283

Olmstead, M. C., & Franklin, K. B. (1997). The development of a conditioned place preference to morphine: effects of lesions of various CNS sites. *Behavioral Neuroscience*, *111*(6), 1313–1323. https://doi.org/10.1037//0735-7044.111.6.1313

Omelchenko, N., & Sesack, S. R. (2010). Periaqueductal gray afferents synapse onto dopamine and GABA neurons in the rat ventral tegmental area. *Journal of Neuroscience Research*, *88*(5), 981–991. https://doi.org/10.1002/jnr.22265

Pathan, H., & Williams, J. (2012). Basic opioid pharmacology: an update. *British Journal of Pain*, *6*(1), 11–16. https://doi.org/10.1177/2049463712438493

Paul, A. K., Smith, C. M., Rahmatullah, M., Nissapatorn, V., Wilairatana, P., Spetea, M., Gueven, N., & Dietis, N. (2021). Opioid Analgesia and Opioid-Induced Adverse Effects: A Review. *Pharmaceuticals (Basel, Switzerland)*, *14*(11). https://doi.org/10.3390/ph14111091

Paxinos, G., & Franklin, K. B. J. (2012). *Paxinos and Franklin's the Mouse Brain in Stereotaxic Coordinates* (4th ed., p. 360). Academic Press.

Phan, B. N., Ray, M. H., Xue, X., Fenster, R. J., Kohut, S. J., Bergman, J., Haber, S. N., Mccullough, K. M., Kuppe-Fish, M. K., Glausier, J. R., Su, Q., Tipton, A. E., Lewis, D. A., Freyberg, Z., Tseng, G. C., Ressler, K. J., Russek, S. J., Alekseyev, Y., Seney, M. L., … Logan, R. W. (2023). Single nucleus transcriptomics of human and monkey striatum implicates DNA damage, neuroinflammation, and neurodegeneration signaling in opioid use disorder. *BioRxiv*. https://doi.org/10.1101/2023.05.17.541145

Piras, A. P., Zhou, Y., Schlussman, S. D., Ho, A., & Kreek, M. J. (2010). Acute withdrawal from chronic escalating-dose binge cocaine administration alters kappa opioid receptor stimulation of [35S] guanosine 5'-O-[gamma-thio]triphosphate acid binding in the rat

ventral tegmental area. *Neuroscience*, *169*(2), 751–757. https://doi.org/10.1016/j.neuroscience.2010.04.060

Pomrenze, M. B., Cardozo Pinto, D. F., Neumann, P. A., Llorach, P., Tucciarone, J. M., Morishita, W., Eshel, N., Heifets, B. D., & Malenka, R. C. (2022). Modulation of 5-HT release by dynorphin mediates social deficits during opioid withdrawal. *Neuron*, *110*(24), 4125-4143.e6. https://doi.org/10.1016/j.neuron.2022.09.024

Punch, L. J., Self, D. W., Nestler, E. J., & Taylor, J. R. (1997). Opposite modulation of opiate withdrawal behaviors on microinfusion of a protein kinase A inhibitor versus activator into the locus coeruleus or periaqueductal gray. *The Journal of Neuroscience*, *17*(21), 8520–8527. https://doi.org/10.1523/JNEUROSCI.17-21-08520.1997

Robble, M. A., Bozsik, M. E., Wheeler, D. S., & Wheeler, R. A. (2020). Learned avoidance requires VTA KOR-mediated reductions in dopamine. *Neuropharmacology*, *167*, 107996. https://doi.org/10.1016/j.neuropharm.2020.107996

Russell, M. A. (1976). What is dependence. *Drugs and Drug Dependence*, 182–187.

Schlosburg, J. E., Whitfield, T. W., Park, P. E., Crawford, E. F., George, O., Vendruscolo, L. F., & Koob, G. F. (2013). Long-term antagonism of κ opioid receptors prevents escalation of and increased motivation for heroin intake. *The Journal of Neuroscience*, *33*(49), 19384–19392. https://doi.org/10.1523/JNEUROSCI.1979-13.2013

Shippenberg, T. S., Bals-Kubik, R., & Herz, A. (1993). Examination of the neurochemical substrates mediating the motivational effects of opioids: role of the mesolimbic dopamine system and D-1 vs. D-2 dopamine receptors. *The Journal of Pharmacology and Experimental Therapeutics*, *265*(1), 53–59.

Shippenberg, T. S., & Herz, A. (1987). Place preference conditioning reveals the involvement of D1-dopamine receptors in the motivational properties of μ- and κ-opioid agonists. *Brain Research*, *436*(1), 169–172. https://doi.org/10.1016/0006-8993(87)91571-X

Shook, J. E., Lemcke, P. K., Gehrig, C. A., Hruby, V. J., & Burks, T. F. (1989). Antidiarrheal properties of supraspinal mu and delta and peripheral mu, delta and kappa opioid receptors: inhibition of diarrhea without constipation. *The Journal of Pharmacology and Experimental Therapeutics*, *249*(1), 83–90.

Sinchaisuk, S., Ho, I. K., & Rockhold, R. W. (2002). Focal kappa-opioid receptor-mediated dependence and withdrawal in the nucleus paragigantocellularis. *Pharmacology, Biochemistry, and Behavior*, *74*(1), 241–252. https://doi.org/10.1016/s0091-3057(02)00993-0

Skinner, B. F. (1938). *The Behavior of Organisms. Appleton-Century-Crofts*.

Sklair-Tavron, L., Shi, W. X., Lane, S. B., Harris, H. W., Bunney, B. S., & Nestler, E. J. (1996). Chronic morphine induces visible changes in the morphology of mesolimbic dopamine

neurons. *Proceedings of the National Academy of Sciences of the United States of America*, *93*(20), 11202–11207. https://doi.org/10.1073/pnas.93.20.11202

Spadotto, V., Zorzi, A., Elmaghawry, M., Meggiolaro, M., & Pittoni, G. M. (2013). Heart failure due to “stress cardiomyopathy”: a severe manifestation of the opioid withdrawal syndrome. *European Heart Journal. Acute Cardiovascular Care*, *2*(1), 84–87. https://doi.org/10.1177/2048872612474923

Spanagel, R, Almeida, O. F., Bartl, C., & Shippenberg, T. S. (1994). Endogenous kappa-opioid systems in opiate withdrawal: role in aversion and accompanying changes in mesolimbic dopamine release. *Psychopharmacology*, *115*(1–2), 121–127. https://doi.org/10.1007/BF02244761

Spanagel, R, Herz, A., & Shippenberg, T. S. (1990). The effects of opioid peptides on dopamine release in the nucleus accumbens: an in vivo microdialysis study. *Journal of Neurochemistry*, *55*(5), 1734–1740. https://doi.org/10.1111/j.1471-4159.1990.tb04963.x

Spanagel, R, Herz, A., & Shippenberg, T. S. (1992). Opposing tonically active endogenous opioid systems modulate the mesolimbic dopaminergic pathway. *Proceedings of the National Academy of Sciences of the United States of America*, *89*(6), 2046–2050. https://doi.org/10.1073/pnas.89.6.2046

Spanagel, R, & Shippenberg, T. S. (1993). Modulation of morphine-induced sensitization by endogenous kappa opioid systems in the rat. *Neuroscience Letters*, *153*(2), 232–236. https://doi.org/10.1016/0304-3940(93)90329-j

Spanagel, Rainer, Herz, A., & Shippenberg, T. S. (1991). Modulation of the mesolimbic dopaminergic system by β-endorphin-(1-27) as assessed by microdialysis. *European Journal of Pharmacology*, *200*(2–3), 319–324. https://doi.org/10.1016/0014-2999(91)90589-I

Spangler, R., Ho, A., Zhou, Y., Maggos, C. E., Yuferov, V., & Kreek, M. J. (1996). Regulation of kappa opioid receptor mRNA in the rat brain by "binge’ pattern cocaine administration and correlation with preprodynorphin mRNA. *Brain Research. Molecular Brain Research*, *38*(1), 71–76. https://doi.org/10.1016/0169-328X(95)00319-N

Spencer, M. R., Miniño, A. M., & Warner, M. (2022). Drug Overdose Deaths in the United States, 2001–2021. *NCHS Data Brief, No. 457*.

Spiga, S., Serra, G. P., Puddu, M. C., Foddai, M., & Diana, M. (2003). Morphine withdrawal-induced abnormalities in the VTA: confocal laser scanning microscopy. *The European Journal of Neuroscience*, *17*(3), 605–612. https://doi.org/10.1046/j.1460-9568.2003.02435.x

Substance Abuse and Mental Health Services Administration, & U.S. Department of Health and Human Services. (2021). *Results from the 2020 National Survey on Drug Use and Health*.

Swanson, L. W. (1982). The projections of the ventral tegmental area and adjacent regions: a combined fluorescent retrograde tracer and immunofluorescence study in the rat. *Brain Research Bulletin*, *9*(1–6), 321–353. https://doi.org/10.1016/0361-9230(82)90145-9

Tejeda, H. A., Counotte, D. S., Oh, E., Ramamoorthy, S., Schultz-Kuszak, K. N., Bäckman, C. M., Chefer, V., O'Donnell, P., & Shippenberg, T. S. (2013). Prefrontal cortical kappa-opioid receptor modulation of local neurotransmission and conditioned place aversion. *Neuropsychopharmacology*, *38*(9), 1770–1779. https://doi.org/10.1038/npp.2013.76

Valentino, R. J., & Volkow, N. D. (2018). Untangling the complexity of opioid receptor function. *Neuropsychopharmacology*, *43*(13), 2514–2520. https://doi.org/10.1038/s41386-018-0225-3

Walker, B. M., Zorrilla, E. P., & Koob, G. F. (2011). Systemic κ-opioid receptor antagonism by nor-binaltorphimine reduces dependence-induced excessive alcohol self-administration in rats. *Addiction Biology*, *16*(1), 116–119. https://doi.org/10.1111/j.1369-1600.2010.00226.x

Wedam, E. F., & Haigney, M. C. (2016). The impact of opioids on cardiac electrophysiology. *Current Cardiology Reviews*, *12*(1), 27–36. https://doi.org/10.2174/1573403x1201160126122405

Wise, R. A., & Koob, G. F. (2014). The development and maintenance of drug addiction. *Neuropsychopharmacology*, *39*(2), 254–262. https://doi.org/10.1038/npp.2013.261

Wise, R. A. (2004). Dopamine, learning and motivation. *Nature Reviews. Neuroscience*, *5*(6), 483–494. https://doi.org/10.1038/nrn1406

Yoo, J. H., Zell, V., Gutierrez-Reed, N., Wu, J., Ressler, R., Shenasa, M. A., Johnson, A. B., Fife, K. H., Faget, L., & Hnasko, T. S. (2016). Ventral tegmental area glutamate neurons co-release GABA and promote positive reinforcement. *Nature Communications*, *7*, 13697. https://doi.org/10.1038/ncomms13697

Young, G. A., Steinfels, G. F., & Khazan, N. (1979). Spontaneous vs. naloxone-induced abstinence in dependent rats self-administering L-alpha-acetylmethadol (LAAM) or morphine. *Pharmacology, Biochemistry, and Behavior*, *10*(4), 585–589. https://doi.org/10.1016/0091-3057(79)90237-5

Yu, X., Ba, W., Zhao, G., Ma, Y., Harding, E. C., Yin, L., Wang, D., Li, H., Zhang, P., Shi, Y., Yustos, R., Vyssotski, A. L., Dong, H., Franks, N. P., & Wisden, W. (2021). Dysfunction of ventral tegmental area GABA neurons causes mania-like behavior. *Molecular Psychiatry*, *26*(9), 5213–5228. https://doi.org/10.1038/s41380-020-0810-9

Zangen, A., Ikemoto, S., Zadina, J. E., & Wise, R. A. (2002). Rewarding and psychomotor stimulant effects of endomorphin-1: anteroposterior differences within the ventral tegmental area and lack of effect in nucleus accumbens. *The Journal of Neuroscience*, *22*(16), 7225–7233. https://doi.org/10.1523/JNEUROSCI.22-16-07225.2002

Zan, G.-Y., Wang, Q., Wang, Y.-J., Liu, Y., Hang, A., Shu, X.-H., & Liu, J.-G. (2015). Antagonism of κ opioid receptor in the nucleus accumbens prevents the depressive-like behaviors following prolonged morphine abstinence. *Behavioural Brain Research, 291*, 334–341. https://doi.org/10.1016/j.bbr.2015.05.053

Zell, V., Steinkellner, T., Hollon, N. G., Warlow, S. M., Souter, E., Faget, L., Hunker, A. C., Jin, X., Zweifel, L. S., & Hnasko, T. S. (2020). VTA Glutamate Neuron Activity Drives Positive Reinforcement Absent Dopamine Co-release. *Neuron*, *107*(5), 864-873.e4. https://doi.org/10.1016/j.neuron.2020.06.011

Zhang, Y., Landthaler, M., Schlussman, S. D., Yuferov, V., Ho, A., Tuschl, T., & Kreek, M. J. (2009). Mu opioid receptor knockdown in the substantia nigra/ventral tegmental area by synthetic small interfering RNA blocks the rewarding and locomotor effects of heroin. *Neuroscience*, *158*(2), 474–483. https://doi.org/10.1016/j.neuroscience.2008.09.039